Optical Spectroscopy of Photosynthetic Complexes:
Focus on Low-Temperature Protein Dynamics

Nicoleta Herascu

A Thesis

in

The Department

of

Physics

Presented in Partial Fulfillment of the Requirements
for the Degree of Master of Science (Physics) at
Concordia University
Montreal, Quebec, Canada

April 2010

Library and Archives
Canada

Published Heritage
Branch

395 Wellington Street
Ottawa ON K1A 0N4
Canada

Bibliothèque et
Archives Canada

Direction du
Patrimoine de l'édition

395, rue Wellington
Ottawa ON K1A 0N4
Canada

Your file Votre référence
ISBN: 978-0-494-67247-1
Our file Notre référence
ISBN: 978-0-494-67247-1

NOTICE:

The author has granted a non-exclusive license allowing Library and Archives Canada to reproduce, publish, archive, preserve, conserve, communicate to the public by telecommunication or on the Internet, loan, distribute and sell theses worldwide, for commercial or non-commercial purposes, in microform, paper, electronic and/or any other formats.

The author retains copyright ownership and moral rights in this thesis. Neither the thesis nor substantial extracts from it may be printed or otherwise reproduced without the author's permission.

AVIS:

L'auteur a accordé une licence non exclusive permettant à la Bibliothèque et Archives Canada de reproduire, publier, archiver, sauvegarder, conserver, transmettre au public par télécommunication ou par l'Internet, prêter, distribuer et vendre des thèses partout dans le monde, à des fins commerciales ou autres, sur support microforme, papier, électronique et/ou autres formats.

L'auteur conserve la propriété du droit d'auteur et des droits moraux qui protège cette thèse. Ni la thèse ni des extraits substantiels de celle-ci ne doivent être imprimés ou autrement reproduits sans son autorisation.

In compliance with the Canadian Privacy Act some supporting forms may have been removed from this thesis.

While these forms may be included in the document page count, their removal does not represent any loss of content from the thesis.

Conformément à la loi canadienne sur la protection de la vie privée, quelques formulaires secondaires ont été enlevés de cette thèse.

Bien que ces formulaires aient inclus dans la pagination, il n'y aura aucun contenu manquant.

Canada

ABSTRACT

Optical Spectroscopy of Photosynthetic Complexes: Focus on Low-Temperature Protein Dynamics

Nicoleta Herascu

To perform photosynthesis, plants, algae and bacteria possess well organized and closely coupled photosynthetic pigment-protein complexes. The information on energy transfer processes and protein dynamics contained in the narrow zero-phonon lines at low temperatures is hidden under the inhomogeneous broadening. Thus, it is difficult to analyze the spectroscopic properties of these complexes in sufficient detail by conventional spectroscopy methods. In this context, high resolution spectroscopy techniques such as Spectral Hole Burning, Fluorescence Line Narrowing and Single Molecule / Single Complex Spectroscopy are powerful tools designed to overcome the inhomogeneous broadening difficulty. This thesis focuses mainly on the low-temperature protein dynamics of several photosynthetic protein complexes (LH2, CP43, CP29 and LHCII). The hole growth kinetics and the shape of the anti-hole due to the non-photochemical spectral hole burning have been explored, and interpreted within the framework of theoretical models describing spectral diffusion due to conformational changes between nearly identical substates on a multi-tier protein energy landscapes.

ACKNOWLEDGEMENTS

I would like to express my gratitude to my supervisor Professor Valter Zazubovitch whose experience, guidance, and patience contributed tremendously to this thesis. I appreciate his experience, originality and spirit of discovery in regard to research and technology.

I would like to thank our group's collaborators for their valuable help in providing samples and scientific discussions.

It is an honor for me to thank to all of those who supported me in any respect during the completion of this master degree.

I must also acknowledge to NSERC for the financial support of this research.

TABLE OF CONTENTS

List of Tables

List of Figures

Fig. A1.1 The structural model of Photosystem I and the absorption spectrum of PS-I wild type where green – chlorophyll molecules, blue, pink, purple, orange, etc – protein alpha-helixes.

Fig. A1.2 Thermocycled spectral holes burned in to the absorption spectrum of *Synechocystis* PCC6803 at 660 nm (T=5K, 20K, 31K, 40K, 52K, 61K, 73K, 86K, 99K, 110K). The lowest-temperature spectrum is the deepest hole spectrum. The vertical line indicates the burn wavelength.

Fig. A1.3 Thermocycled spectral holes burned in the absorption spectrum of *Thermosynechococcus Elongatus* at 659.94 nm (T=5K, 19.5K, 30K, 40K, 50K, 69.4K, 85.1K, 100K, 119K, 146K). The lowest-temperature spectrum is the deepest hole spectrum

Table 5.1 Parameters to the best fit to the hole shape and HGK curves

Fitting parameter	**Parameter values**
phonon sideband	$S = 0.45 \pm 0.05$, $\omega_{\text{peak}} = 25$ cm^{-1}, Gaussian/Lorentzian fwhm of 22/40 cm^{-1}
homogeneous line width	distribution from ref. 65 based on the whole B850 DOS, peaked at 3.3 cm^{-1} (1.6 ps)
antihole, tier 1, shifts ~ 1 cm^{-1}	$\phi > 10^{-6}$, $\lambda_0 \leq 7.8$, $\sigma_\lambda \leq 0.1$; not observed in SHB experiments
antihole, tier 2, shifts ~ 7-10 cm^{-1}	fwhm = 35 ± 5 cm^{-1}, shift = 3 ± 1 cm^{-1}, $\lambda_0 = 10.3 \pm 0.2$, $\sigma_\lambda = 0.7 \pm 0.2$ ($\phi \approx 10^{-8}$)
Antihole, tier 3, shifts ~ 60 cm^{-1}	fwhm = 70 ± 10 cm^{-1}, shift = 60 ± 10 cm^{-1}, $\phi \approx 10^{-7}$; note that only several percent of molecules are capable of such large shifts

Table 5.2 Absorption features of LHCII

	Experimental results		Literature results				
Pigment	LHCII-monomer	LHCII-trimer	LHCII-monomer		LHCII-trimer		Aggregated LHCII-trimer 4.2K
			77K	4.5K	77K	4.5K	
Chl a	675.86 nm	675.46 nm 671.08 nm 661.54 nm	662 nm; [34, 87] 670 nm; [.34, 87] 678 nm; [34, 87]	676 nm [88] 671 nm [88] 661.5 nm [88]	670 nm; [34, 87] 676 nm; [34, 87]	676 nm [88] 671 nm [88] 661.5 nm[88]	676.3 nm[89] 671.9 nm [89] 662.0 nm[89]

Table 5.3 The summary of the HGK curves simulation parameters Fit parameters correspond to the lowest burn frequency, highlighted in bold

Complex	**CP43, A-state**	**CP29**	**LHCII monomer**	**LHCII trimer**
SDF peak and width (cm^{-1})	14641; 180	14717, 165 [1]	14705; 198 [2]	14717, 180 [3]
Oscillator strength (Chl *a* equivalents)	1	1.0-0.7	1.2	1.2
Lifetime τ_1 (ns)	3.5	4.8	4.4	4.4
Γ_{homog} **(cm^{-1})**	0.03	0.04	0.04	0.04
Burn frequency ω_B (cm^{-1})	**14560**	**14670** 14694 14720	**14616,** 14628, 14653	**14640** 14652 14656
S_{PSB}	0.30±0.05	0.60±0.05	0.80±0.05[4]	1.3±0.1
ω_m; Γ_{Gauss}; $\Gamma_{Lorentz}$ **(cm^{-1})**	17; 15; 70	22; 20; 110	22; 20; 110[4]	22,20,110
λ_0	11.0±0.2	9.6±0.2	11.3±0.2[4]	11.2±0.2
σ_λ	1.0±0.05	1.4±0.2	2.0±0.2	2.3±0.2

[1] SDF parameters from [79]: peak 14745 cm^{-1}, FWHM=120 cm^{-1}, S=0.4...0.6.

[2] SDF parameters from [88]: peak 14715 cm^{-1}, FWHM=110 cm^{-1}, S=0.6

[3] SDF parameters from [88]: peak 14705 cm^{-1}, FWHM=80 cm^{-1}; S=0.8...0.9

[4] The best fit with electron-phonon coupling parameters exactly as in [88] yields λ_0=12.0

Table A2: Summary of the experiments performed

Species	*Rps. Acidophila*
Complex studied	**LH2**
Provider/collaborator	Cogdell, U. Glasgow
Experiment type	HB Spectra, hole broadening on a time scale of hours and HGK
Species	*Spinach*
Complex studied	**CP43**
Provider/collaborator	Seibert and Picorel, NREL, Colorado
Experiment type	HB Spectra and HGK
Species	*Spinach*
Complex studied	**CP29**
Provider/collaborator	Pieper and Irrgang, Berlin
Experiment type	HB Spectra and HGK
Species	*Pea*
Complex studied	**LHC-II**
Provider/collaborator	Nethan Nelson, U. Tel Aviv, Israel
Experiment type	HB Spectra and HGK
Species	*Synechocystis PCC6803* and *Synechococcus elongatus*
Complex studied	**PS I**
Provider/collaborator	T.W. Johnson / Petra Fromme ASU
Experiment type	Thermocycling of the whole satellite hole structure.

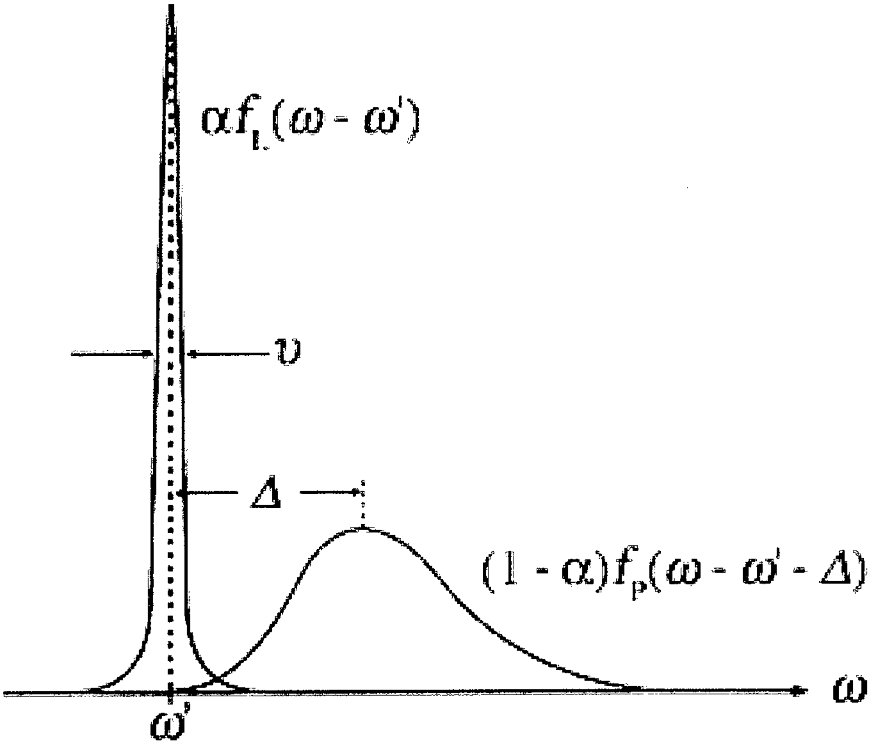

Fig. 1.1 Debye – Waller factor and schematic absorption line shape of guest molecules in perfect lattice (from ref. [9 and 19])

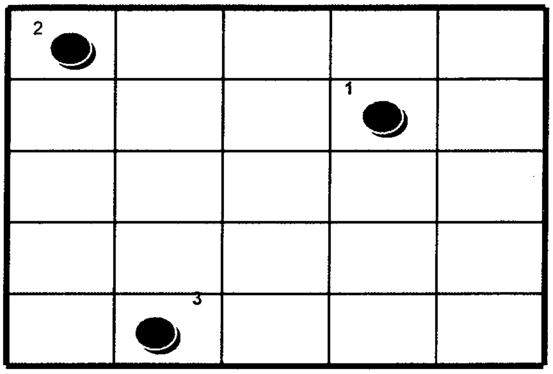

Fig. 1. 2 Identical guest molecules in a perfect lattice (after ref. [8, 9])

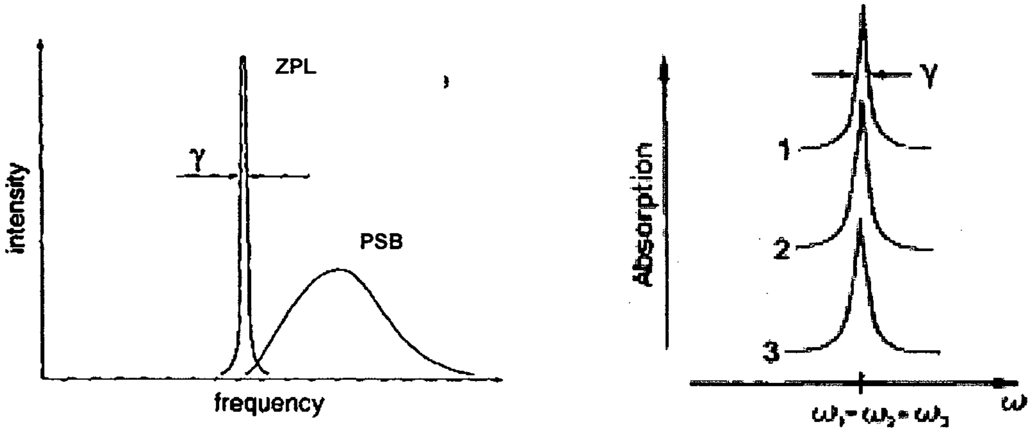

a. b.

Fig. 1. 3 Absorption line shape of guest molecules in perfect lattice
a. absorption line shape of a single guest molecule in a perfect lattice;
b. Homogeneous lines of identical guest molecules in a perfect lattice (from ref. [8, 9])

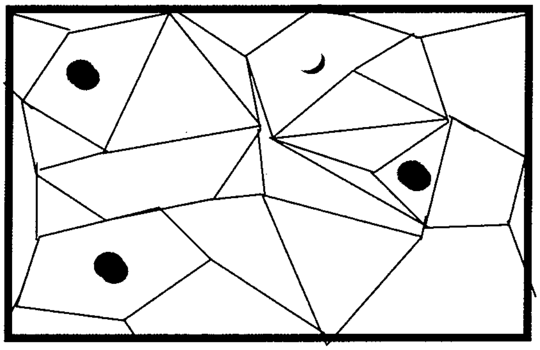

Fig. 1.4 A disordered lattice doped with guest molecules (after ref. [8, 9])

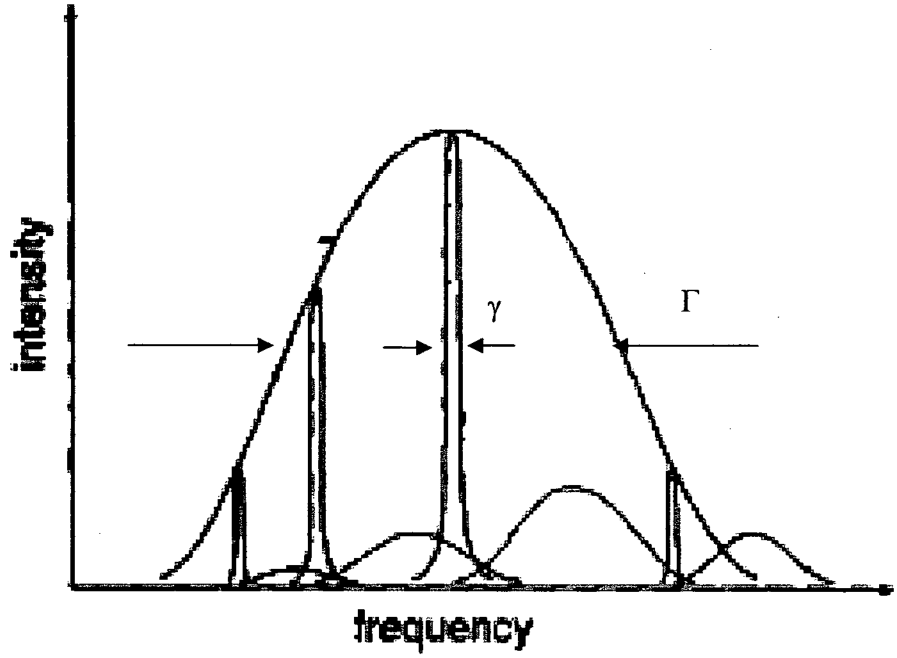

Fig. 1.5 Absorption line shape of guest molecules in disordered lattice
Γ - inhomogeneous lines width; γ - homogeneous lines width (from ref. [8, 9])

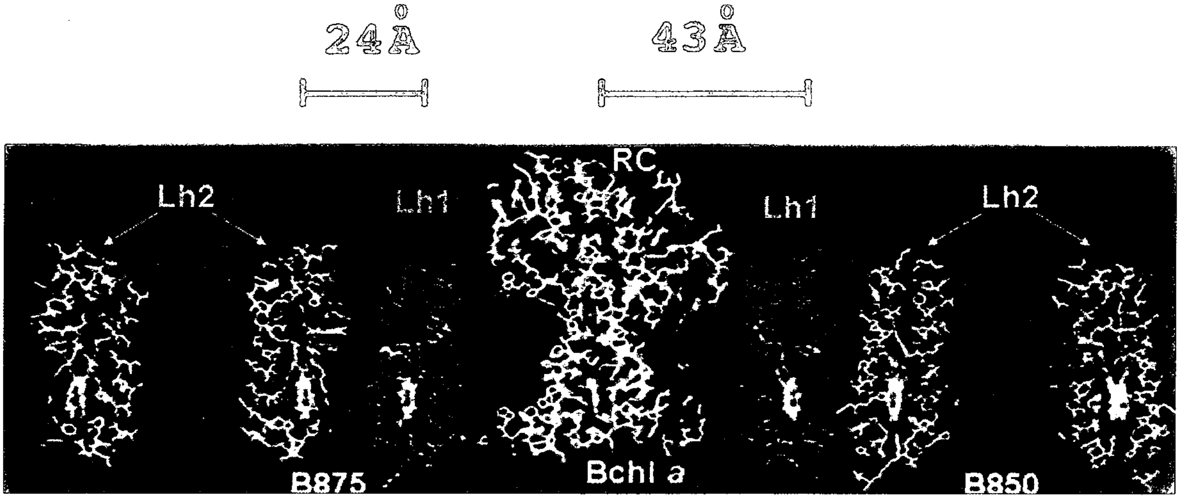

Fig. 2.1 X-ray structure of the photosynthetic unit in purple bacteria, *R. molischianum* (from ref. 4), including the reaction center, LH1 and LH2.

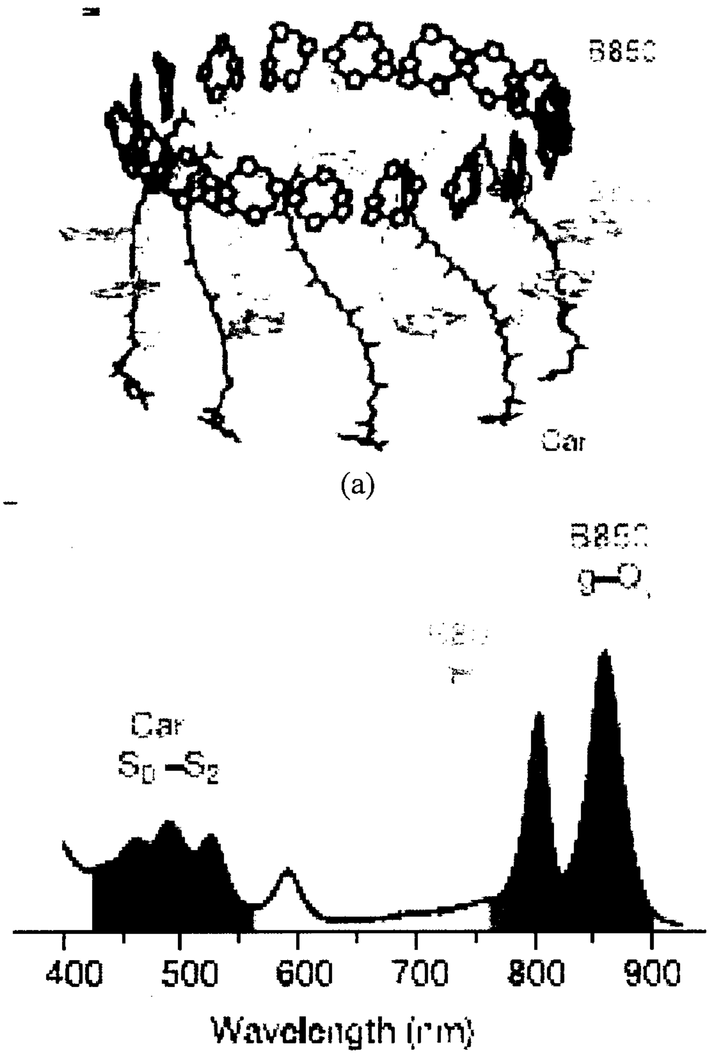

(a)

(b)

Fig. 2.2 The structure of the peripheral LH2 complex from *Rsp. Acidophila* (a) and the absorption spectrum of lh2 from *Rsp. Acidophila* (b) (from and ref. 17; 18)

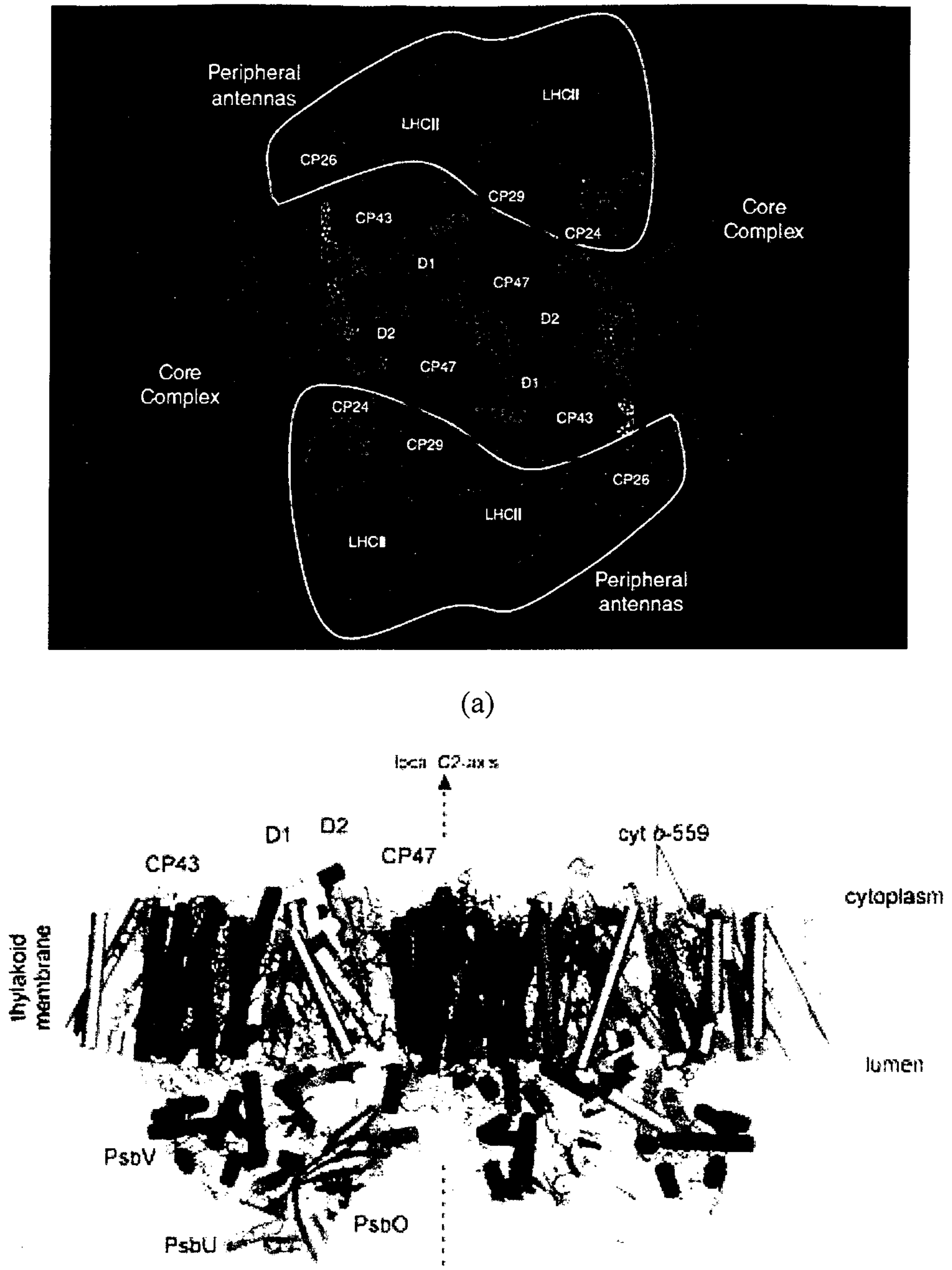

(a)

(b)

Fig. 2.3 Structure of PS II - (a) view from above and (b) side view along the membrane plane of dimeric PSII (from http://www.lbl.gov/Science-Articles/Archive/PBD-CP29.html and http://www.sciencemag.org/feature/data/prizes/ge/2006/loll_figure.gif)

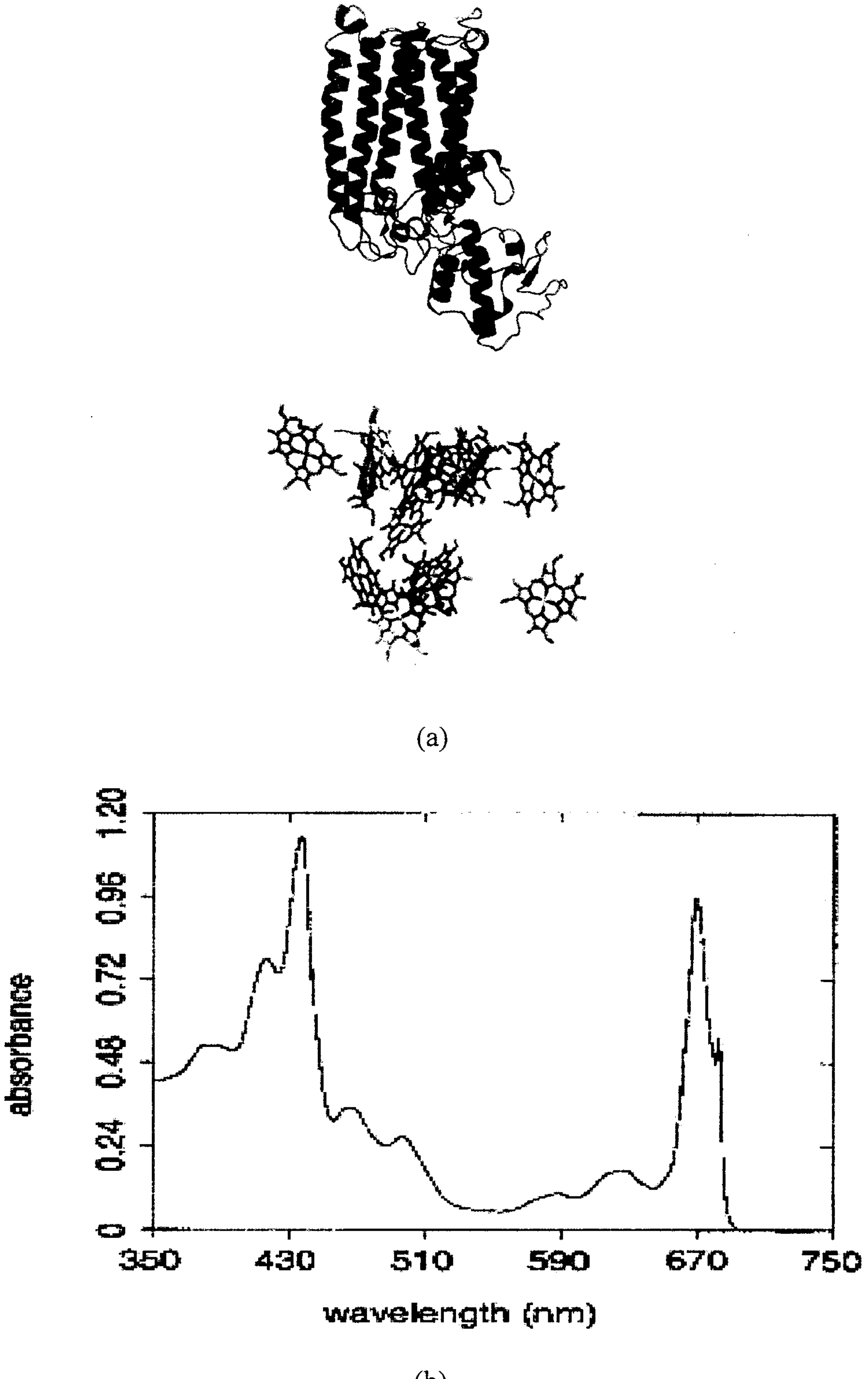

(a)

(b)

Fig. 2.4 Structure (the complete structure and the organization of chlorophylls) and low-temperature absorption spectrum of CP43 (from ref. 19, 20)

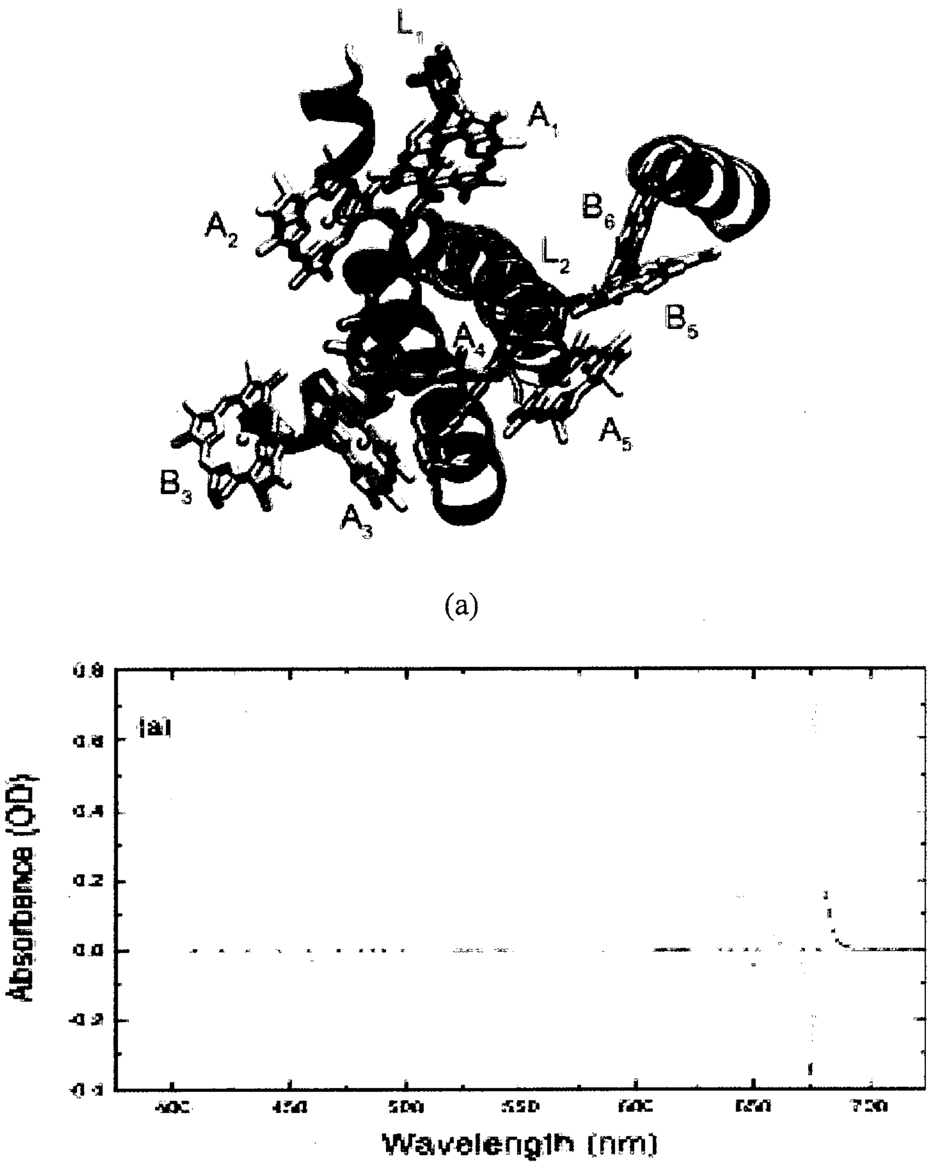

(a)

(b)

Fig. 2.5 Structure and absorption spectrum (with second derivative) of CP29 (from www.lbl.gov/.../Archive/PBD-CP29.html; ref. 21)

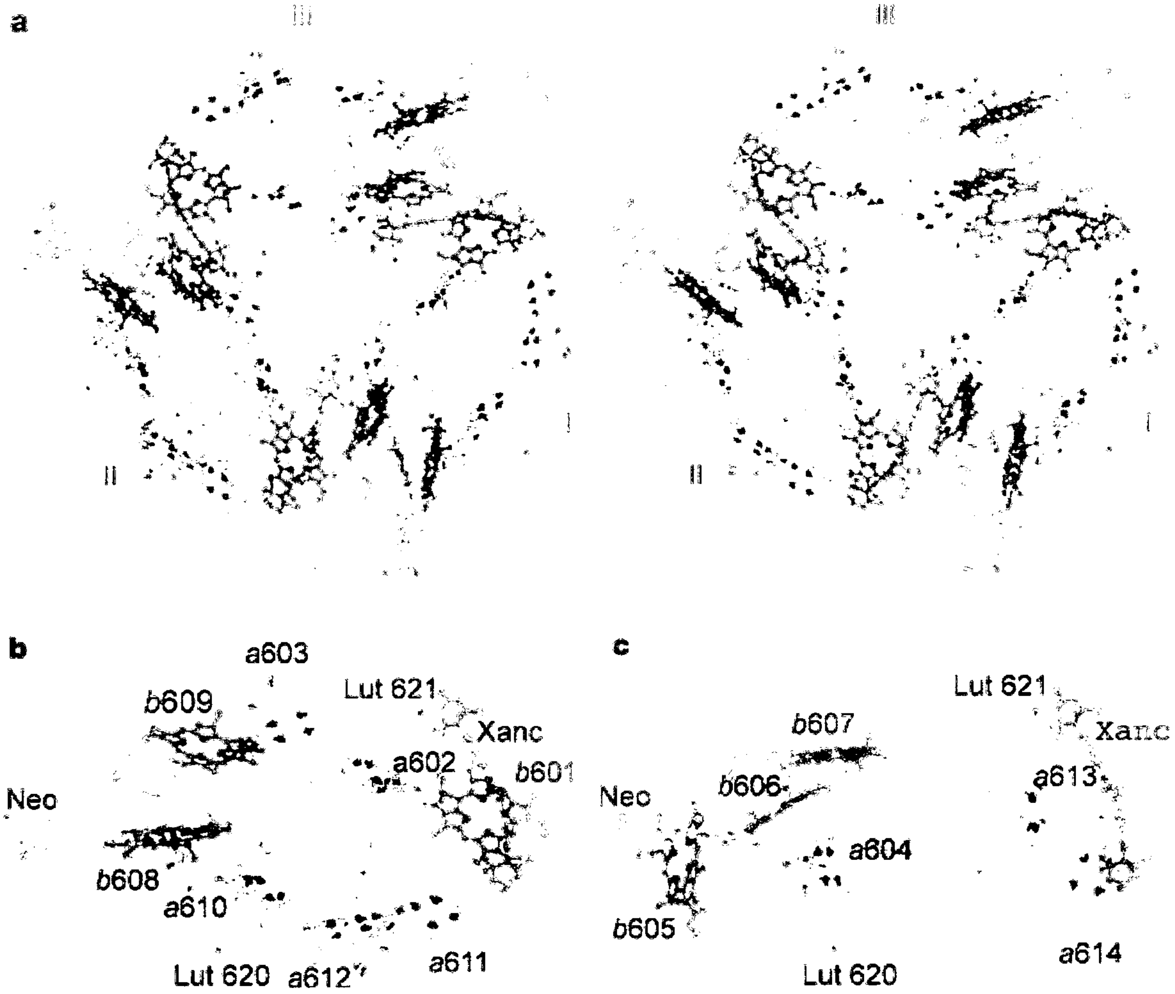

Fig. 2.6 The trimeric and monomeric structure of LHC-II; a – pigments in the LHC-II trimer, view along the membrane normal from the stromal side; b and c, d – pigments in the LHC-II monomer, view at the stromal and lumenal sides, respectively (from ref. 27)

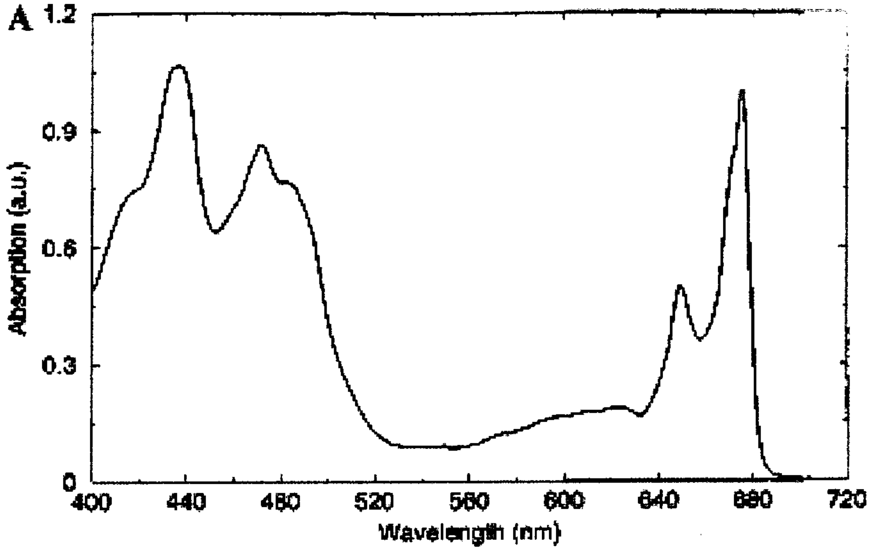

Fig. 2.7 The low-temperature absorption spectra of LHC-II (from ref. 26)

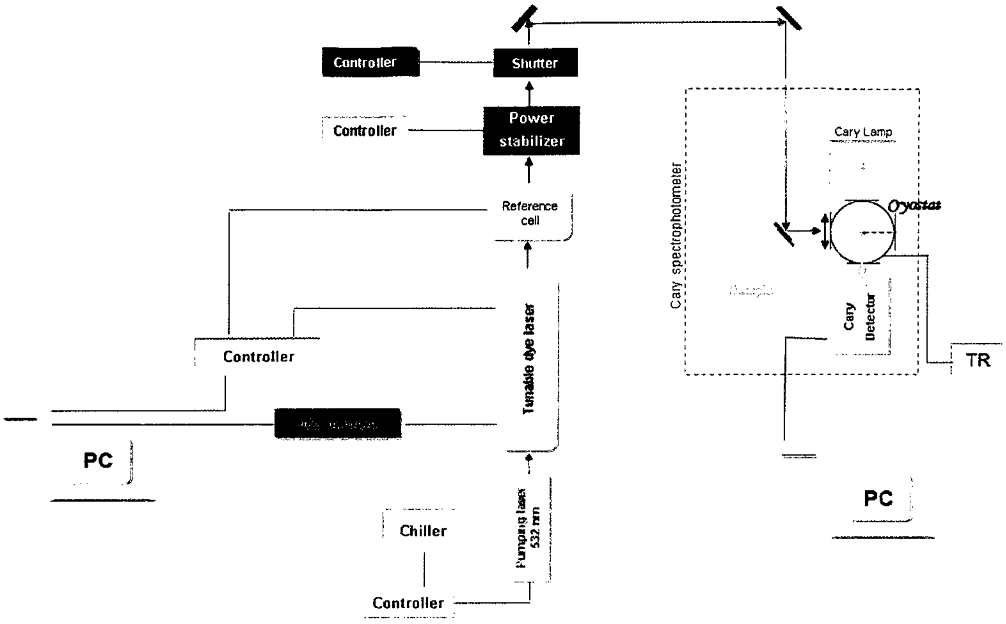

Fig. 3.1 Absorption and low-resolution HB set-up

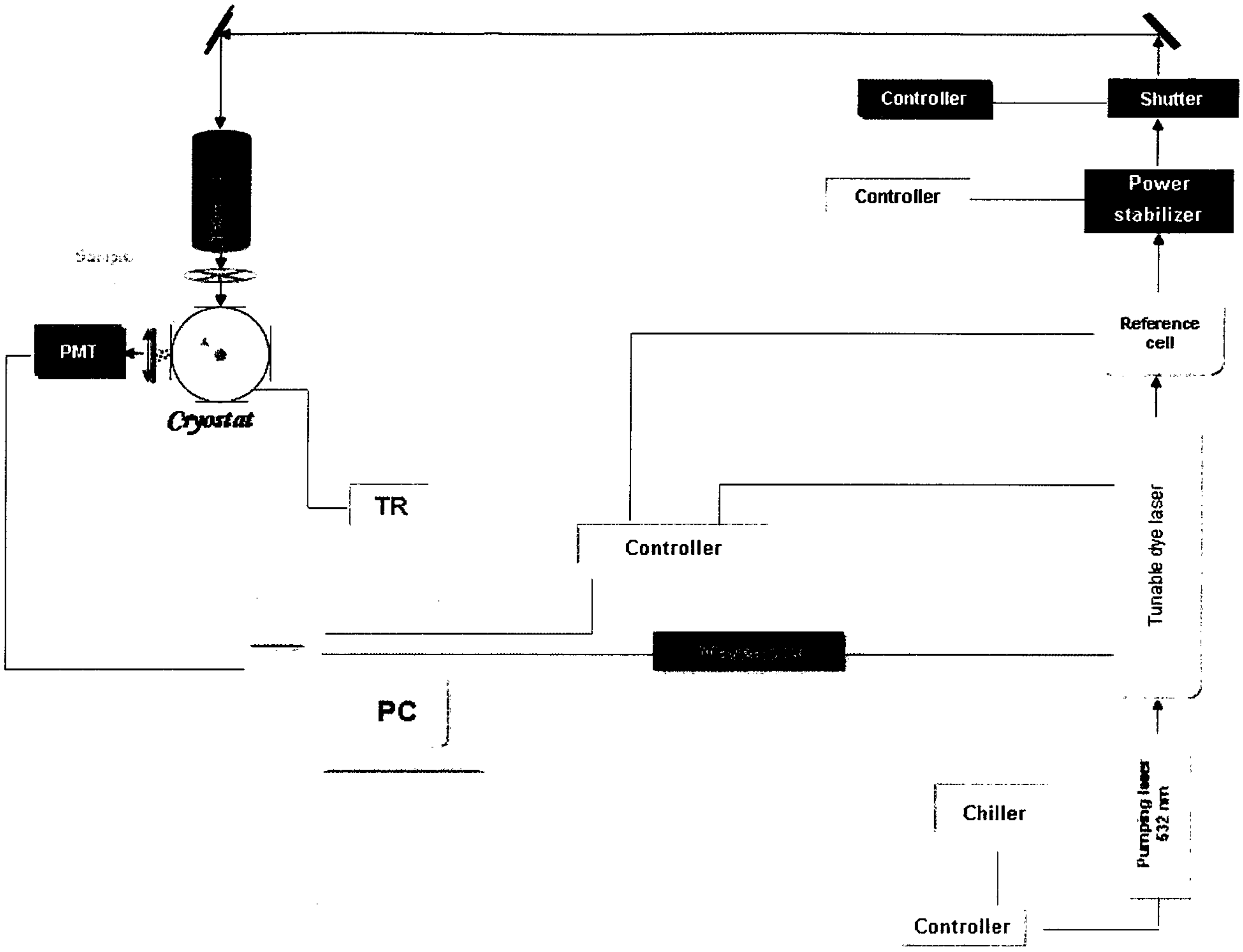

Fig. 3.2 Fluorescence excitation mode set-up

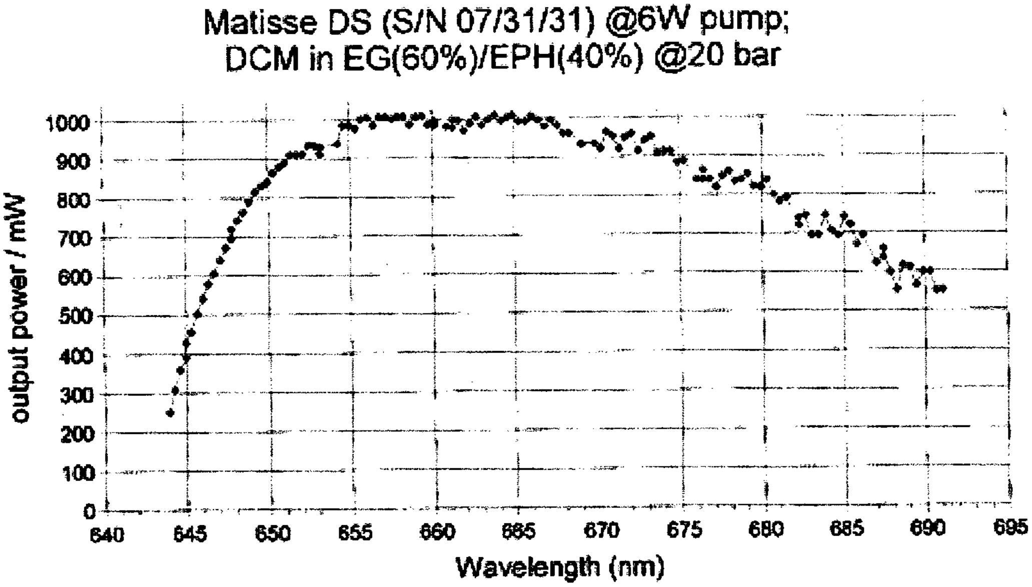

Fig. 3.3 DCM-dye calibration curve (from ref. [30])

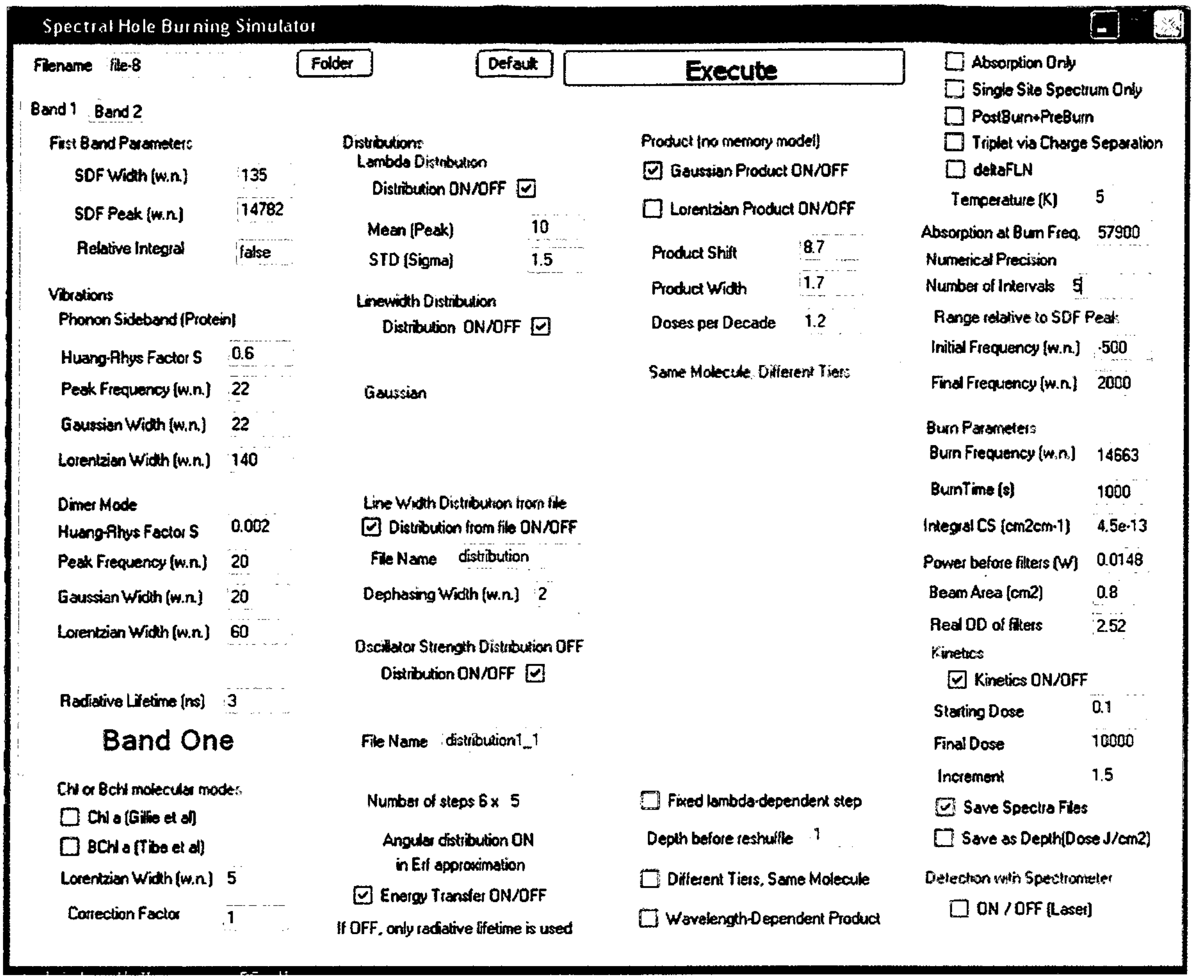

Filename file-8

First Band Parameters
SDF Width (w.n.) 135
SDF Peak (w.n.) 14782
Relative Integral false

Vibrations
Phonon Sideband (Protein)
Huang-Rhys Factor S 0.6
Peak Frequency (w.n.) 22
Gaussian Width (w.n.) 22
Lorentzian Width (w.n.) 140

Dimer Mode
Huang-Rhys Factor S 0.002
Peak Frequency (w.n.) 20
Gaussian Width (w.n.) 20
Lorentzian Width (w.n.) 60

Radiative Lifetime (ns) 3

Chl or Bchl molecular modes
☐ Chl a (Gillie et al)
☐ BChl a (Tiba et al)
Lorentzian Width (w.n.) 5
Correction Factor 1

Distributions
Lambda Distribution
Distribution ON/OFF ☑
Mean (Peak) 10
STD (Sigma) 1.5

Linewidth Distribution
Distribution ON/OFF ☑

Gaussian

Line Width Distribution from file
☑ Distribution from file ON/OFF
File Name distribution
Dephasing Width (w.n.) 2

Oscillator Strength Distribution OFF
Distribution ON/OFF ☑

File Name distribution1_1

Number of steps 6 x 5

Angular distribution ON
in Erf approximation
☑ Energy Transfer ON/OFF
If OFF, only radiative lifetime is used

Product (no memory model)
☑ Gaussian Product ON/OFF
☐ Lorentzian Product ON/OFF
Product Shift 8.7
Product Width 1.7
Doses per Decade 1.2

Same Molecule, Different Tiers

☐ Fixed lambda-dependent step
Depth before reshuffle 1
☐ Different Tiers, Same Molecule
☐ Wavelength-Dependent Product

☐ Absorption Only
☐ Single Site Spectrum Only
☐ PostBurn+PreBurn
☐ Triplet via Charge Separation
☐ deltaFLN
Temperature (K) 5
Absorption at Burn Freq. 57900
Numerical Precision
Number of Intervals 5
Range relative to SDF Peak
Initial Frequency (w.n.) -500
Final Frequency (w.n.) 2000

Burn Parameters
Burn Frequency (w.n.) 14663
BurnTime (s) 1000
Integral CS (cm2cm-1) 4.5e-13
Power before filters (W) 0.0148
Beam Area (cm2) 0.8
Real OD of filters 2.52
Kinetics
☑ Kinetics ON/OFF
Starting Dose 0.1
Final Dose 10000
Increment 1.5
☑ Save Spectra Files
☐ Save as Depth(Dose J/cm2)
Detection with Spectrometer
☐ ON / OFF (Laser)

Fig. 3.4 Interface of Spectral Hole Burning Simulator

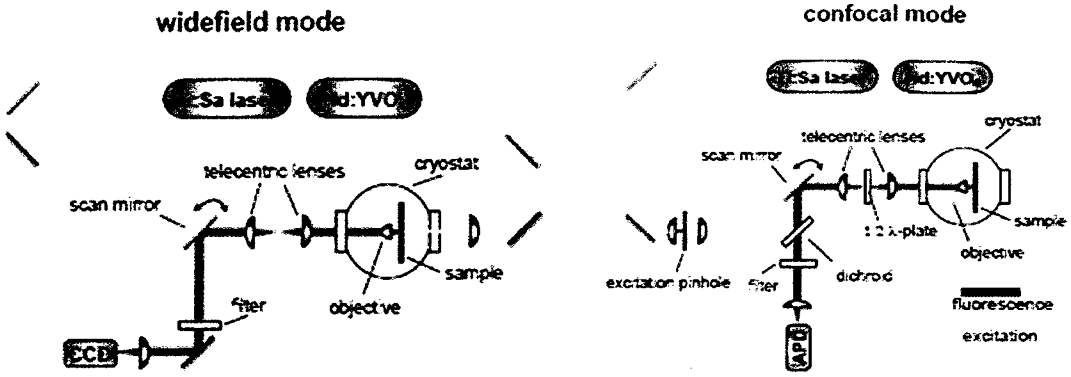

a) b)

Fig. 3.5 Single-molecule spectroscopy; (a) diagram of the widefield arrangement of the microscope; (b) diagram of the confocal arrangement of the microscope (from ref. 46)

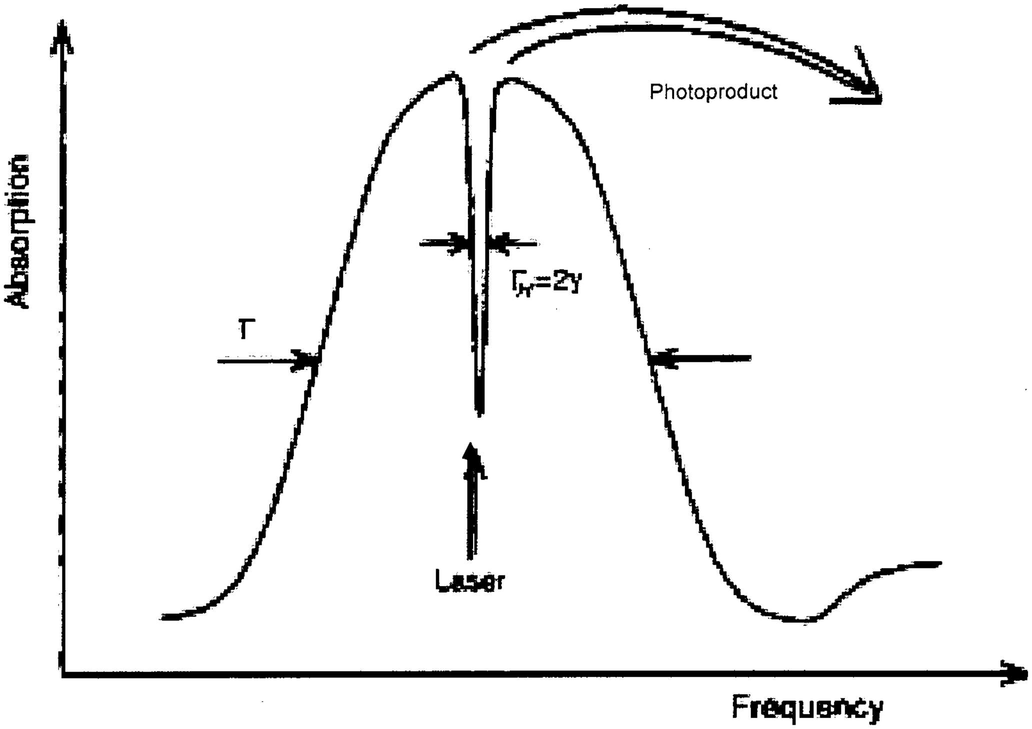

Fig. 4.1 Zero phonon hole (after ref [9])

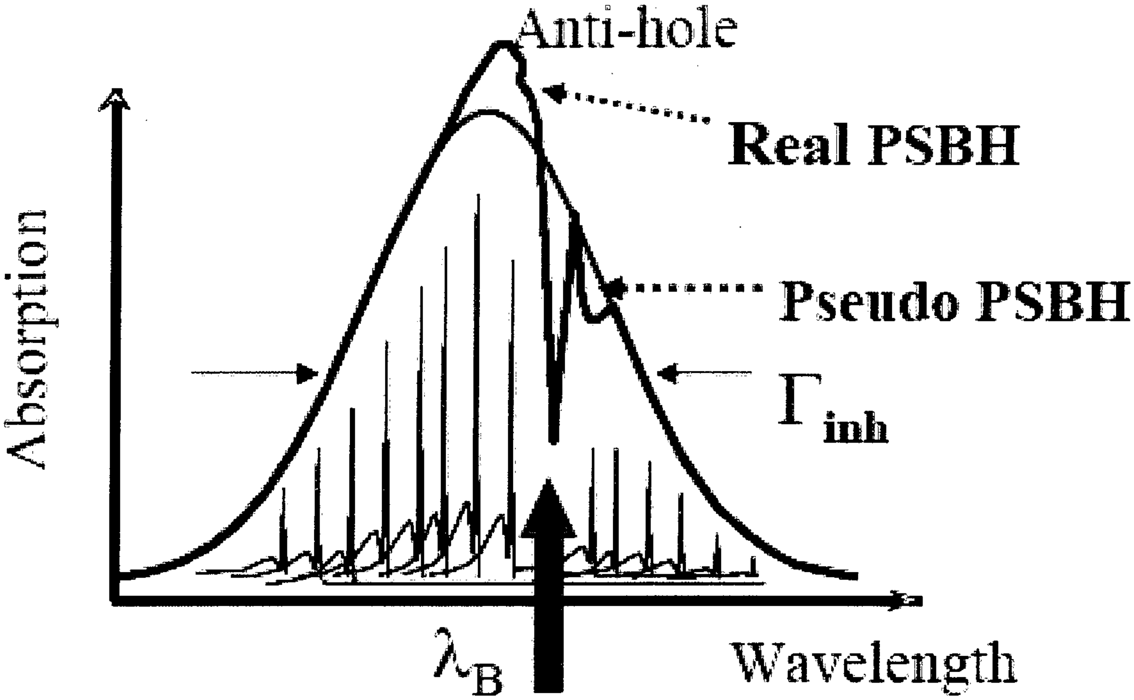

Fig. 4.2 Non-photochemical hole profiles burnt non-resonantly (from ref. [16])

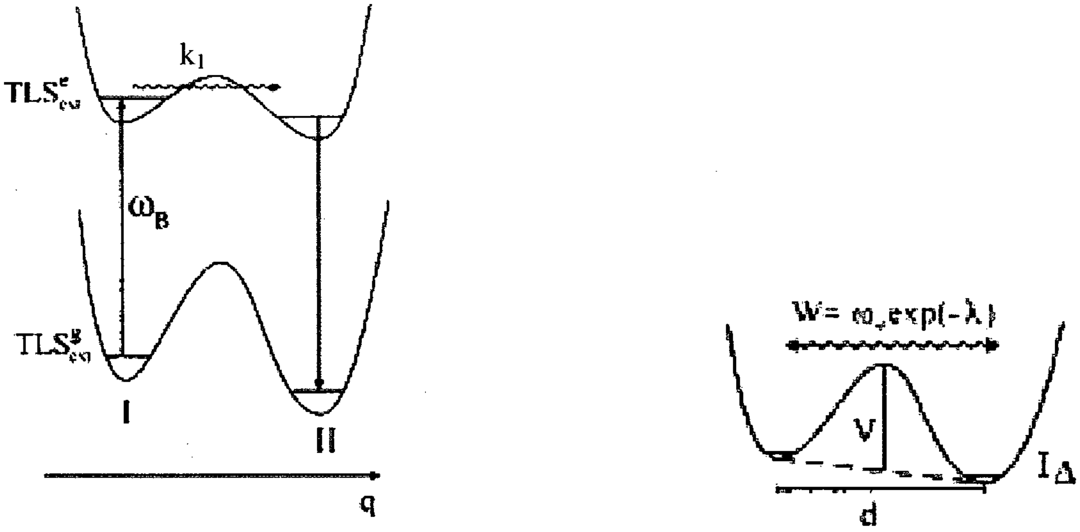

Fig. 4.3 (a) Two-level (referred to as I and II) system model (where indices "e" and "g" indicate the chromophore in its excited and ground state, ω_B is the burn frequency of the laser, and k_I is the tunneling rate, I/II denote the preburn/postburn chromophore host configurations);
(b) The TLS parameters (where *W* is the tunneling frequency), (from ref [12])

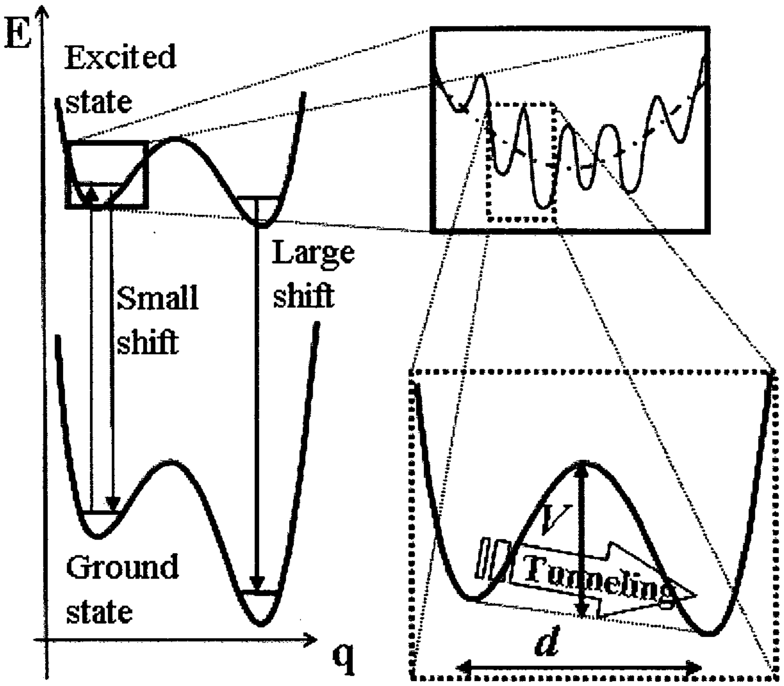

Fig. 4.4 NPHB mechanisms accounting the different hierarchical tiers on the energy landscape (from ref. 38)

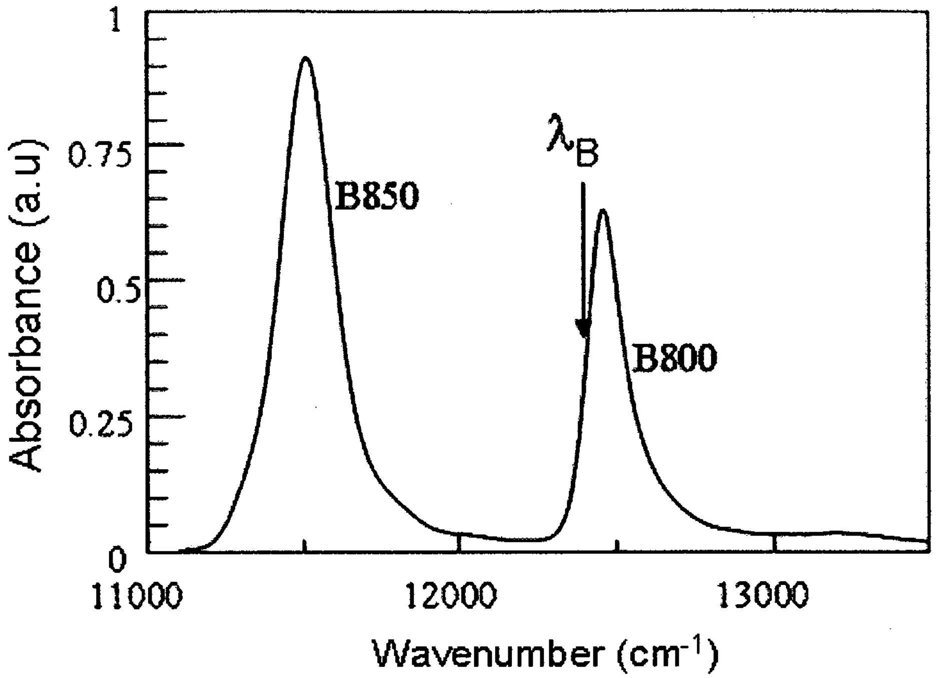

Fig. 5.1 Low temperature (T=5K) absorption spectra of LH2 from *Rsp. Acidophila*

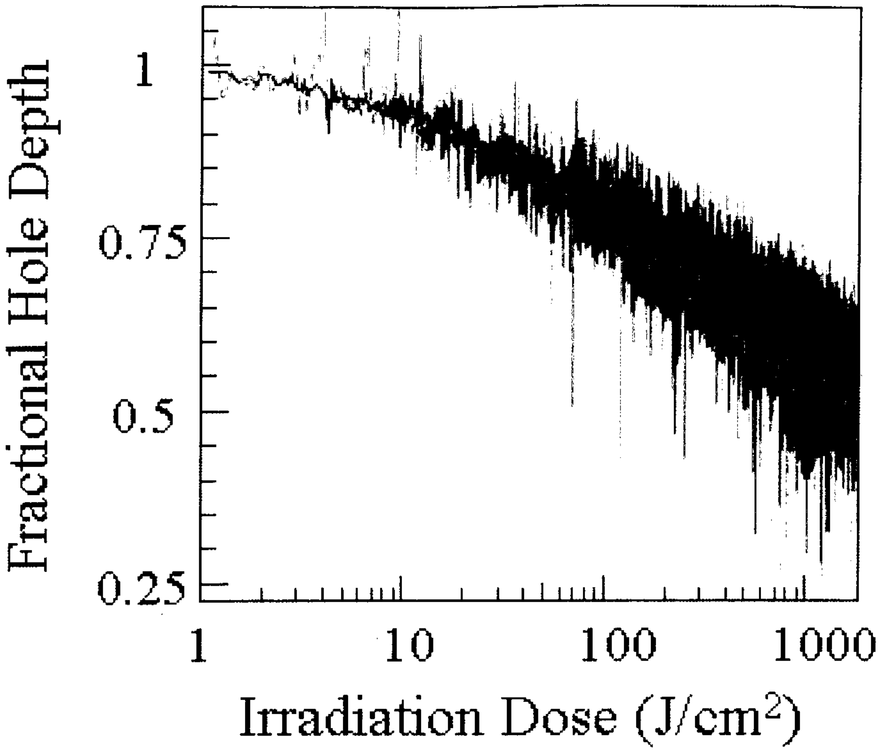

Fig. 5.2 HGK curves obtained at 0.23 W/cm^2 (0.5 s/point; dark gray curve) and 1.37 W/cm^2 (0.1 s/point; light gray curve) at 807.5 nm, as well as hole depths extracted from the spectral holes (red circles for data as measured, blue circles - for data corrected for white-light-induced hole filling, see ref 38 for details on LIHF)

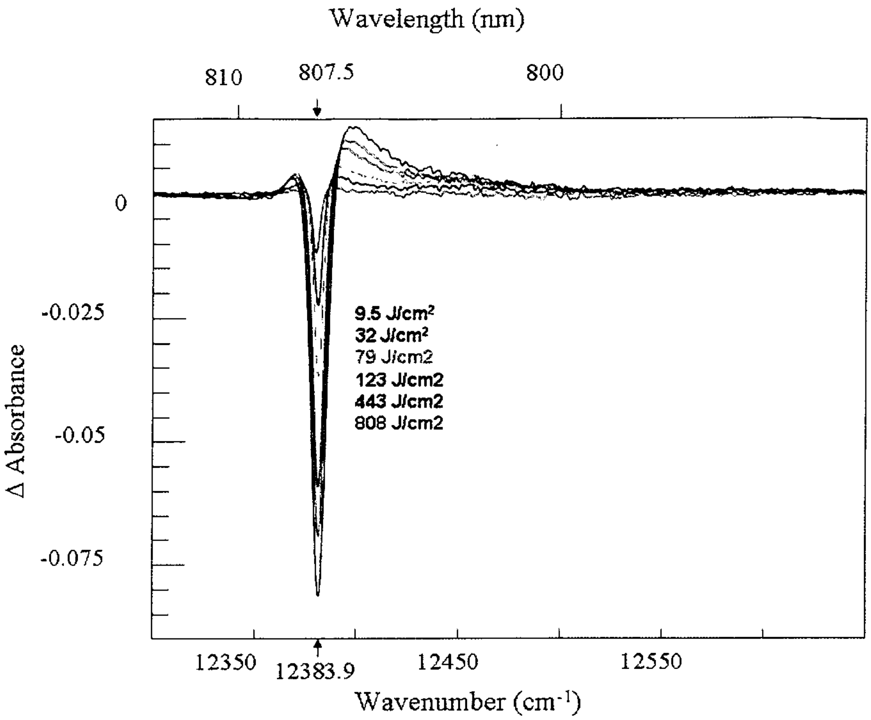

Fig. 5.3 NPHB of LH2 complex of *Rsp. Acidophila* (λ_B = 807.5 nm) for various irradiation doses

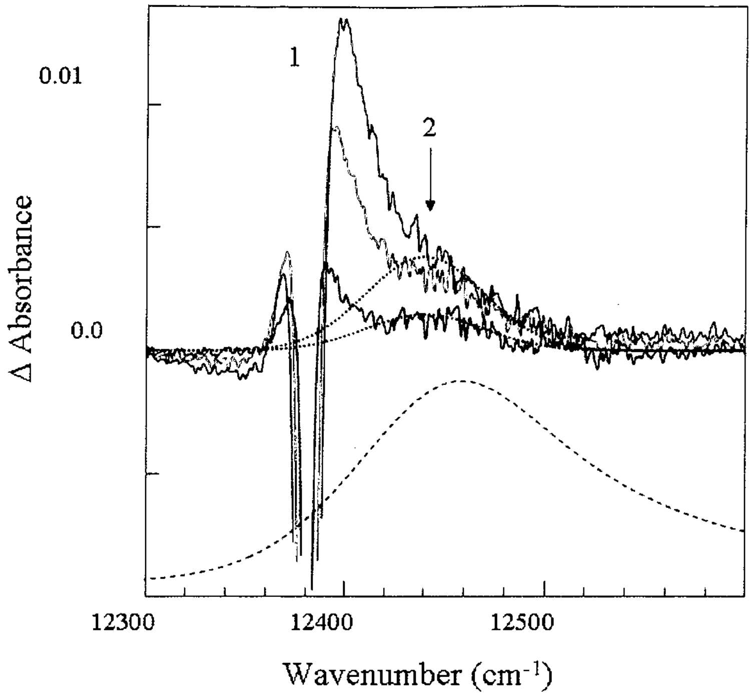

Fig. 5.4 NPHB anti-hole structure for Lh2 complex of *Rsp. Acidophila,* where the numerals 1 and 2 refer to different contributions to the NPHB antihole; dotted curves are the fit to the second, strongly shifted component of the antihole (labeled with the downward arrow); the dashed curve is the B800 absorption

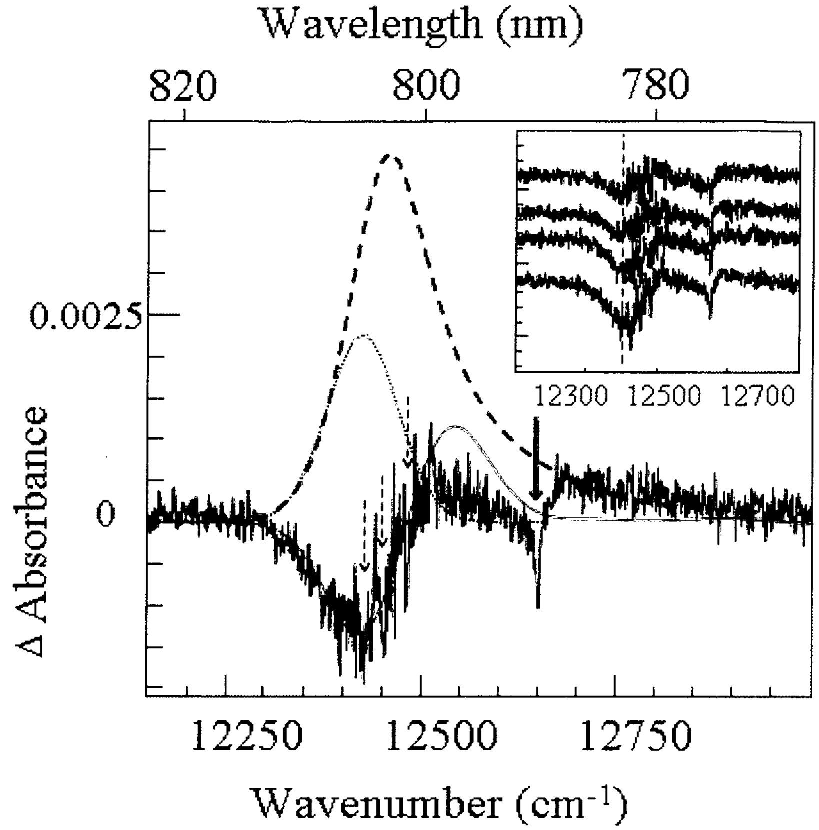

Fig. 5.5 Non-resonantly burned hole spectrum of LH2 complex of *Rsp. Acidophila* (λ_B = 790 nm and 150 J/cm^2), where the dotted line is the fit to the SHB action spectrum, and the dashed line is the B800 absorption band (multiplied by a factor of 0.003); the thin red solid curve represents the hole due to EET and its antihole; dashed arrows show vibronic replicas of the resonant hole; the inset contains nonresonantly SHB for different irradiation doses (50, 85, 100, and 150 J/cm^2, from top to bottom)

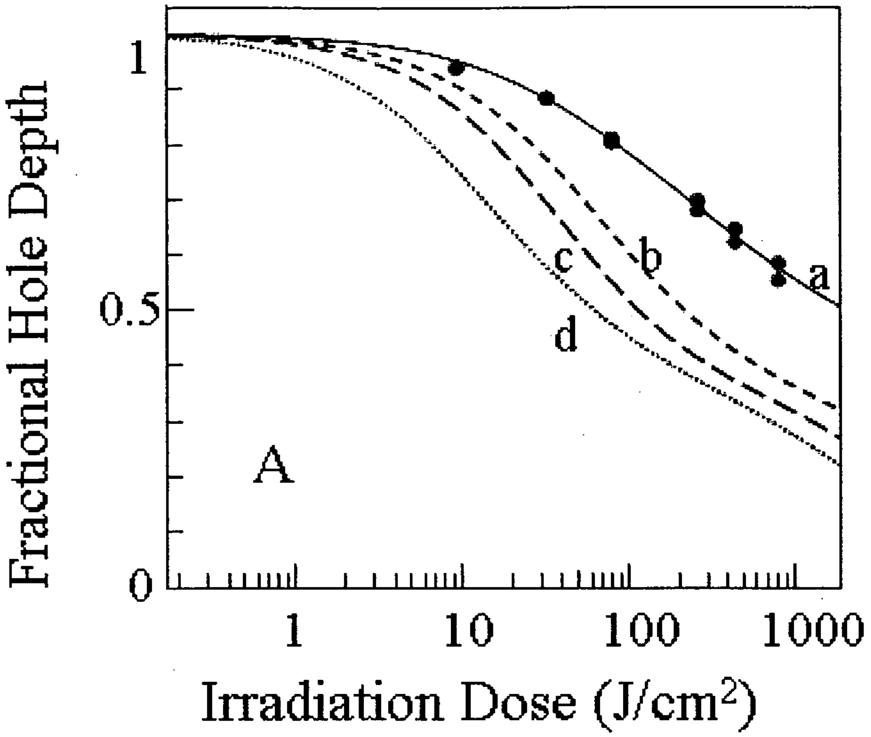

Fig. 5.6 The HGK calculated curves for $\lambda_0 = 7.8$, $\sigma_\lambda = 0$ and various shapes of the anti-hole function

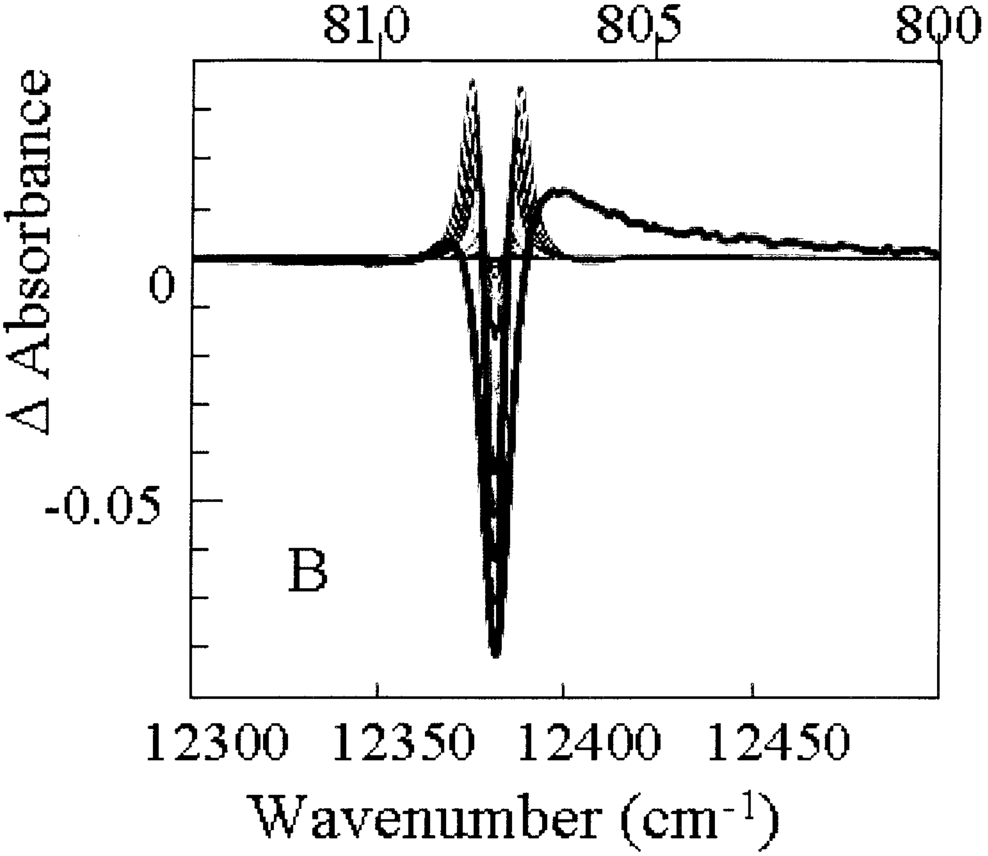

Fig. 5.7 The spectral hole burnt at λ_B = 807.5 nm and the spectral hole calculated for λ_0 = 7.8, σ_λ = 0, non-shifted Gaussian anti-hole function with the width of 1.1 cm^{-1} and several irradiation doses.

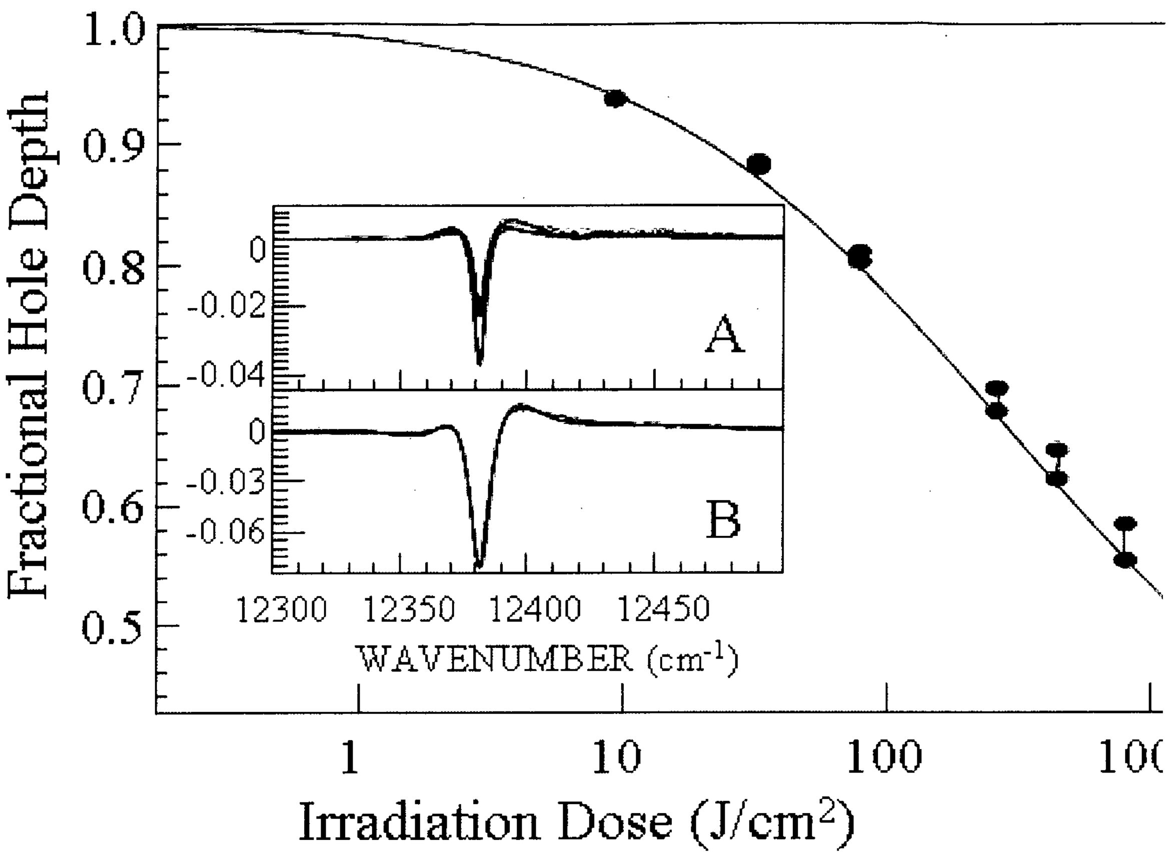

Fig. 5.8 The best fit to HGK and the overall shape fit of the shallowest and deepest holes in the series burned at 807.5 nm (inset A and inset B respectively). The blue and red noisy curves are the experimental holes.

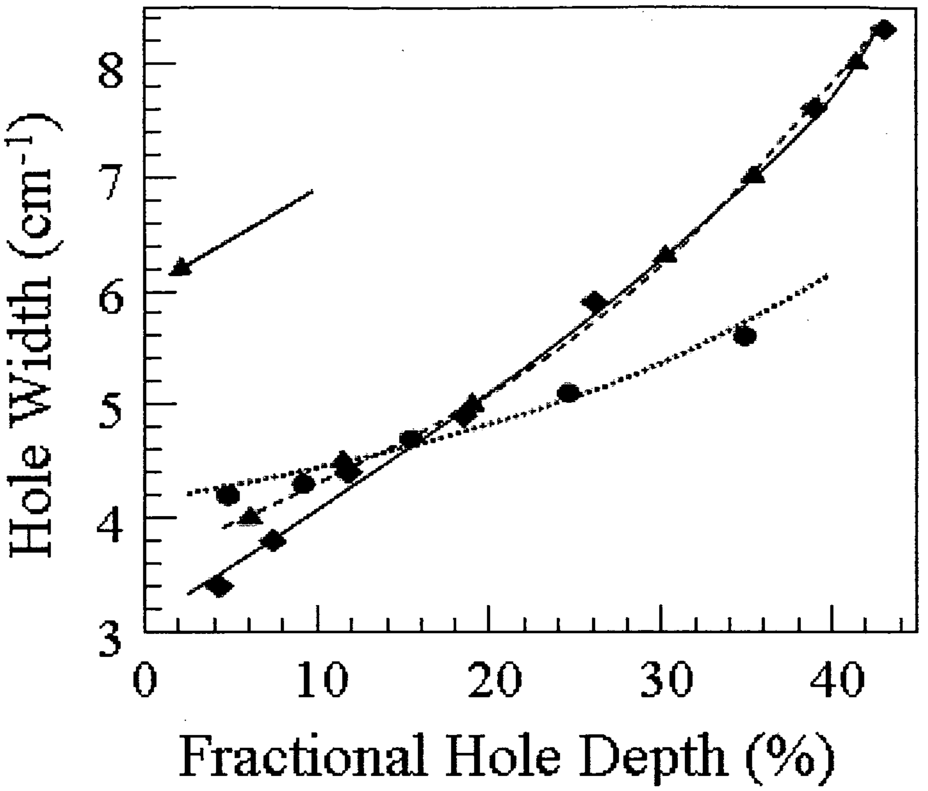

Fig. 5.9 Experimental dependence of the hole width on the fractional hole depth (triangles, dashed line), predicted dependence (based on eq. 4.5) in the absence of a homogeneous line width distribution (circles, dotted line), and predicted dependence assuming the distribution of line widths from ref 63 (diamonds, solid line). The value of the (shallow) hole width expected based on the time-domain data (i.e., about 6 cm^{-1}) is indicated by an arrow.

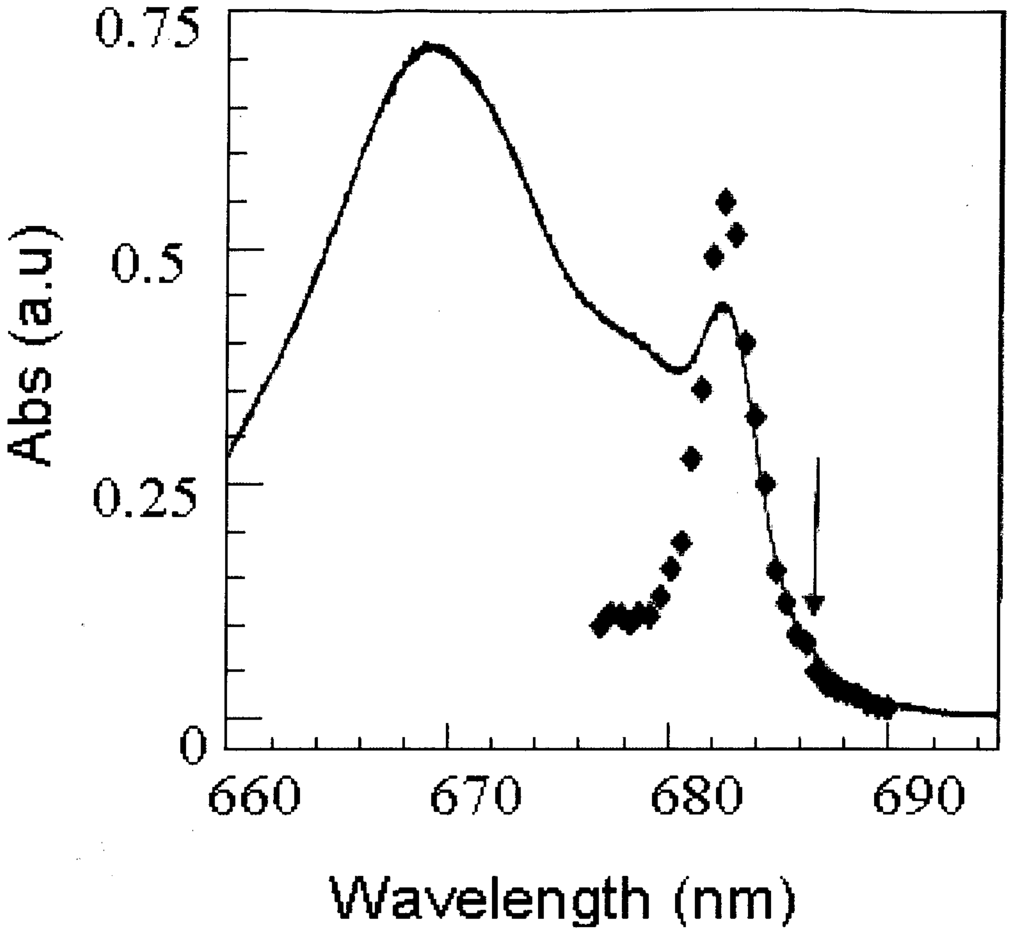

Fig. 5.10 Low temperature absorption spectrum of CP43 (red curve) and the SHB action spectrum of CP43 (black diamonds); the black pointed arrow indicates the burning wavelength (λ_B = 686.8 nm)

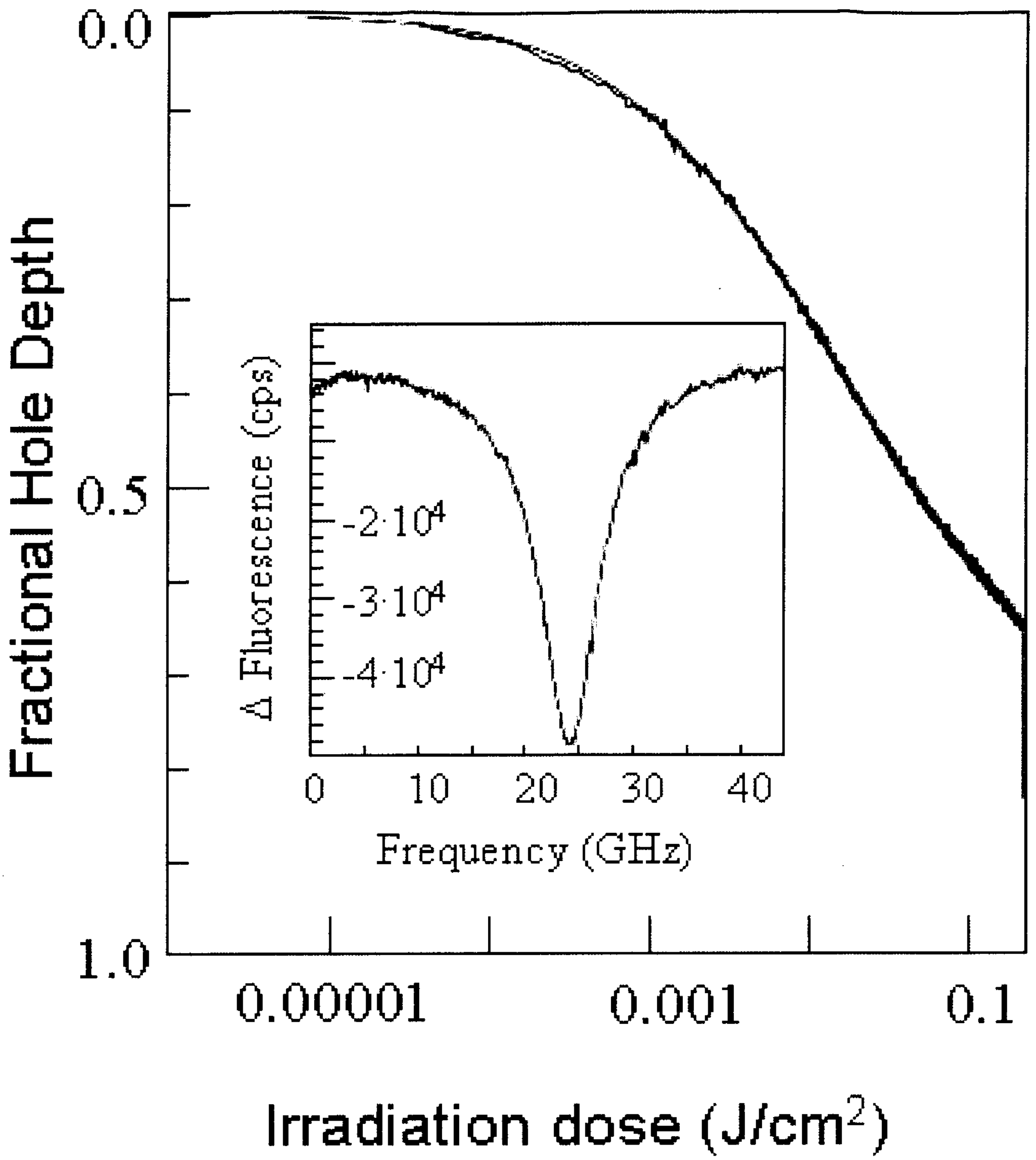

Fig. 5.11 The experimental (black noisier curve) and the best fit (based on eq. 4.5; red curve) to the hole growth kinetics curve of CP43; the insert shows the spectral hole burnt at 686.8 nm

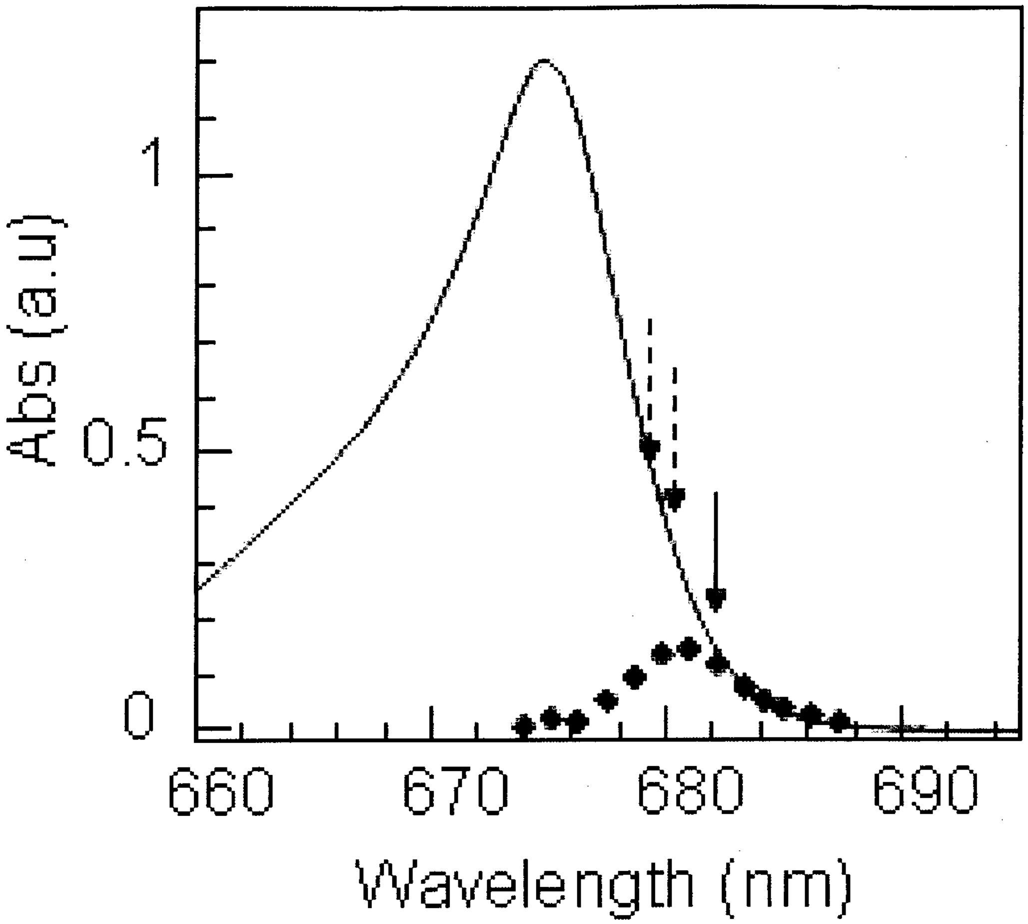

Fig. 5.12 Low temperature (T=5K) absorption spectrum of CP29 (red curve) and the SHB action spectrum of CP29 (black diamonds); the arrows indicate the burning wavelengths

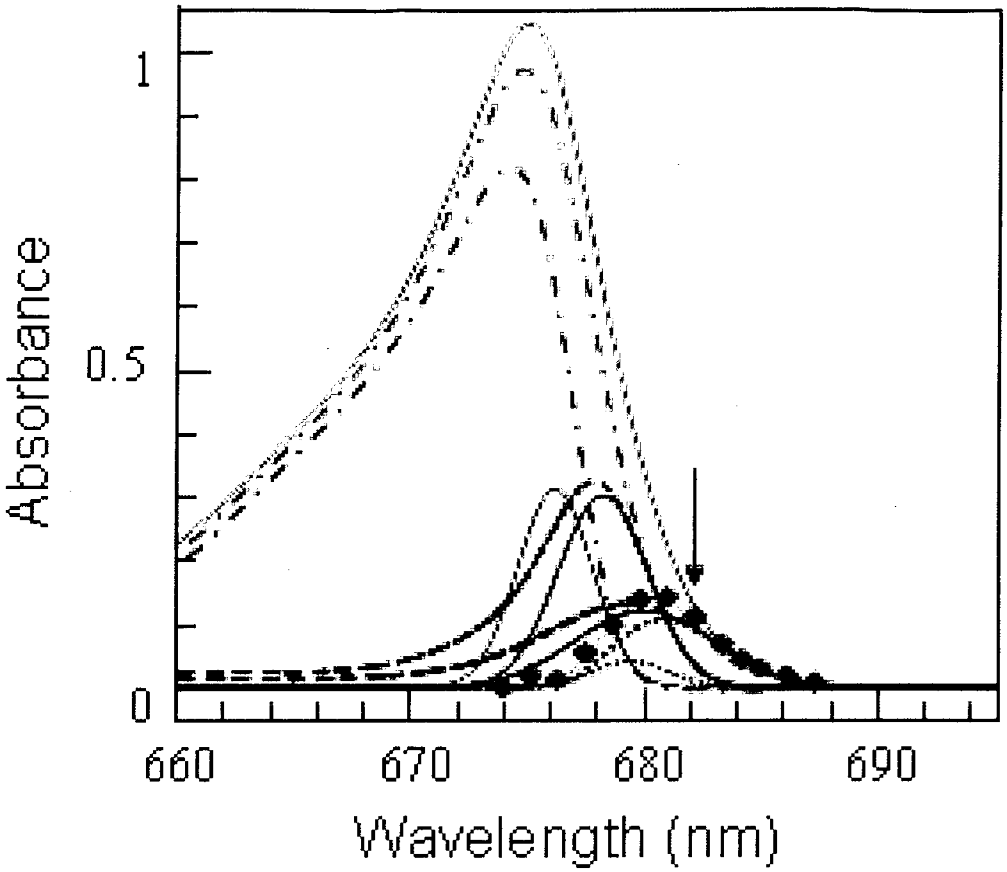

Fig. 5.13 The SDF and the absorption spectrum of the lowest – energy state of CP29; where the dashed blue curve is the pigment 1 SDF corrected with phonons and localized vibrations contribution [82]; dash-dotted red curve is the difference between the whole absorption spectrum (solid red curve) and the lowest-state absorption (dashed blue curve); black and green solid curves are the second and third-lowest energy SDFs; dashed black curve is the absorption spectrum of pigment 2 dressed with phonon and vibration contributions; black dotted curve is SDF of pigment 2 molecules incapable of downhill EET (divided by 3 for clarity, to avoid overlapping with other curves).

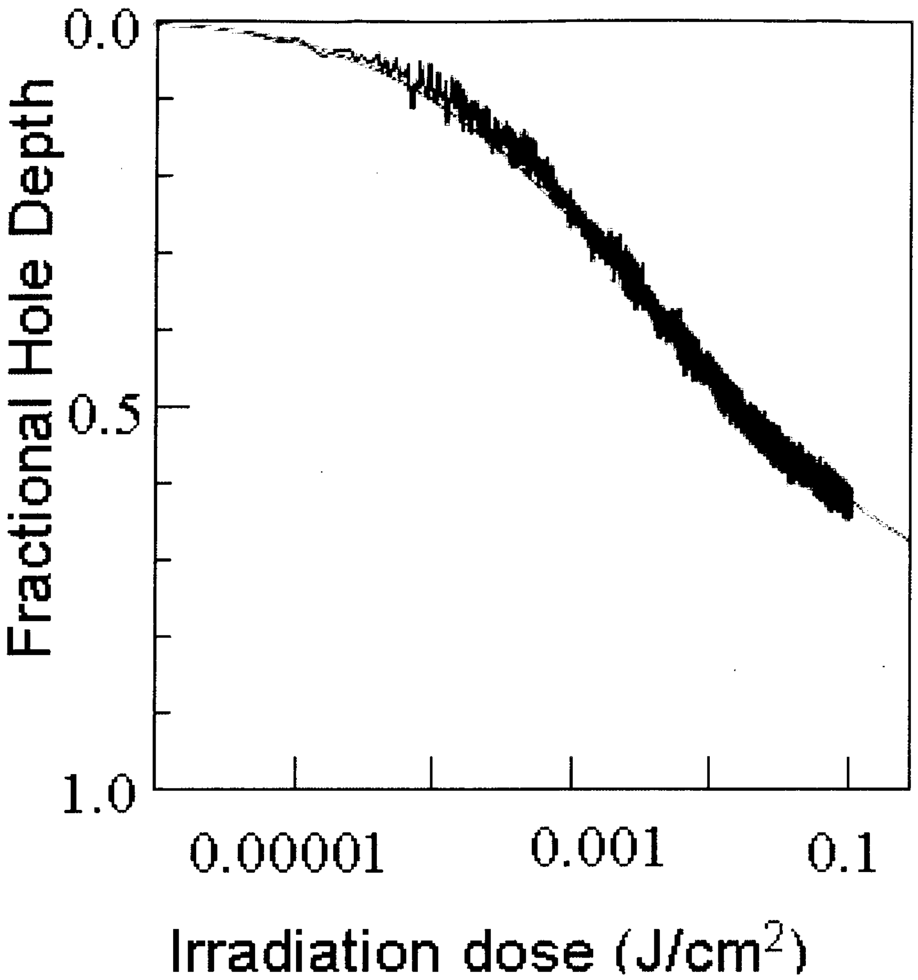

Fig. 5.14 The experimental HGK curves and the best fit to HGK of CP29 for burn wavelength of 681.7 nm

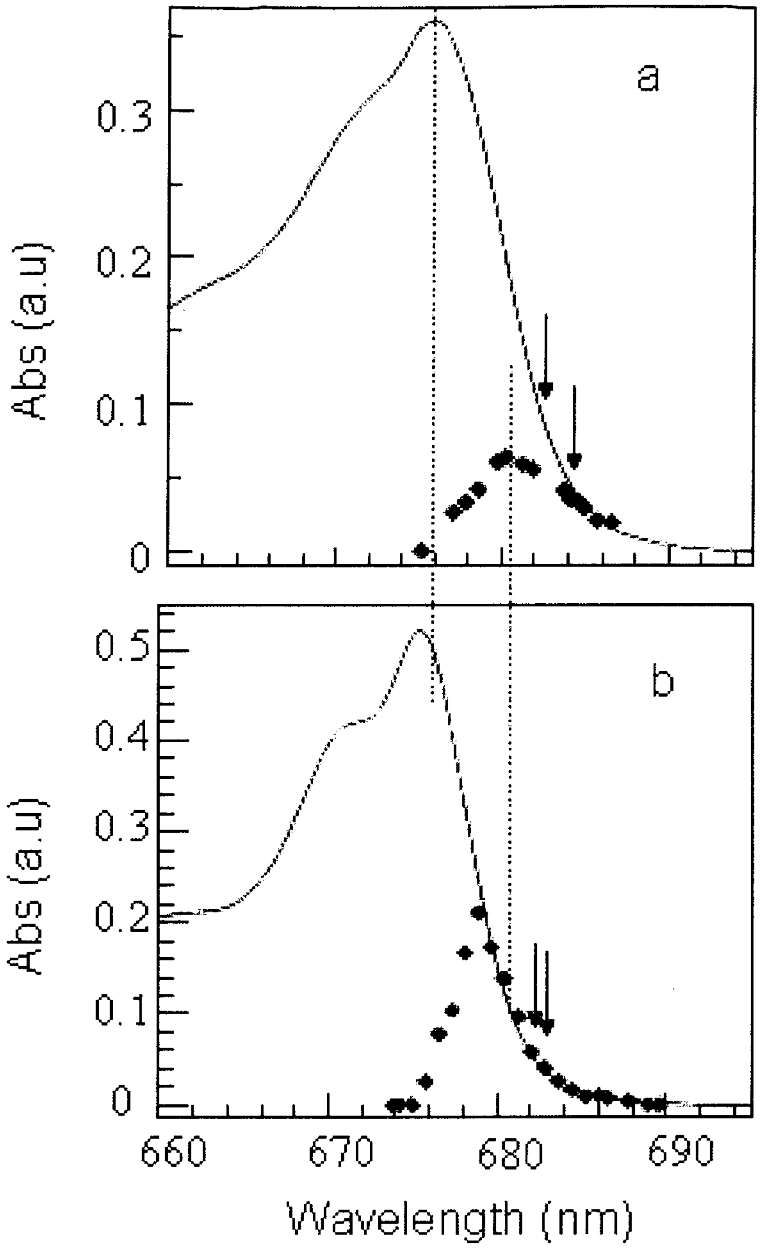

Fig. 5.15. Absorption (red curves) and HB action spectra (diamond curves) of LHCII-monomer (a) and LHCII-trimer (b)

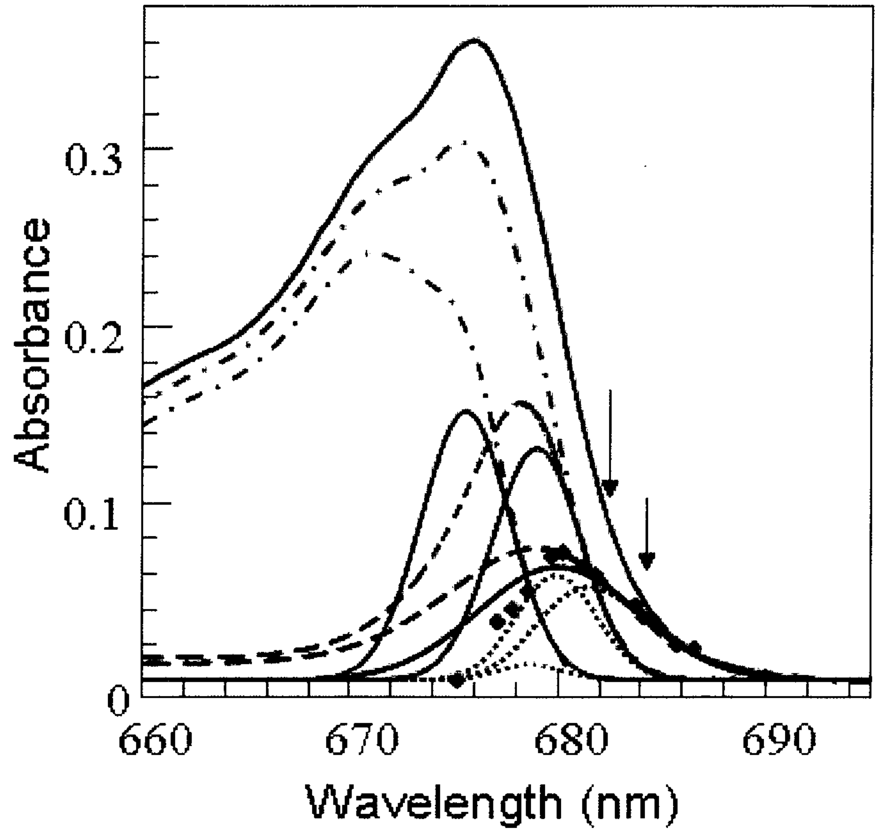

Fig. 5.16 The SDF and the absorption spectrum of the lowest – energy state of LHCII monomer; where the dashed blue curve is the pigment 1 SDF corrected with phonons and localized vibrations contribution; dash-dotted red curve is the difference between the whole absorption spectrum (solid red curve) and the lowest-state absorption (dashed blue curve); black and green solid curves are the second and third-lowest energy SDFs; dashed black curve is the absorption spectrum of pigment 2 dressed with phonon and vibration contributions; black dotted curve is SDF of pigment 2 molecules incapable of downhill EET

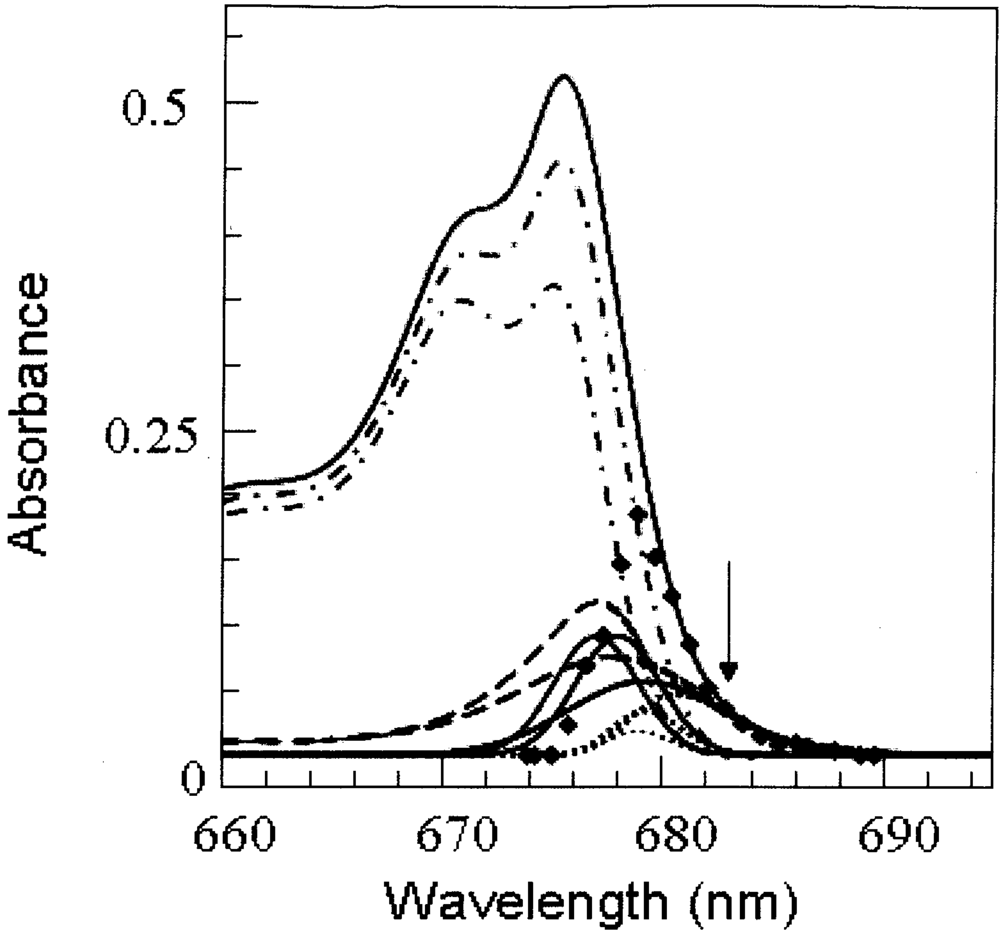

Fig. 5.17 The SDF and the absorption spectrum of the lowest – energy state of LHCII trimer; where the dashed blue curve is the pigment 1 SDF corrected with phonons and localized vibrations contribution; dash-dotted red curve is the difference between the whole absorption spectrum (solid red curve) and the lowest-state absorption (dashed blue curve); black and green solid curves are the second and third-lowest energy SDFs; dashed black curve is the absorption spectrum of pigment 2 dressed with phonon and vibration contributions; black dotted curve is SDF of pigment 2 molecules incapable of downhill EET

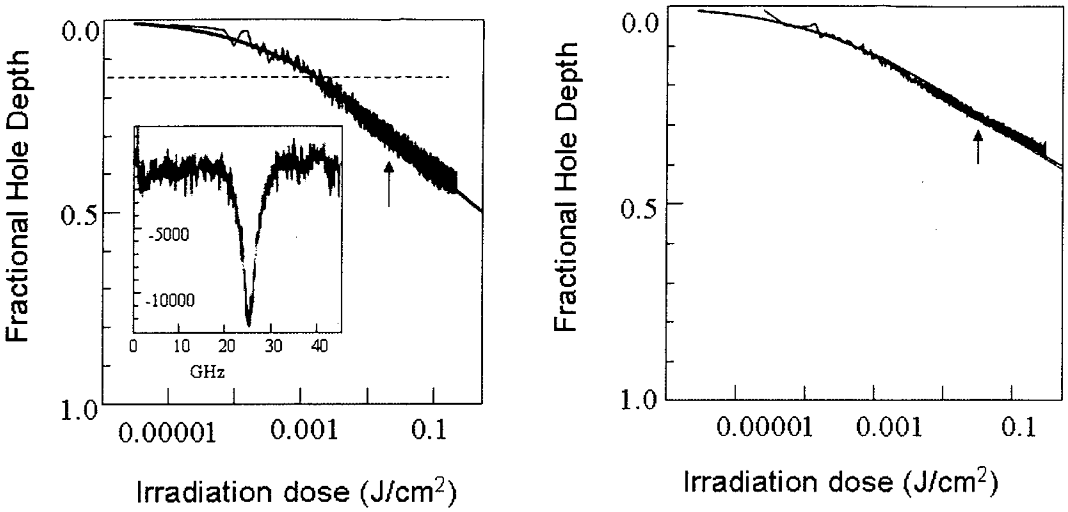

(a) (b)

Fig. 5.18 The experimental HGK curves for LHCII – monomer (a) and trimer (b) and the best fit to HGK for burn wavelength of 684.2 nm and 683.1 nm respectively; the insert shows the spectral hole burned at 684.2 nm

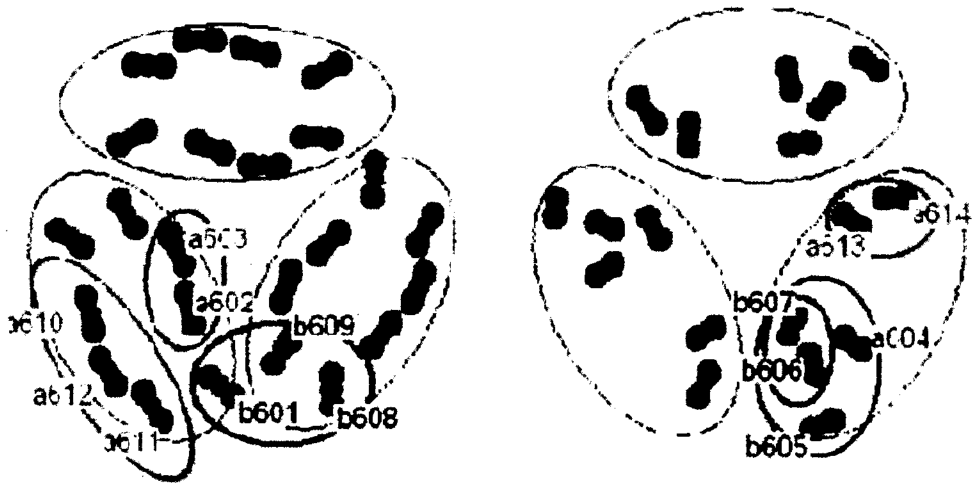

Fig. 5.19 The structural arrangement of chlorophylls in LHCII (after ref. 27)

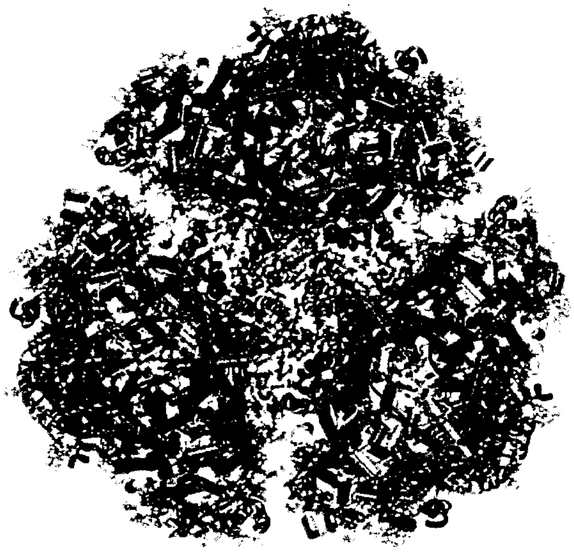

(a)

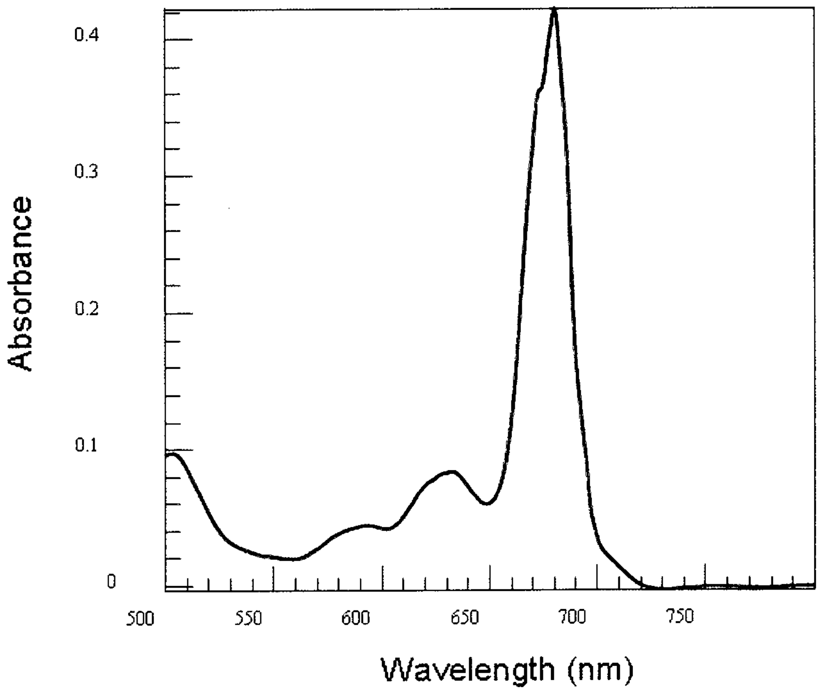

(b)

Fig. A1.1 The structural model of Photosystem I and the absorption spectrum of PS-I wild type (a -from ref. 106, b - from our group data). Green – chlorophyll molecules, blue, pink, purple, orange, etc – protein alpha-helixes.

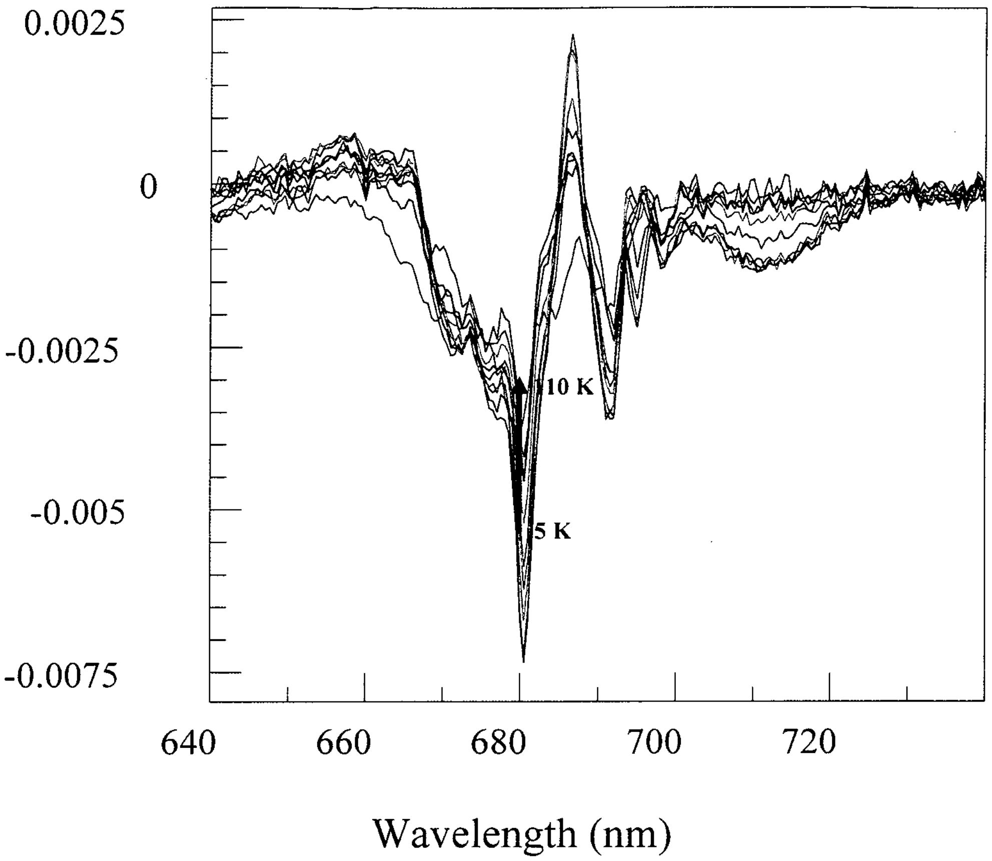

Fig. A1.2 Thermocycled spectral holes burned in to the absorption spectrum of Synechocystis PCC6803 at 660 nm (T=5K, 20K, 31K, 40K, 52K, 61K, 73k, 86K, 99K, 110K). The lowest-temperature spectrum is the deepest hole spectrum. The vertical line indicates the burn wavelength.

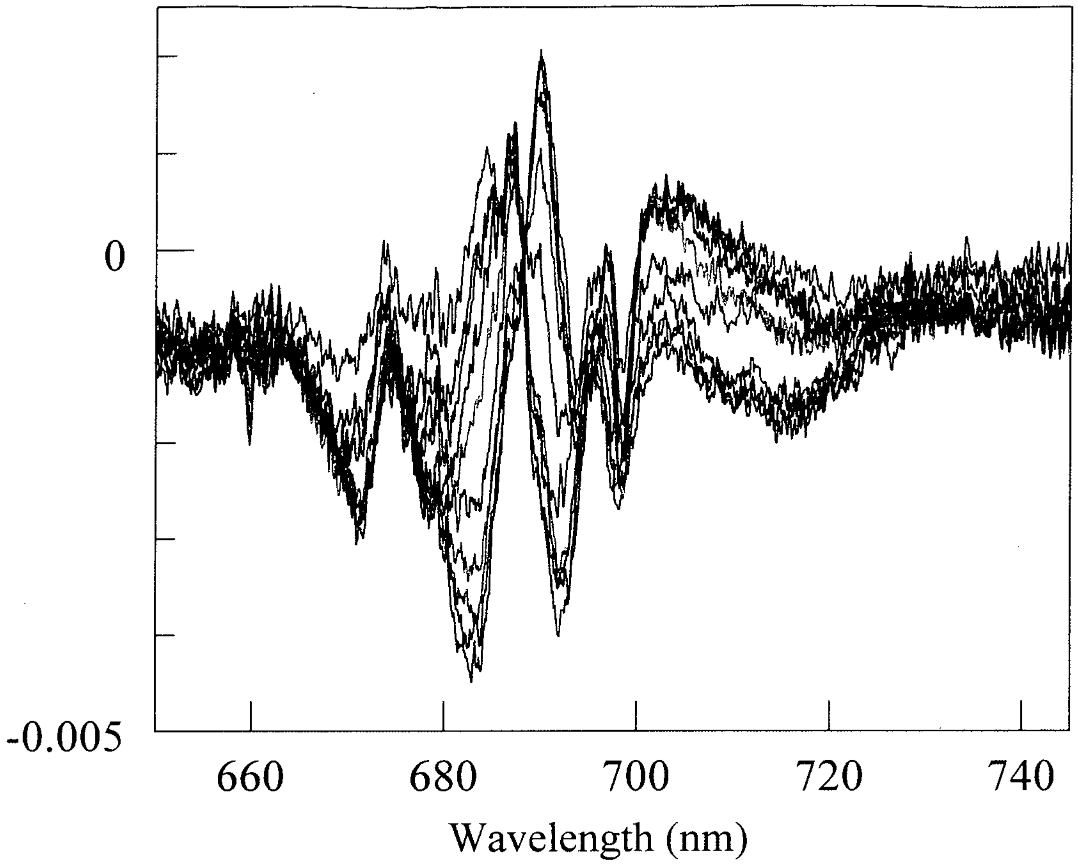

Fig. A1.3 Thermocycled spectral holes burned in the absorption spectrum of *Thermosynechococcus Elongatus* at 659.94 nm (T=5K, 19.5K, 30K, 40K, 50K, 69.4K, 85.1K, 100K, 119K, 146K). The lowest-temperature spectrum is the deepest hole spectrum

List of Acronyms

CP 29 – Chlorophyll – Protein complex

CP 43 – Chlorophyll – Protein complex

Δ-FLN – Delta Fluorescence Line Narrowing

FWHM - Full Width at Half Maximum

HGK – Hole Growth Kinetics

LIHF – Light-Induced Hole Filling

LH 2 – Peripheral light-harvesting antenna

LHC II – Light-harvesting complex II

MLS – Multi-Level System

NADP+ - Nicotinamide Adenine Dinucleotide Phosphate

NPHB - Persistent Non-photochemical Hole Burning

PHB – Photochemical Hole Burning

PSB - Phonon Side Band

PSI - Photosystem I

PSII - Photosystem II

RC – reaction center

SDF – Side Distribution Function

SHB - Spectral Hole Burning

SMS - Single Molecule Spectroscopy

SPCS – Single Photosynthetic Complex Spectroscopy

TLS – Two-Level System

ZPL – Zero – Phonon Line

INTRODUCTION

The importance of photosynthesis as unique physico-chemical phenomenon was pointed out many years ago, but research into its mechanisms and related structures reached the height of attention only during the past 40 years. This interest continues further, owing to the constant development of various experimental approaches and emergence of new high-quality samples. Photosynthesis is a highly interdisciplinary field of research with implications affecting areas from solar energy conversion to biosensors to general properties of protein energy landscapes.

Photosynthesis is the process by which plants, algae and photosynthetic bacteria convert solar energy into a form that can be used to sustain the life process [1-3].

$$6CO_2 + 12H_2O \overset{h\nu}{\rightarrow} C_6H_{12}O_6 + 6O_2$$

There are certain steps of photosynthesis which are followed to arrive at the above equation [1-3]:

- light absorption and energy delivery by antenna systems – photo-physical process;
- primary electron transfer in reaction centers - photochemical process;
- energy stabilization by secondary electron transfer- chemical process;
- synthesis and transport of stable sugar products - biochemical process.

To perform primary steps of photosynthesis, plants, algae and bacteria possess well organized and closely coupled photosynthetic pigment-protein complexes. The structures of various photosynthetic complexes are reviewed in Chapter 2 and Appendix I. The common denominator is that proteins in these complexes hold together a network of pigment molecules, which is optimized for light harvesting, energy transfer and charge separation.

Photosynthetic pigment-protein complexes are complicated systems, and it is difficult to analyze their spectroscopic properties in full detail [5-7]. Traditionally the optical spectra of photosynthetic pigment-protein complexes at low temperatures are analyzed in the same way as that in the case of chromophores in amorphous solid hosts [8] (e.g. glasses and polymers), as they exhibit large inhomogeneous broadening due to static disorder. This is caused by individual pigments, e.g. chlorophylls, bacteriochlorophylls or carotenoids, experiencing slightly different local environments even in the same protein site, which leads to a broad distribution of electronic transition frequencies [5-7]. The background information on optical spectroscopy in general and in the case of amorphous solids in particular will be presented in Chapter 1.

Inhomogeneous broadening hides the information about the energy transfer processes and protein dynamics of photosynthetic complexes, which is contained in the widths and positions of the narrow (at low temperatures) homogeneously-broadened lines, which contain information on energy and charge transfer or pure dephasing (see Chapter 1). This problem can be solved by utilizing methods of high-resolution optical spectroscopy [9, 10]. One of such high-resolution methods is Spectral Hole Burning (SHB). Persistent non-photochemical hole burning (NPHB) is a variety of SHB occurring in structurally disordered hosts such as glasses, polymers, and proteins. It does not involve any photochemical reactions but is a result of rearrangement of pigment's local environment. The latter can be interpreted as tunneling between different host-chromophore configurations [11]. The tunneling is triggered by excitation of the chromophore and occurs while the chromophore is in its excited state [12]. Investigation of single molecules / complexes (Single Molecule Spectroscopy, SMS) is the ultimate method of escaping inhomogeneous broadening. However, SMS is technically much more demanding and, as we will demonstrate, may provide results which are not statistically relevant representatives of the large ensembles of identical proteins. Both SMS and SHB can be employed to explore light-induced spectral diffusion, which is a manifestation of low-temperature protein dynamics. The latter is the key subject of the present thesis. The studies of low-temperature protein dynamics by methods of optical spectroscopy published so far [63, 62] do not address the comparison between the results obtained by different methods for the same proteins. While SHB studies focused on heme protein and horseradish peroxidase [51], SMS was applied almost exclusively to photosynthetic protein complexes, mainly LH2 antenna complexes of purple bacteria (see Chapter 2) [46].

In Chapter 2 we present the structures of various photosynthetic complexes used in this work. In Chapter 3 we discuss the technical details of our SHB experiments and give some overview of SMS experiments by Aartsma's and Köhler groups with which we compare our results. In Chapter 4 we discuss the theoretical models relevant from the viewpoint of studying low-temperature protein dynamics by optical methods.

In Chapter 5 we present the results of our hole burning experiments and discuss them within the framework of available models. For LH2 [38] we demonstrate partial incompatibility of SMS results with our SHB data. In the next sections we discuss the results of similar SHB experiments for several small chlorophyll a -based antenna complexes, which are, generally, in line with the LH2 results.

Conclusions of our work are summarized in Chapter 6.

Appendix I contains very recent data on protein dynamics in still another photosynthetic complex, cyanobacterial Photosystem I.

CHAPTER 1. BASICS OF OPTICAL SPECTRA

1. 1 Relation between various parameters of optical transitions

The optical transitions of atoms and molecules are characterized by such parameters as Einstein coefficients, transition dipole moment, oscillator strength, absorption coefficient, and the line shape function.

There are three coefficients to describe optical transitions of atoms and molecules. The Einstein A_{21} coefficient defines the total rate of spontaneous emission [13, 15]:

$$A_{21} = \frac{64\pi^4 v^3 \mu_{12}{}^2 g_1}{3hc^3 g_2}, \text{ and } \tau_{21} = 1/A_{21} \qquad (1.1)$$

where ν is the frequency of transition; g_i is the degeneracy of level i; τ_{21} is the natural (fluorescence) lifetime; μ_{12} is the transition dipole moment, $\mu_{12} = \int \psi_2^* \mu \psi_1 dV$ and $\mu = \sum_i q_i r_i$ is the electric dipole moment operator; $|\mu_{12}|^2$ is proportional to the transition probability, which gives the selection rules: for a forbidden transition $|\mu|^2 = 0$ and for an allowed transition ($|\mu|^2 \neq 0$).

The Einstein coefficient B_{21} characterizes the transition rate of stimulated (induced) emission while the transition rate of absorption is proportional to the Einstein coefficient B_{12} (as well as to the energy density in the field). One notes that stimulated emission is a coherent process while the spontaneous emission is an incoherent process [13, 15]. In our experiments we are concerned only with absorption and spontaneous emission.

$$B_{12} = B_{21}\text{, and } B_{12} = \frac{8\pi^3}{3ch^2}\mu_{12}^{2} \qquad (1{:}2)$$

The Einstein coefficient of spontaneous emission is related to the Einstein coefficient of absorption/stimulated emission by the following formula [13, 15]:

$$A_{21}=\frac{8\pi h\nu^3}{c}B_{21}$$

The Einstein coefficient for absorption or stimulated emission is related to the absorbance one can find in Beer's law:

$$I = I_0 10^{-OD} = I_0 10^{-c\varepsilon z} \qquad (1{:}3)$$

where OD is optical density, or "absorbance" (see subsequent sections), c is the concentration of the chromophore, and ε is the molar extinction coefficient. The latter is related to absorption cross-section. The absorption cross section is wavelength-dependent and depends on the line-shape function. $\sigma(cm^2) = \frac{8\pi^3 \nu f(\nu)\mu^3}{3ch}$; and the integrated cross section $\int \sigma(\nu)d\nu = h\nu B_{12}$, [13-15].

Since optical transition process is quantum-mechanical in nature, the Heisenberg uncertainty principle applies.

$$\Delta E \Delta t \geq \frac{h}{2\pi} \qquad (1{:}4)$$

This principle states that to determine either the energy or the lifetime of a particular transition one has to restrict the accuracy of the other. Therefore, the spectral lineshape of an optical transition is necessarily broadened by this condition, and it is often referred to as *natural or homogeneous lineshape* of an optical transition and *natural or homogeneous broadening* respectively [13-15].

Broadening of lines arising from finite lifetime of a state gives rise to a Lorentzian line-shape function, $f_L(\nu)$.

$$f_L(\nu) = \frac{\gamma_L / 2\pi}{(\nu - \nu_0)^2 + \gamma_L^2 / 4} \qquad (1:5)$$

where, γ_L is the Lorentzian full width at half maximum (FWHM), which is inversely proportional to the natural lifetime [16, 18].

$$\gamma_{L,nat}(\mathrm{cm}^{-1}) = \frac{1}{2\pi c \tau} \qquad (1:6)$$

where c is speed of light in cm/s and τ in the natural lifetime in seconds.

1.2. Optical properties of host-guest systems

In the host - guest systems the optical properties of guest molecules are strongly influenced by the nature of the host lattice. The host system could be either a crystalline or amorphous solids. “Guest” refers to chromophores which generally are impurities, or dopants [8, 9]. (In the case of photosynthetic complexes, however, chlorophylls are not a result of artificial doping, but are built into protein by Nature.) While the optical properties of certain crystalline materials doped with different molecules have been studied from the early days of the low temperature optical spectroscopy, the study of more complex host–guest systems, like photosynthetic complexes, is still evolving [8, 9].

The absorption line shape of a single molecule embedded in a solid presents two main features, [8, 9]: (a) the zero–phonon line, ZPL (that represents the zero–phonon transition or the purely electronic transition) and (b) the phonon side band, PSB (for electronic transition accompanied by creation or destruction of phonon(s), the quantum of lattice vibration). Homogeneous line width, and Huang-Rhys or Debye Waller factors are parameters that characterize the optical line shape of a chromophore in a solid lattice [8, 9].

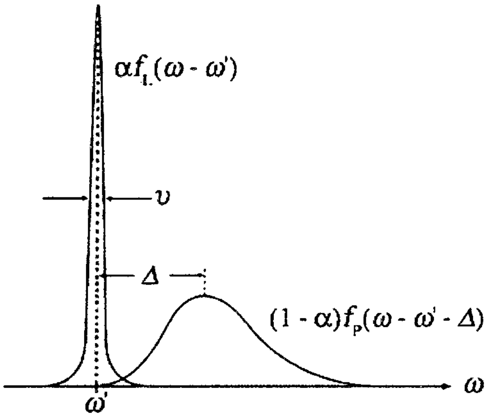

Fig. 1.1 Debye – Waller factor and schematic absorption line shape of guest molecules in perfect lattice (from ref. [9 and 19])

Homogeneous line width is inversely proportional to the dephasing time, τ_2 [8, 9].

$$\gamma = \frac{1}{c\pi\tau_2} \qquad \frac{1}{\tau_2} = \frac{1}{2\tau_1} + \frac{1}{\tau_2^*} \tag{1:7}$$

where τ_1 is excited state lifetime / energetic relaxation time and τ_2^* is pure dephasing time. The latter corresponds to the processes when, for example, scattering of a phonon off the chromophore results in a random shift of the excited state wavefunction phase without molecule actually returning to the ground electronic state (such returning would be described by τ_1). The dephasing time τ_2 represents the lifetime of the excited state coherence [9]. In other words, there are two types of processes that determine the dephasing time τ_2: the decay processes of the excited state population that contributes with the finite lifetime τ_1 and pure phase-destroying processes with τ_2^* [9]. One should note that in the limiting case when temperature approaches the absolute zero (T = 0K) the pure-dephasing time becomes infinitely long (there are no phonons to be scattered) and γ

depends only on τ_1. Also, factor 2 in equation 1.7 occurs because the lifetime of the ground state is infinitely long [9].

The Debye – Waller factor represents the relative intensity in the zero-phonon line and it is determined by the strength of the electron-phonon coupling [8, 9]

$$\alpha = \frac{I_{ZPL}}{I_{Total}} = \frac{I_{ZPL}}{I_{ZPL} + I_{PSB}} = \exp(-S) \qquad (1:8)$$

where I_{ZPL} is the integral intensity of the zero-phonon line and I_{Total} is the total intensity and I_{PSB} is the integral intensity of the phonon sideband. S is the Huang-Rhys factor that is related to the displacement Δ between the minimum energy positions of harmonic vibrational potentials associated with ground and excited electronic states.

$$S = \frac{1}{2}\Delta^2 \qquad \Delta = 2\pi\sqrt{m_r \nu / h}(b_e - b_g) \qquad (1:9)$$

where ν is the vibrational frequency, $(b_e - b_g)$ is the change in generalized coordinate (in the simplest case of a linear diatomic molecule – change of the equilibrium bond length).

Since the Huang-Rhys factor is related to the Franck-Condon factor and further to the square of nuclear wavefunction overlap, it determines the probability of exciting particular vibration during electronic transition. Excitation of these transitions gives rise to vibrational replicas in absorption and fluorescence spectra [13-16].

Both homogeneous line width and Debye-Waller factor vary strongly with temperature. At low temperatures the ZPL width is much narrower and ZPL becomes more prominent than PSB. The relative intensity in the zero-phonon line decreases with increasing temperature, e.g. the zero-phonon becomes virtually indistinguishable from PSB for temperatures above 50 K [8, 9]. The homogeneous line width increases with temperature leading to the thermal broadening of line shape.

Now we turn to the spectra of the ensembles of molecules and to origins of the inhomogeneous broadening. One can consider the case of a perfect host lattice doped with guest molecules in a very low concentration (Fig. 1.2). In this case the guest molecules can be considered isolated from one another and will have identical spectral features due to identical local environment [8, 9]. In other words, the host-guest interaction introduces a certain spectral shift, named "solvent shift". For a perfect host lattice this interaction determines the same shift for all molecules and hence their transition frequencies are identical [8, 9].

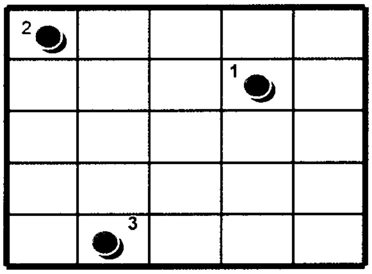

Fig. 1. 2 Identical guest molecules in a perfect lattice (after ref. [8, 9])

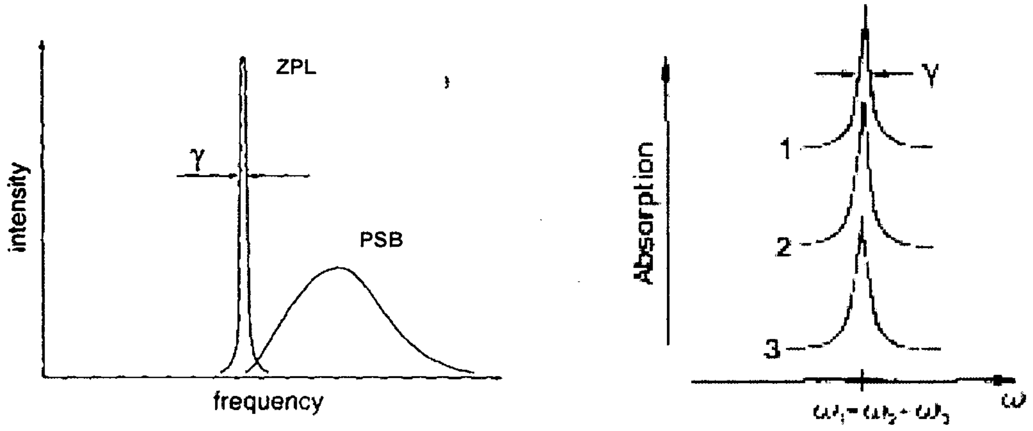

a. b.

Fig. 1. 3 Absorption line shape of guest molecules in perfect lattice
a. absorption line shape of a single guest molecule in a perfect lattice;
b. Homogeneous lines of identical guest molecules in a perfect lattice (from ref. [8, 9])

In contrast to the perfect lattice, the individual guest molecules experience different environments and the respective absorption energies will present dispersion. In consequence the associated band is broad and this broadening due to static disorder is called inhomogeneous broadening [8, 9].

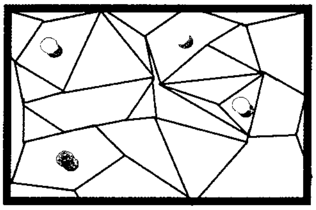

Fig. 1.4 A disordered lattice doped with guest molecules (after ref. [8, 9])

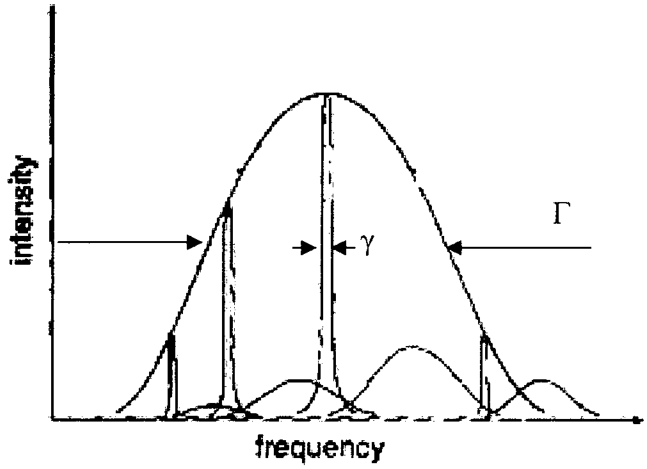

Fig. 1.5 Absorption line shape of guest molecules in disordered lattice
Γ - inhomogeneous lines width; γ - homogeneous lines width (from ref. [8, 9])

As it is shown in Figure 1.5 the inhomogeneous absorption band is the convolution of the single molecule line shape ("single site spectrum") with the site distribution function and the respective inhomogeneous width Γ is very large [8, 9]. The site distribution function (SDF) describes the probability to find a molecule with the purely electronic (0-0) S_0-S_1 transition at a certain frequency, [17]. Since the homogeneous line is hidden under the inhomogeneously broadened absorption band, γ cannot be obtained by conventional spectroscopy, one can use the high resolution spectroscopy methods to solve this issue, [10].

CHAPTER 2 OVERVIEW OF PHOTOSYNTHETIC COMPLEXES STUDIED

In plants and cyanobacteria there are two categories of photosynthetic pigment-protein complexes: Photosystem I (PSI) and Photosystem II (PSII). Both photosystems are transmembrane proteins located in the thylakoid membrane. Both are composed of the reaction center and antenna. In PSII the reaction center can be isolated from the antenna proteins, while in PSI both reaction center and antenna chlorophylls are held by the same protein(s). Despite that difference, there are multiple similarities in the arrangement of pigments in the core antenna of PSI and PSII. The reaction centers of each photosystem absorb light of somewhat different wavelengths: PSI reaction center is believed to absorb at 700 nm (P700) and PSII RC absorbs at 680 nm (P680). Over the course of photosynthesis processes electrons flow from PSII through cytochrome b_6f and further to PSI [1-5]. This flow of electrons along the membrane is coupled to the flow of protons through the membrane. PSII is responsible for water splitting and oxygen production.

In purple bacteria the cytoplasmic membranes contain, in addition to the reaction centers, two types of light-harvesting complexes: the light-harvesting LH1 complex and the peripheral light-harvesting LH2 complex, both complexes having coaxial ring-like structures. The LH1 complex surrounds reaction center (RC) and LH2 transfers the energy via LH1 to the RC [3, 4]. The LH1 complex has maximum absorption at 875 nm while LH2 has two absorption maxima placed slightly to the blue at 800 and 850 nm respectively [3, 4].

Photosynthetic pigment-protein complexes that have been studied by spectroscopic methods are the following:

2.1. LH2 complexes from purple bacteria - *Rps. Acidophila*

LH2 is a pigment–protein complex that serves as a peripheral light-harvesting antenna in bacterial photosynthesis [1 - 4]. The X-ray crystallographic studies show that LH2 of *Rps. Acidophila* contains 27 bacteriochlorophyll *a* molecules arranged in two highly symmetric coaxial rings. One ring has nine well separated BChl *a* molecules, which absorb light at λ = 800 nm (12,500 cm^{-1}; B800) while the other ring consists of 18 closely interacting BChl *a* molecules, which absorb light at λ = 850 nm (11,765 cm^{-1}, B850) [1 - 4]. Some other purple bacteria, like *Rb. –Molischianum*, feature very similar design, but with 16 and 8 bacteriochlorophylls in the B850 and B800 rings, respectively.

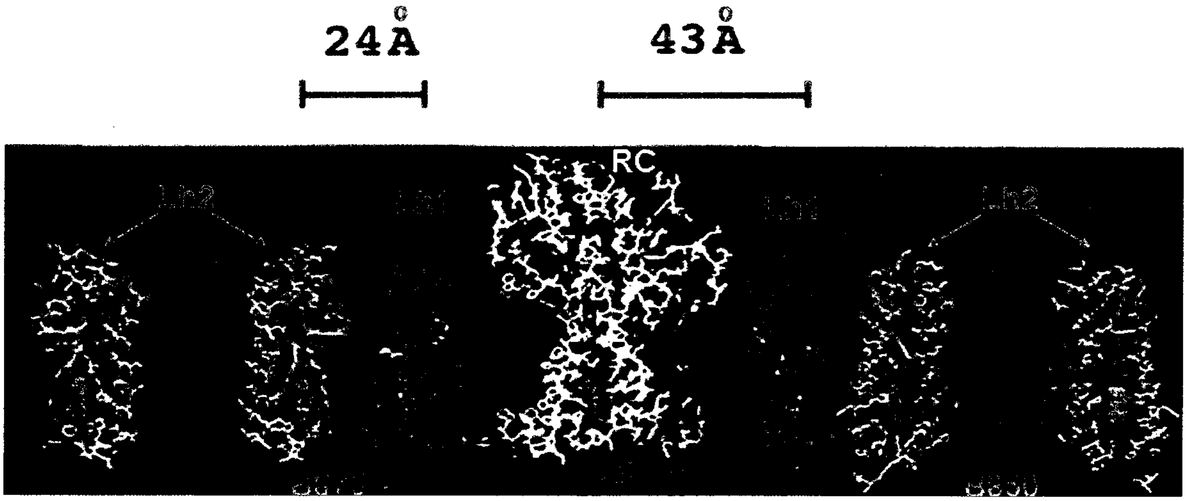

Fig. 2.1 X-ray structure of the photosynthetic unit in purple bacteria, *R. molischianum* (from ref. 4), including the reaction center, LH1 and LH2.

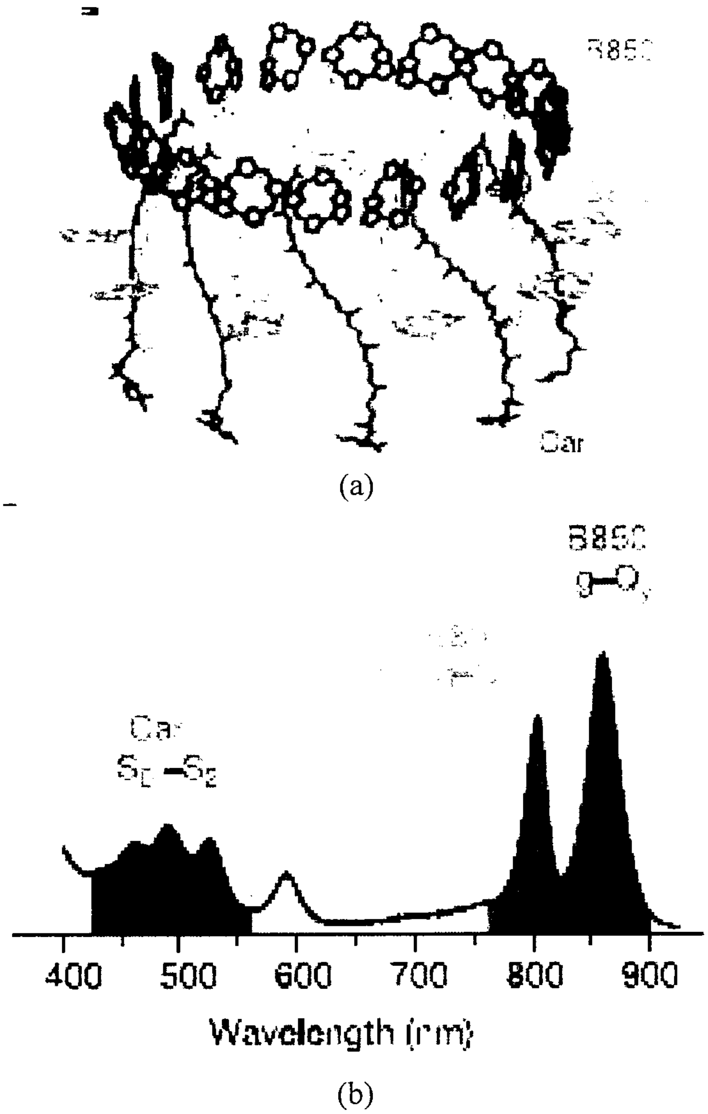

Fig. 2.2 The structure of the peripheral LH2 complex from *Rsp. Acidophila* (a) and the absorption spectrum of lh2 from *Rsp. Acidophila* (b) (from and ref. 17; 18)

2.2 Light-harvesting complexes of Photosystem II

Photosystem II (PSII) is a large supramolecular pigment-protein complex embedded in the thylakoid membranes of green plants, algae, and cyanobacteria [19]. The green plant PSII consists of at least 25 different types of protein subunits, many of which have a light-harvesting or antenna function [19]. There are two groups of light-harvesting complexes in PSII. The first is formed by the core antenna proteins - CP47 and

CP43 and the second group is formed by the peripheral antenna dominated by the light-harvesting complex II - LHCII [19] and also containing smaller antenna complexes genetically close to LHCII: CP24, CP26 and CP29. The second group consists of a collection of related Chl *a*/*b* binding proteins and these proteins do not show sequence homology with the core antenna proteins [19].

The core antenna complex CP43 is a chlorophyll-protein complex that binds 13 chlorophyll *a* molecules located in between the three alpha-helix dimers [19, 20]. As a core antenna the main function of CP43 complex is to funnel the excitation energy from the peripheral PSII antennas complexes (major antenna complexes LHCII and minor antenna complexes named CP29, CP26, and CP24 (or Lhcb4, Lhcb5, and Lhcb 6 respectively) to the reaction center containing P680 [19]. It is also involved in maintaining the structure of the PSII complex [19, 20].

The pigment-binding protein CP29 is a minor PSII light-harvesting antenna, that binds 6 Chls *a* and 2 Chls *b*, and it always exist in monomeric form [21]. This antenna complex is located between the reaction center and the peripherally located major LHCII antenna [22].

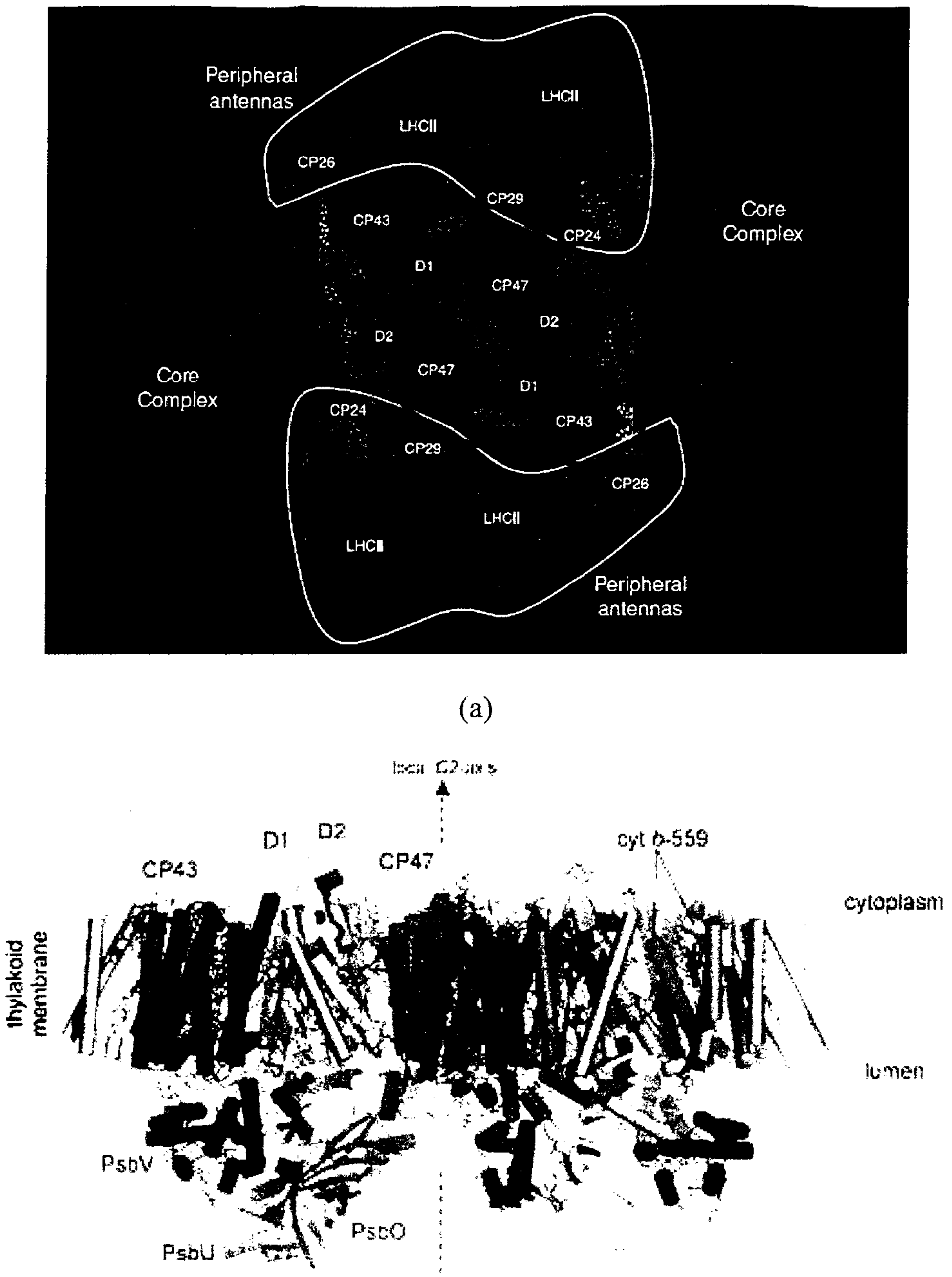

(a)

(b)

Fig. 2.3 Structure of PS II - (a) view from above and (b) side view along the membrane plane of dimeric PSII (from http://www.lbl.gov/Science-Articles/Archive/PBD-CP29.html and http://www.sciencemag.org/feature/data/prizes/ge/2006/loll_figure.gif)

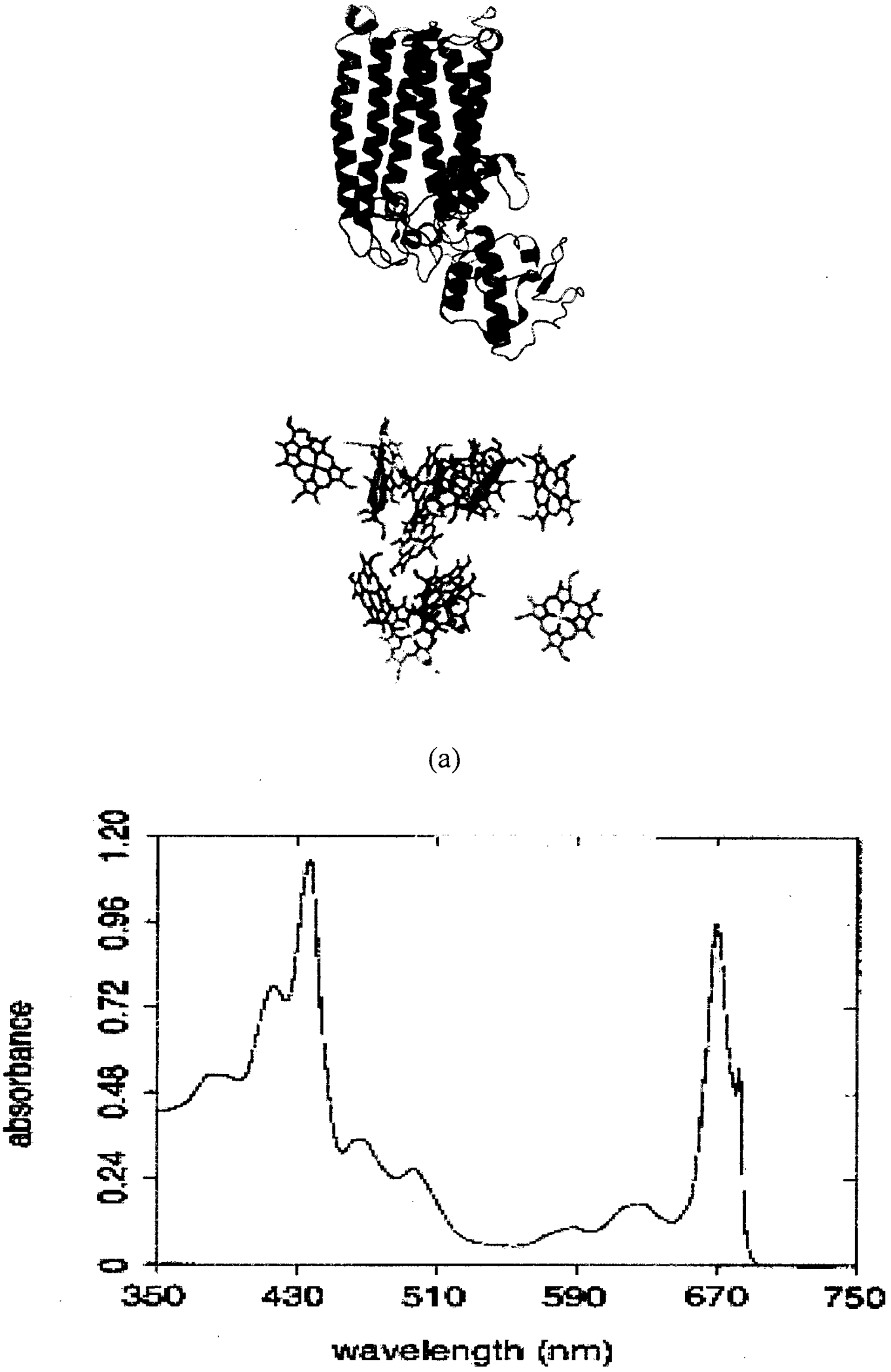

(a)

(b)

Fig. 2.4 Structure (the complete structure and the organization of chlorophylls) and low-temperature absorption spectrum of CP43 (from ref. 19, 20)

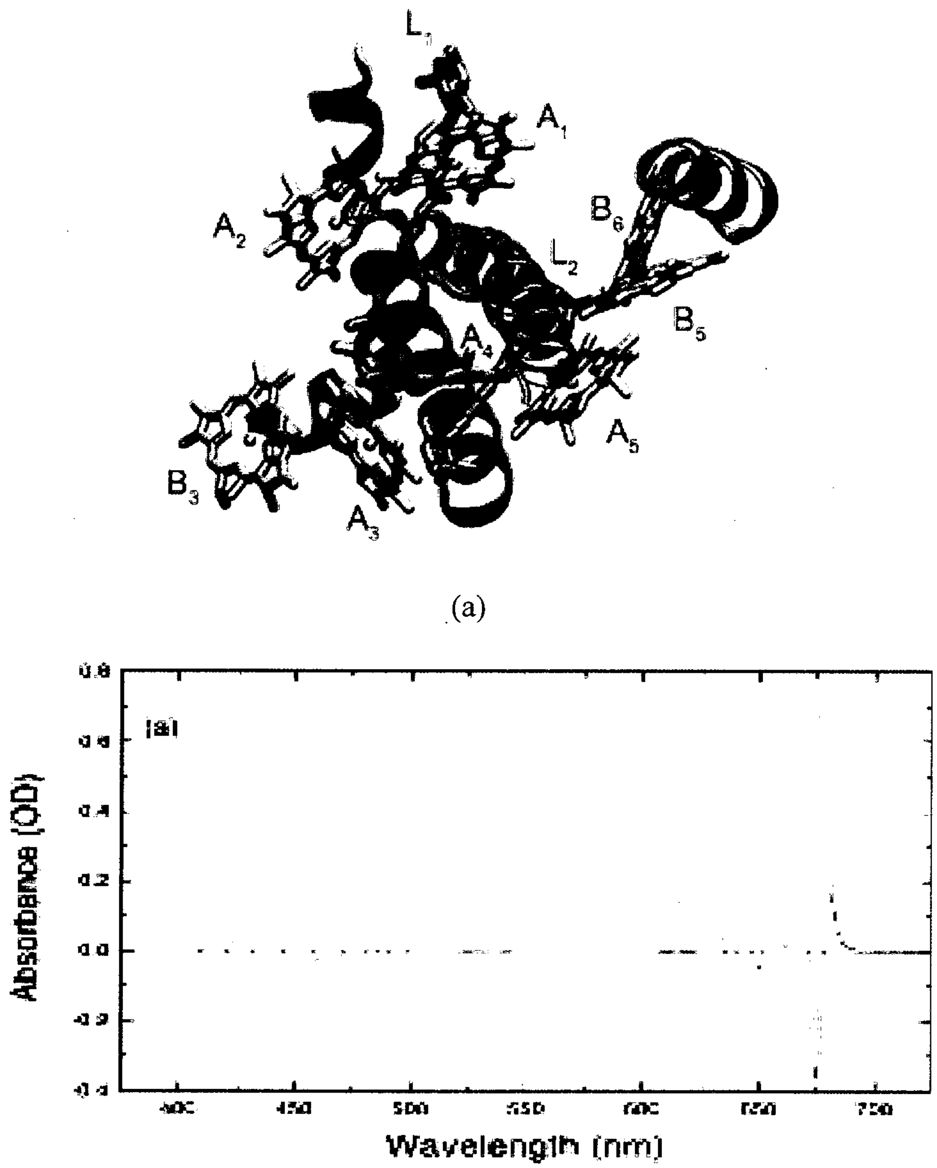

(a)

(b)

Fig. 2.5 Structure and absorption spectrum (with second derivative) of CP29 (from www.lbl.gov/.../Archive/PBD-CP29.html; ref. 21)

Light-harvesting complex II (LHCII) is located peripherally to the reaction center and is the most abundant light-harvesting antenna associated with PSII, binding approximately 65% of its chlorophyll [23, 24]. In its natural form in the thylakoid membrane, the LHCII antenna appears as a trimeric complex and each of its monomers contains 14 chlorophyll molecules arranged in two layers close to the luminal and stromal surfaces of the membrane [23, 24]. According to most recent crystal structure data [25, 26], 8 of these chlorophylls are Chl *a* and 6 are Chl *b*, and the structure sites are unambiguously assigned to either Chl *a* or Chl *b*. Earlier mutagenesis data, however, suggests that some sites can be occupied by either type of chlorophyll. Thus, an isolated trimer contains 21–24 chlorophylls *a*, 15–18 chlorophylls *b*, 2 luteins and 1neoxanthin [23, 24].

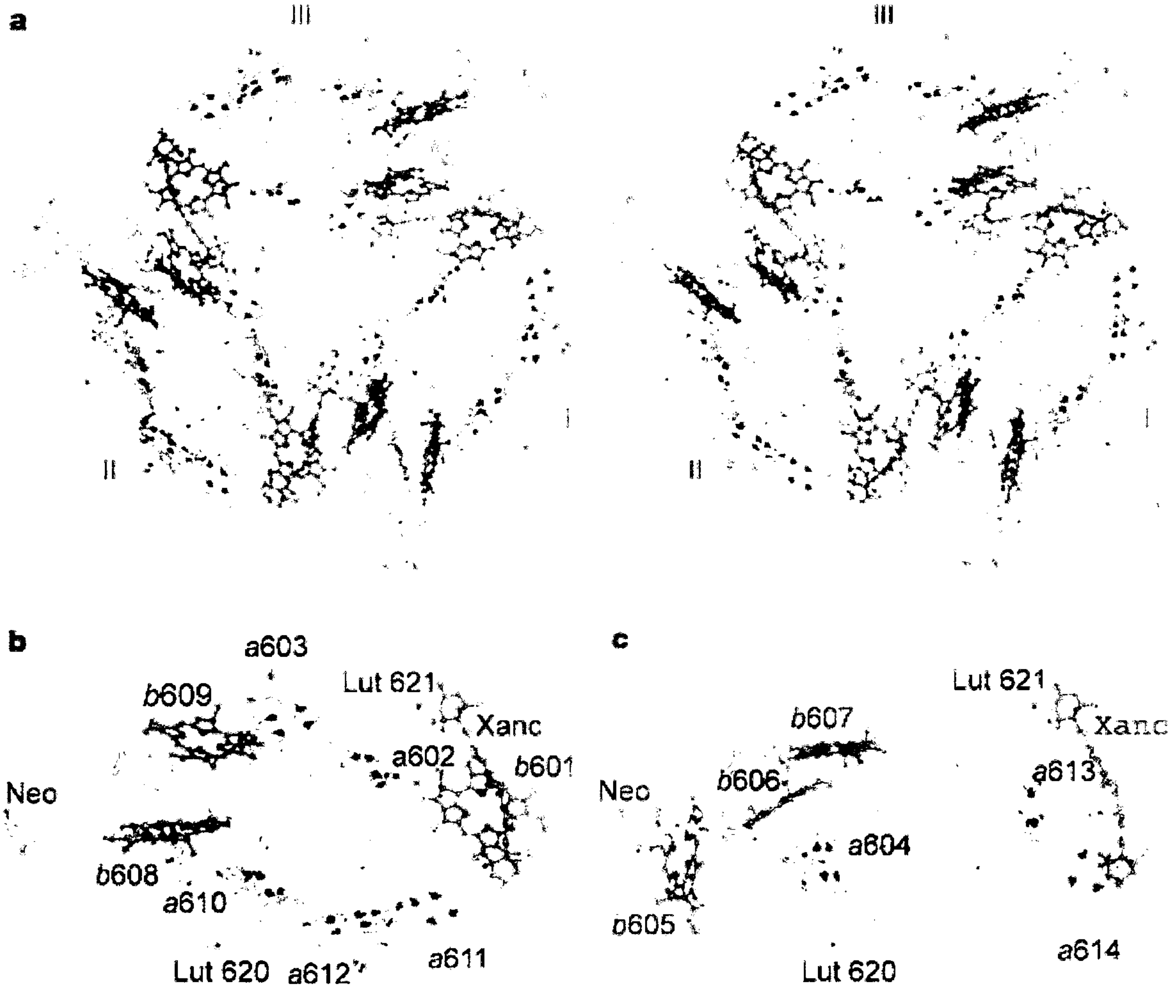

Fig. 2.6 The trimeric and monomeric structure of LHC-II; a – pigments in the LHC-II trimer, view along the membrane normal from the stromal side; b and c, d – pigments in the LHC-II monomer, view at the stromal and lumenal sides, respectively (from ref. 27)

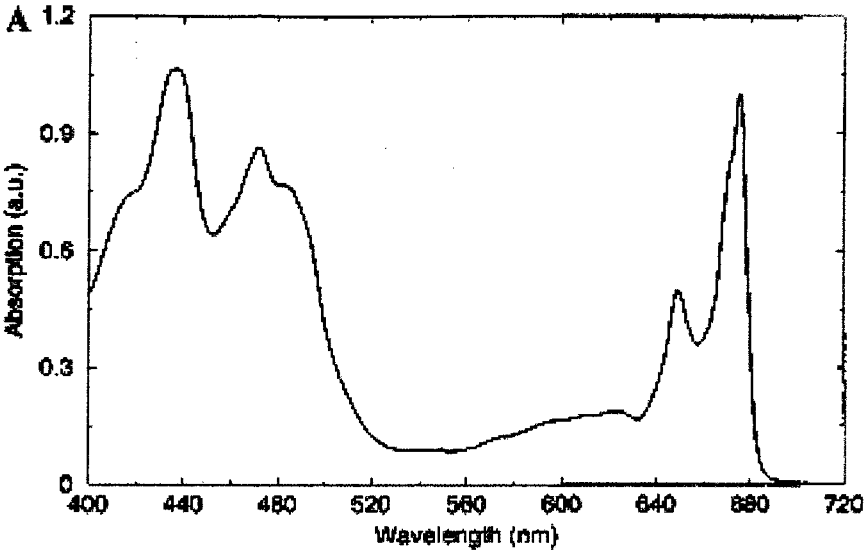

Fig. 2.7 The low-temperature absorption spectra of LHC-II (from ref. 26)

CHAPTER 3. EXPERIMENTAL METHODS

3.1. General features

The absorption spectra presented in the following sections were measured using a Cary 5000 UV-VIS-NIR spectrophotometer. The hole spectra were measured in either absorption or fluorescence excitation modes. The holes were burned and scanned using the tunable Spectra-Physics (Sirah) Matisse Dye Laser or Spectra-Physics 3900 Titanium-Sapphire Laser (in case of LH2), depending on the wavelength. For all experiments both in fluorescence and absorption mode a laser power stabilizer was used (Brockton Electro-Optics Corp).

The setup used to measure absorption spectra and some spectral holes at low resolution (>0.05 nm or ~1 cm^{-1}) is depicted in Figure 3.1

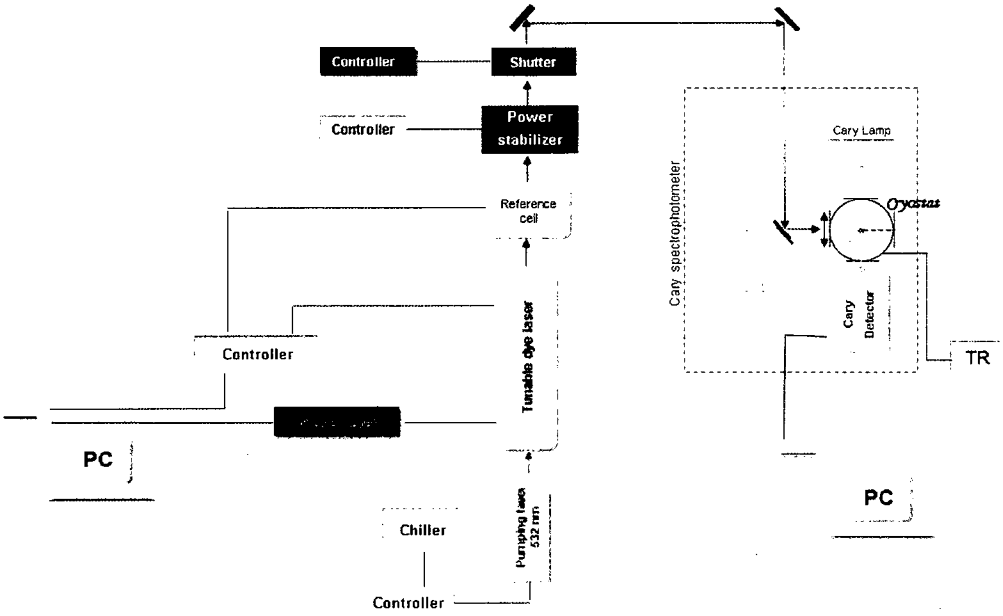

Fig. 3.1 Absorption and low-resolution HB set-up

The burning light of the dye or Ti-sapphire laser was focused on the sample using an open beam optical system.

In high-resolution experiments the holes were usually burned and recorded in fluorescence excitation mode. The laser power density (light intensity) was adjusted accordingly with the type of measurement (burning or reading) using neutral density filters. Thus, the power density for burning varied between several μWcm^{-2} to hundreds of $mW\ cm^{-2}$, while for holes reading, the laser power density was about tens of $nWcm^{-2}$.

Fluorescence signal was attenuated by a long pass filter AELP730 in case of chl a and AELP 850 in case of bchl a (Omega) and conventional long-pass and neutral density filters. The attenuated emitted light was focused on the sensitive area of H7421-50 photon counter module (Hamamatsu) and recorded/converted by NI counter board. The H7421-50 PMT uses a photomultiplier tube having a semiconductor photocathode with a high quantum efficiency that allows measurements over a wide spectral range, $\lambda = 380 - 890$ nm, [28]. To deliver a higher S/N ratio the H7421 PMT is equipped with a Peltier element (thermoelectric cooling element) that reduces thermal noise and a thermistor that measures the temperature [28]. In order to ensure that slight movements of the sample inside of the cryostat due to thermal expansion and contraction do not affect the alignment, the laser beam was expanded to 1 cm in diameter. Figure 3.2 depicts the typical setup in the case of fluorescence excitation experiment.

During spectroscopy experiments, to maintain the samples at low temperature, an optical Liquid Helium cryostat (a gas flow / bath cryostat A240B produced by Ukrainian Academy of Science) was used. This type of cryostat enables cooling of the sample chamber in the range of (300 – 1.5) K, [29]. To achieve the optimum conditions inside the cryostat, vacuum pumps and a pressure stabilizer were used in the cryogenic setup. During experiments, the sample chamber temperature is uniformly controlled by an external temperature regulator (TR). Thus, the optical cryostat A240B allowed enough samples cooling for our goals in experiments at liquid helium temperature and was able to keep the temperature almost constant even in the cases of high burning powers (P_b > 300 mW) and long burning times (t_b > 30 min), [29].

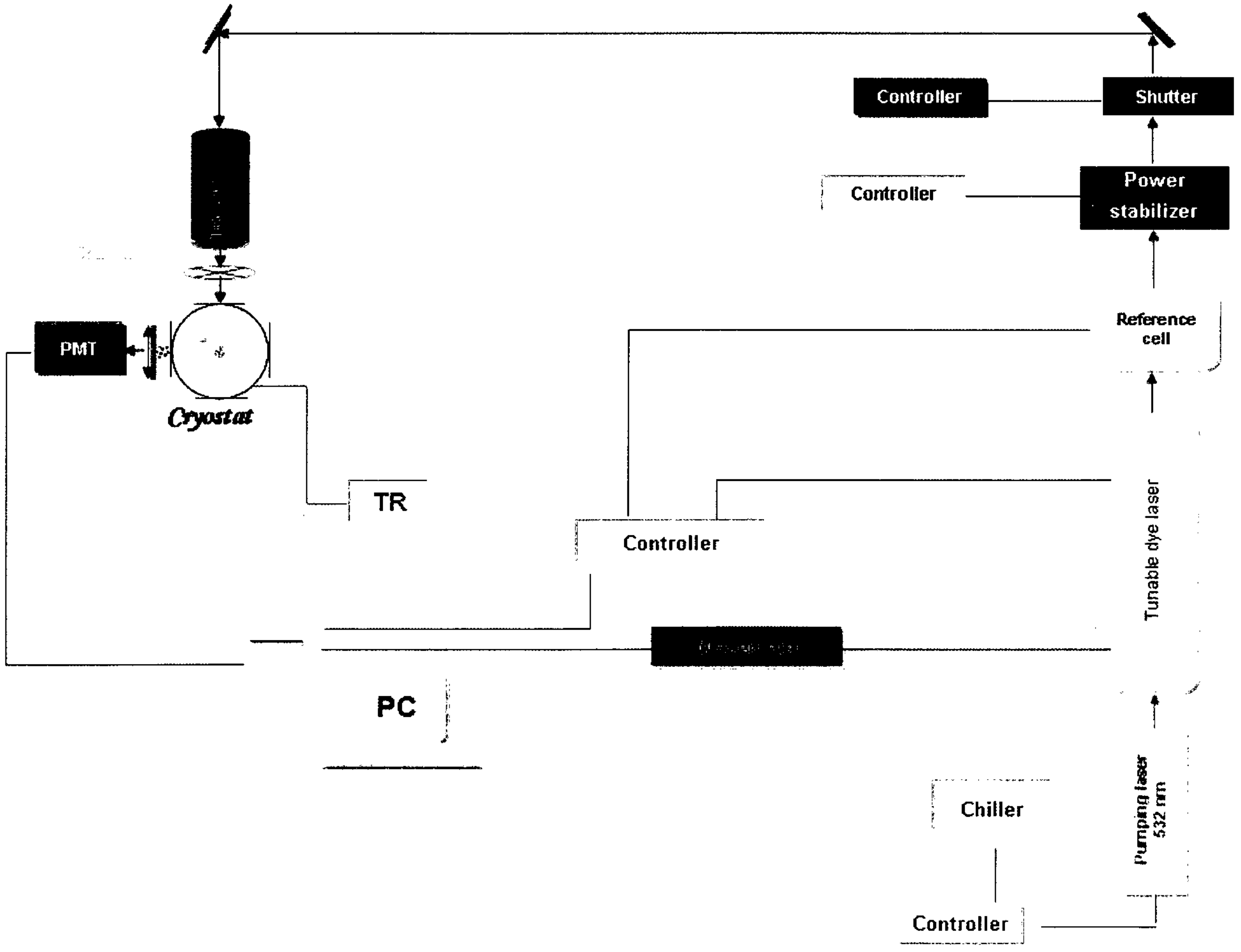

Fig. 3.2 Fluorescence excitation mode set-up

To erase the holes the sample has been heated in the dark to ~ 150K and the absorption spectra have been measured once again to verify if its spectral features had been restored. Heating the sample to temperatures lower than 150 K results in partial filling of the holes (see Appendix I). Analyzing this effect one can determine the distribution of the barriers on a protein energy landscape in the ground state. In thermocycling experiments (see Appendix I) the holes were burnt at low temperature (5 K) as described above and then the sample was subjected to temperature cycling: heating up to a certain temperature and cooling down to 5K. The absorption spectra have been measured at low temperature after each cycle. The hole-burned spectra and the thermocycled hole-burned spectra are post-burn absorption spectra minus pre-burn absorption spectra. The holes growth kinetics curves were measured by monitoring the signal at burn frequency during burning as a function of time. Burn parameters (times and intensities) are given in the text and figure captions of subsequent section.

3.2 Laser system details

For spectral hole burning experiments on complexes containing Chl *a* the laser system based on a high resolution Spectra Physics Matisse DS dye laser (produced by Sirah Gmbh, Germany) was used. The emitted laser radiation is horizontally polarized and depending on the dye and optics set the output wavelength tuning range extends from 550 nm to 660nm or from 640 nm to 760 nm. For all reported results, DCM dye (DCM in EG 60% / EPH 40% mixture) was used together with its specific mirror set (MOS5). Thus, the tuning rage expands from 645 nm to 695 nm, having the maximal power at 660 nm [30]. The laser bandwidth is down to 250 KHz and the typical beam diameter is between 1.2 and 1.4 mm. Matisse DS-dye ring laser operates in TEM_{00} spatial mode. It is tuned using a precise long-travel piezo to allow single-frequency scanning over 45 GHz while maintaining stable power output without mode hopping [30].

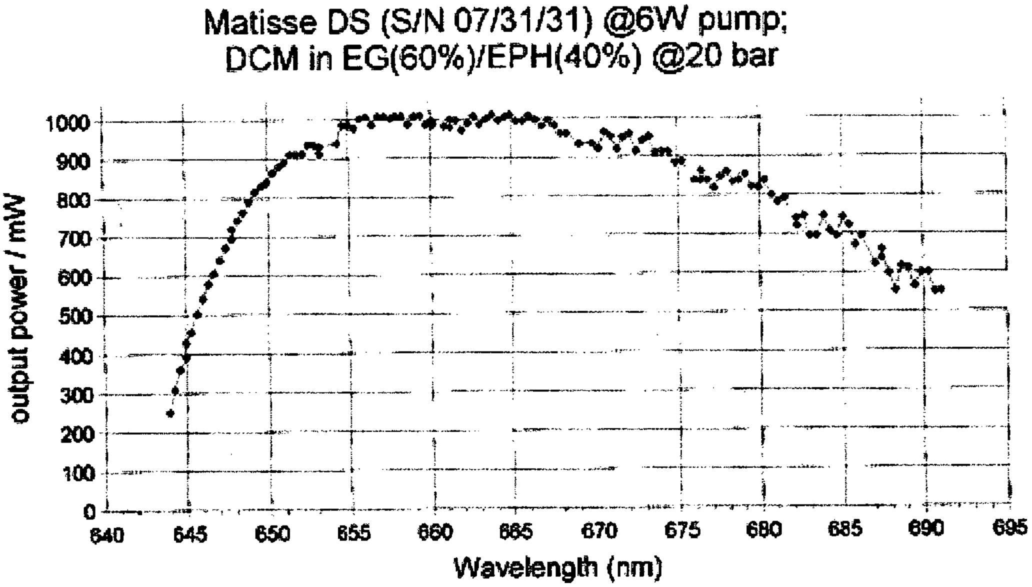

Fig. 3.3 DCM-dye calibration curve (from ref. [30])

3.3 Spectral Hole Burning Simulator

Computer modeling of various spectra was employed to compare the results of experiments with theoretical predictions. Spectral Hole Burning Simulator (developed by V. Zazubovich and T. R. Connolly, using some earlier algorithms by Hayes, Lyle and Reinot) was used. It is based on the theories presented in Chapter 4 below. With the current version of this ever-evolving program one can calculate the absorption spectra, the Single Site Spectra, hole spectra, Δ–FLN spectra, Hole growth kinetics curves and hole width dependence on irradiation (burn) dose. In this respect a set of parameters describing the Site Distribution Function (width and peak), phonon and vibration modes (Huang-Rhys factor; widths and peak frequency of Gaussian and Lorentzian contributions to PSB) of the pigment-protein complex have to be chosen from literature or measured. The parameters of the experiment, e.g. burn frequency and time, diameter and power of the laser beam and optical density of neutral density filters are required for spectra calculation. The simulator includes also various distributions (distribution of tunneling parameter λ; line width distribution, and oscillator strength distribution) as well as NPHB anti-hole if additional effects must be considered. It is also possible to simulate the hole burning into the overlapping absorption bands of two pigments, the situation occurring in most of the photosynthetic complexes at least at some wavelengths.

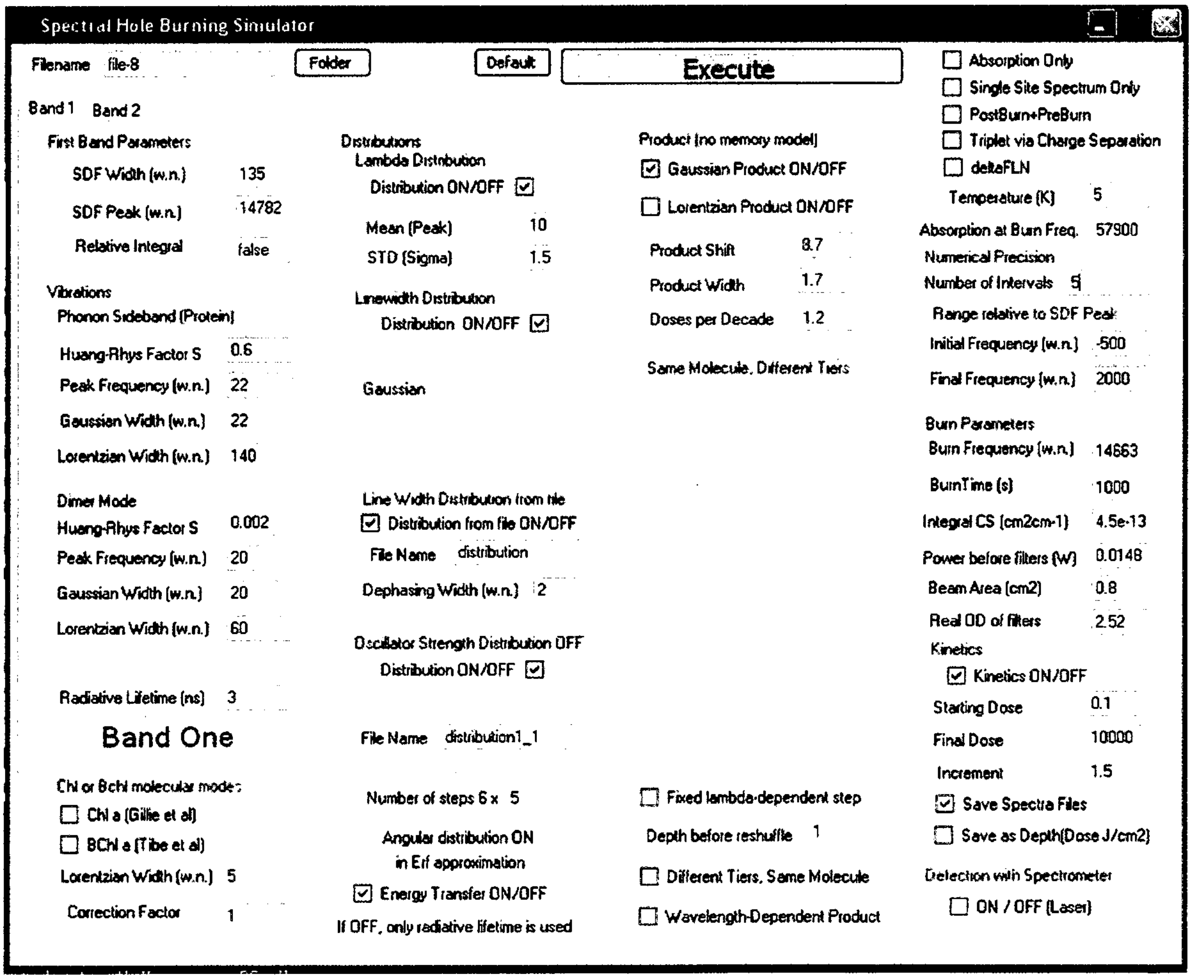

Filename file-8

First Band Parameters
SDF Width (w.n.) 135
SDF Peak (w.n.) 14782
Relative Integral false

Vibrations
Phonon Sideband (Protein)
Huang-Rhys Factor S 0.6
Peak Frequency (w.n.) 22
Gaussian Width (w.n.) 22
Lorentzian Width (w.n.) 140

Dimer Mode
Huang-Rhys Factor S 0.002
Peak Frequency (w.n.) 20
Gaussian Width (w.n.) 20
Lorentzian Width (w.n.) 60

Radiative Lifetime (ns) 3

Band One

Chl or Bchl molecular mode:
☐ Chl a (Gillie et al)
☐ BChl a (Tibe et al)
Lorentzian Width (w.n.) 5
Correction Factor 1

Distributions
Lambda Distribution
Distribution ON/OFF ☑
Mean (Peak) 10
STD (Sigma) 1.5

Linewidth Distribution
Distribution ON/OFF ☑

Gaussian

Line Width Distribution from file
☑ Distribution from file ON/OFF
File Name distribution
Dephasing Width (w.n.) 2

Oscilator Strength Distribution OFF
Distribution ON/OFF ☑

File Name distribution1_1

Number of steps 6 x 5

Angular distribution ON
in Erf approximation
☑ Energy Transfer ON/OFF
If OFF, only radiative lifetime is used

Product (no memory model)
☑ Gaussian Product ON/OFF
☐ Lorentzian Product ON/OFF
Product Shift 8.7
Product Width 1.7
Doses per Decade 1.2

Same Molecule, Different Tiers

☐ Fixed lambda-dependent step
Depth before reshuffle 1
☐ Different Tiers, Same Molecule
☐ Wavelength-Dependent Product

☐ Absorption Only
☐ Single Site Spectrum Only
☐ PostBurn+PreBurn
☐ Triplet via Charge Separation
☐ deltaFLN
Temperature (K) 5
Absorption at Burn Freq. 57900
Numerical Precision
Number of Intervals 5
Range relative to SDF Peak
Initial Frequency (w.n.) -500
Final Frequency (w.n.) 2000

Burn Parameters
Burn Frequency (w.n.) 14663
BurnTime (s) 1000
Integral CS (cm2cm-1) 4.5e-13
Power before filters (W) 0.0148
Beam Area (cm2) 0.8
Real OD of filters 2.52
Kinetics
☑ Kinetics ON/OFF
Starting Dose 0.1
Final Dose 10000
Increment 1.5
☑ Save Spectra Files
☐ Save as Depth(Dose J/cm2)
Detection with Spectrometer
☐ ON / OFF (Laser)

Fig. 3.4 Interface of Spectral Hole Burning Simulator

3.4. Typical setup of Single Molecule Spectroscopy Experiments

As in this research a comparative study of SHB and SMS results by Aartsma's and Köhler's groups [45-50, 61-63] was performed, we briefly discuss the setup of their SMS experiments. To perform single molecule spectroscopy two different experimental arrangements have been used. First, fluorescence microscopy has been performed using the wide-field arrangement while fluorescence-excitation measurements have been performed using the confocal set-up (a home-built microscope that can be operated either in wide field or confocal mode has been used). A CW tunable titanium–sapphire (Ti:Sapphire) laser (pumped by a frequency-doubled continuous-wave neodyniumyttrium-vanadate Nd:YVO4 laser) has been used to illuminate the samples in both types of measurements [46]. In order to scan the wavelength range of the laser a motorized micrometer screw has been used to rotate the intra-cavity birefrigent filter. The wavelength has been measured with a wavemeter.

In case of fluorescence microscopy experiments the excitation light is focused on the sample by means of a simple planoconvex lens and the emitted light is first collected by the single aspheric lens of the objective (placed inside the cryostat) and then it is focused on the CCD camera after passing suitable band-pass filters that cut the residual laser light.

In the confocal mode the excitation light is focused onto the sample after it passed through a sophisticated focusing optical system which main parts are the excitation pinhole, the scanning mirror, the telecentric lenses and then the objective lens inside the cryostat [46]. This focusing system aimed to ensure a very small diffraction-limited excitation volume ($< 1\mu m^3$). Particular volumes (particular complexes) were selected by tilting the direction of the excitation beam with a scan mirror) and by a very precise alignment of sample with the confocal aperture. The emitted light is collected back by the same optical system and focused onto an APD (single-photoncounting avalanche photodiode) module [46].

In these experiments fluorescence excitation spectra have been measured in rapid succession by scanning the laser repetitively through the spectral range of interest and recorded as different traces separately. The aim was to diminish the light-induced fluctuations of the fluorescence intensity on a time scale of seconds and extract information about the spectral dynamics.

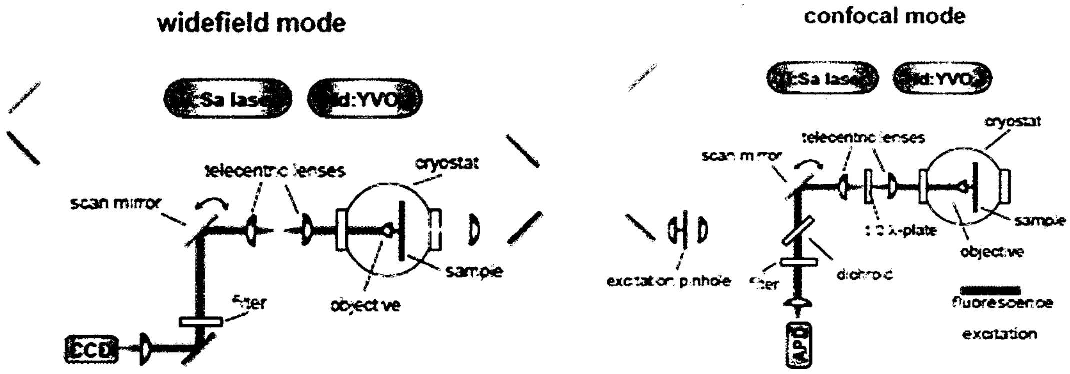

a) b)

Fig. 3.5 Single-molecule spectroscopy; (a) diagram of the wide-field arrangement of the microscope; (b) diagram of the confocal arrangement of the microscope (from ref. 46)

CHAPTER 4 SPECTRAL HOLE BURNING (AND OTHER HIGH-RESOLUTION OPTICAL SPECTROSCOPY TECHNIQUES) IN CASE OF PROTEIN HOST.

4.1. General features of the mechanism of hole burning and hole-burned spectra

Spectral hole burning is one way to uncover a narrow, homogenous line from an inhomogeneously broadened spectral band at low temperatures. The hole is burnt by means of selective photoreactions in a solid solution [9, 10, 31-33]. Irradiation of a sample with a narrow-band laser (ω_B being burn frequency) results in excitation of molecules absorbing at the laser frequency. Molecules absorbing at the burning frequency (or their local environment) may be able to undergo photo-transformation, and, consequently, their absorption spectrum will be shifted to higher or lower frequencies, leaving a narrow hole in the inhomogeneous spectrum at ω_B [15, 9, 10, 31, 32]. The shifted molecules' absorption after the shift is referred to as "photoproduct" or "anti-hole". It should be mentioned that, the photoproduct band or "anti-hole" is usually much broader than the resonant hole [10]. Depending on the actual cause of burning (chemical reaction versus structural change of local environment) one can distinguish photochemical and non-photochemical hole burning. Non-photochemical hole-burning (NPHB), the process actually occurring in photosynthetic complexes, was first observed by Personov and co-workers in glasses [10, 12, 32-35]. If the photoproduct is stable at low temperature, the hole will be persistent while if the photoproduct is in a metastable state a transient hole is created [10]. The spectral hole can be read in absorption, fluorescence excitation or fluorescence mode (Δ-FLN), using very low laser scanning powers [10, 31, 32]. The fluorescence excitation method is more convenient in the case of samples of low optical density [10].

4.2 Hole profile

The hole-burning spectrum is obtained from the difference between the absorption spectrum before and after burning and it shows the structure of the absorption spectrum of burnt molecules [32]. It is obvious that in the first approximation the hole spectrum represents a negative replica of the zero phonon line and it is named Zero Phonon Hole (ZPH), Figure 4.1. The width of the ZPH, Γ_{ZPH} is twice the homogeneous line width [9, 10, 31, 32], $\Gamma_{ZPH} = 2\gamma$. The hole width (Γ_{ZPH}) also yields the lifetime of the excited electronic state (or optical dephasing time, τ_2) and thus provides information about relaxation processes of the excited state.

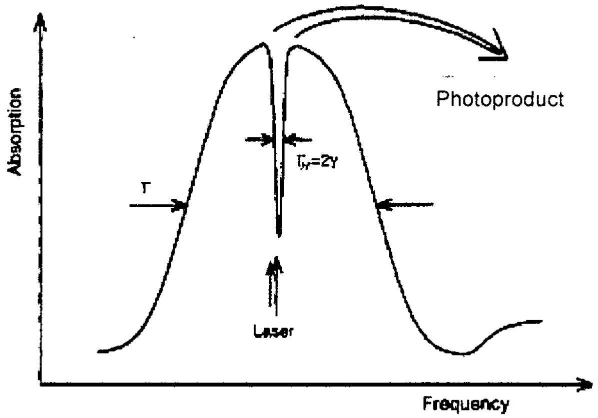

Fig. 4.1 Zero phonon hole (after ref [9])

The hole burnt spectra exhibits contributions not only at the burning frequency but at all vibronic transition frequencies of burnt molecules, as well [32]. The most obvious contribution of this class is so called real phonon sideband (real-PSB), which is the phonon sideband of the ZPH. Additionally, molecules can be burnt not only resonantly via ZPL but also non-resonantly via their PSB. The latter contribution to the hole spectrum is called pseudo-PSB. Thus, the zero-phonon hole is accompanied by additional features located on both sides of ZPH but mainly on its long wavelength side [32]. The low-frequency phonon sidebands contain information about "solvent" vibrations that are coupled to the electronic excitation [15]. Higher-frequency vibronic replicas contain information on localized intra-molecular vibrations of the chromophore.

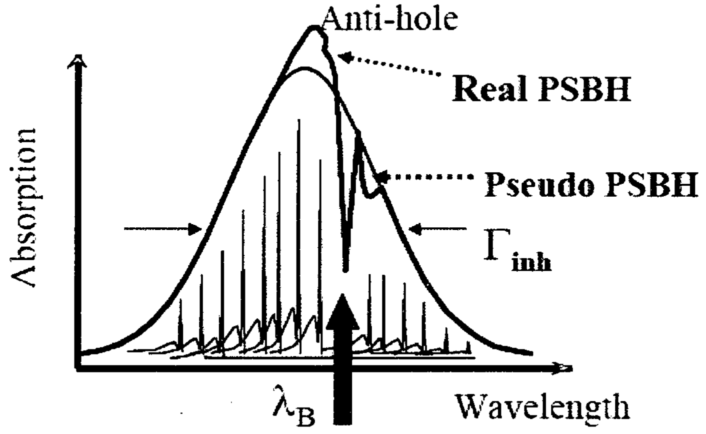

Fig. 4.2 Non-photochemical hole profiles burnt non-resonantly (from ref. [16])

It should be mentioned that the homogeneous ZPL width in glassy matrices, polymers and proteins shows, at very low temperatures, T<5 K, an unusual temperature dependence [10, 21] $\Gamma(T) \approx T^{1.3 \div 1.4}$. This unconventional temperature dependence is explained via interaction of the guest molecules with the two-level systems, TLS (the chromophore is electrostatically coupled the TLS) of the amorphous host [10, 32, 33].

4.3. Two-level systems

The TLS model was introduced many years ago to explain the anomalous thermal and acoustic low temperature properties (specific heat, thermal conductivity, saturation effects in ultrasonic absorption) of amorphous solids and soon thereafter it was successfully used to explain the NPHB spectra [32-34]. Essentially, it is tunneling in TLS that is responsible for non-photochemical spectral hole burning at low temperatures in structurally disordered hosts such as glasses and polymers [12, 32-36]. The tunneling is triggered by excitation of the chromophore and occurs while the chromophore is in its excited state [12, 35].

TLS can be viewed as an asymmetric double well potential with each well representing a distinct structural configuration of the glass [12, 33-35]. The NPHB mechanism presented in Ref. 12 is based on the so-called standard tunneling model. There, the TLS are divided into two classes: the TLS associated with the glassy host named intrinsic TLS (TLS_{int}) and the TLS associated with the guest dye molecule and its inner shell of solvent molecules named extrinsic TLS (TLS_{ext}) [12, 35]. The TLS tunneling mechanism works as follows: first, the laser irradiation leads to the tunneling of TLS_{int} in the outer shell. The TLS_{int} being intimately connected with the excess free volume of glasses its tunneling leads to the diffusion of this volume to the inner shell opening the way for phonon-assisted tunneling of the $TLS_{ext.}$ In the standard tunneling model, TLS-TLS coupling or connectivity is neglected [12].

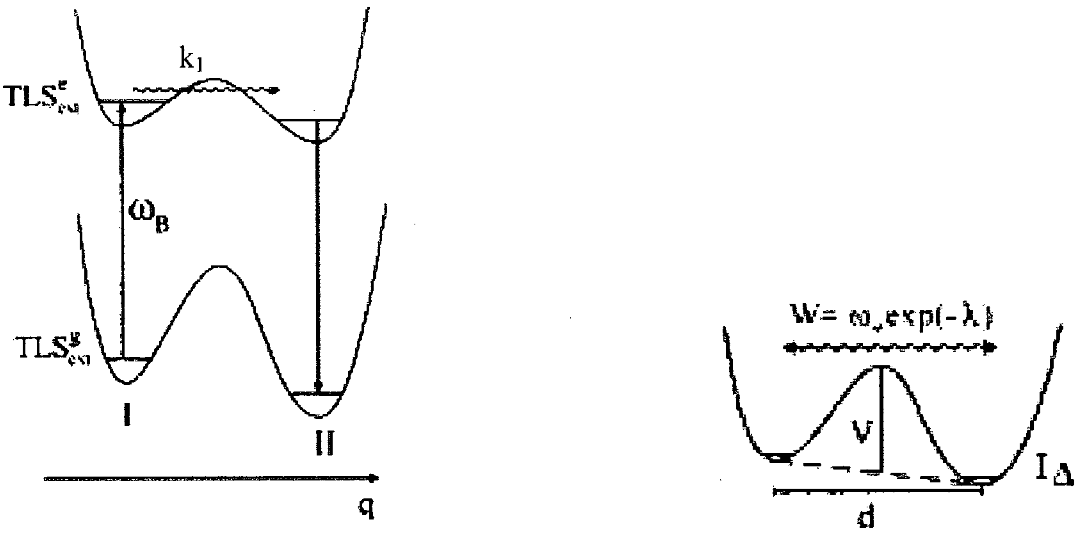

Fig. 4.3 (a) Two-level (referred to as I and II) system model (where indices "e" and "g" indicate the chromophore in its excited and ground state, ω_B is the burn frequency of the laser, and k_I is the tunneling rate, I/II denote the preburn/postburn chromophore host configurations);
(b) The TLS parameters (where *W* is the tunneling frequency), (from ref [12])

The tunneling frequency and tunneling parameter are given by, [12], $W = \omega_B \exp(-\lambda)$ and $\lambda = d(2mV)^{1/2}$, respectively. Here *m* is the effective mass of the tunneling entity, *d* is the displacement between the two potential energy minima and *V* is the barrier height. Because of structural heterogeneity, there is a distribution of TLS_{ext} (i.e. λ is subject to distribution), with varying barrier height or asymmetry parameter. This results in a broad distribution of the tunneling rates and further to a high dispersion of hole growth kinetics [12, 35]. Based on mechanism described in Ref. 12 a model for persistent hole burned spectra and hole growth kinetics calculation has been developed [12, 35, 36], which we are going to expand further.

4.4. The model of NPHB and HGK for a chromophore-glass system

A model for NPHB and PHB (including HGK) of the S_0 - S_1 origin absorption bands of chromophores in amorphous hosts such as glasses, polymers and proteins at low temperatures have been developed in ref [35]. This model includes some assumptions as follows, [33]:

- *linear electron–phonon coupling.* The peak frequency of phonons that couple to the electronic transition is very low (~20 cm^{-1}).
- three distributions that lead to dispersive hole growth kinetics:

1. *λ-distribution.* The λ-distribution is the most important distribution, the distribution for the tunneling parameter between the bistable configurations of the chromophore-host system that are interconverted by hole burning
2. *ω distribution* - The ω-distribution accounts for the fact that ZPLs whose Lorentzian profiles overlap the laser profile can be exactly resonantly at ω_B or off-resonance. This distribution is also responsible for pseudo-PSB.
3. *α distribution* – The α-distribution comes from the fact that α, the angle between the polarization of the burn laser and the transition dipole of the chromophore, varies from molecule to molecule in a random fashion as molecules/complexes are randomly oriented.

Thus, the absorption spectrum after a burn at ω_B with photon flux P and burn time t and assuming that the laser linewidth is much narrower than the width of the ZPL, is given by [10] the following master equation:

$$A(\Omega,t) = 1.5\int d\omega L(\Omega-\omega)G(\omega)\int d\lambda f(\lambda)\int d\alpha \sin\alpha \cos^2\alpha e^{-P\sigma\phi(\lambda)L(\omega-\omega_B)\cos^2\alpha t} \tag{4:1}$$

where ω is the frequency of the zero-phonon line (ZPL); $G(\omega)$ is the Gaussian distribution of ZPL frequencies, or site-distribution function (SDF); $L(\Omega-\omega)$ is the single site absorption spectrum that consists of the ZPL and PSB. It is given by

$$L(\varpi_B - \omega) = \exp-[\sum_k S_k(2\bar{n}_k + 1)]\prod_{k=1,2}\sum_{R=0}^{\infty}\left(\frac{{S_k}^R}{R!}\right) l_{R,k}(\omega_B - \omega - R\overline{\omega}_k). \tag{4:2}$$

where l_R are line shape functions with R=0, 1, 2… corresponding to the zero, one-, two-,… phonon transitions. For instance, l_0 is the Lorentzian zero-phonon line. The width of the homogeneous ZPL contributing to $L(\omega)$ is determined not by τ_1, but by the total dephasing time τ_2. $1/\tau_2=1/(2\tau_1)+1/\tau_2^*$, where τ_2^* is pure dephasing time.. Homogeneous line width is $\Gamma_{hom}=1/\pi c\tau_2$, where Γ_{hom} is in cm^{-1} and c is speed of light in cm/s. S_k, ω_k and $\bar{n}_k$ are the Huang-Rhys factor, frequency and thermal occupation number of the k-th coupled phonon / vibration. $\bar{n}_k$ are temperature-dependent. The phonon side band peaked at ω_m can be described by a Gaussian on its low energy side (side closer to ZPL) and a Lorentzian on its high energy side. $f(\lambda)$ is the normalized Gaussian distribution function for tunneling parameter λ, centered at λ_0 and having standard deviation σ_λ. As stated above, α is the angle between the polarization of the burn laser and the transition dipole of the chromophore. σ is the integrated absorption cross section of the chromophore with transition dipole parallel to laser polarization. $\phi(\lambda)$ is the hole burning quantum yield given by

$$\phi(\lambda) = \frac{\Omega_0 \exp(-2\lambda)}{\Omega_0 \exp(-2\lambda) + \tau_{fl}^{-1}}; \tag{4:3}$$

$\Omega_0 \exp(-2\lambda)$ is the tunneling rate, Ω_0 is the constant pre-factor in the Fermi-Golden rule expression for the TLS relaxation rate for NPHB and τ_{fl} is the fluorescence lifetime (i.e. τ_1).

One could note that for t=0 the Equation 4.1 yield the pre-burn absorption spectrum, as it becomes the convolution of the unmodified Gaussian SDF and of the single site absorption spectrum. *The hole burning spectrum* is defined as the post-burn absorption spectrum minus pre-burn absorption spectrum: $HBS = A(\Omega, t) - A(\Omega - 0)$. The fractional hole depth at time t is given by $FHD = 1 - \frac{A(\omega_B, t)}{A(\omega_0, 0)}$.

At this point the model does not include the treatment of the anti-hole absorption due to NPHB and of light-induced hole filling (LIHF). To account for the effects of photoproduct absorption and LIHF in the calculated spectrum some assumptions have been made [35]. For instance, it has been assumed that in the act of LIHF any given photoproduct site reverts to the educt site from which it originates (the "perfect photomemory model") and the hole burning and LIHF tunneling rates of a given site are equal [35]. The latter model allows calculation of hole-burned spectra in glasses for a certain set of parameters and wide range of irradiation doses. To calculate the hole spectra for systems like photosynthetic pigment-protein complexes this model has to be modified further.

4.5. The model of NPHB and HGK for photosynthetic pigment-protein complexes (Including Energy Transfer)

The model developed in ref. [35] for the case of the chromophores well isolated from each other in a glassy matrix does not account the distribution of the homogeneous line widths due to variations in EET rates. Distribution of excited state lifetimes due to pure dephasing variations from molecule to molecule has been considered in [38] and its effect was ruled negligible. The distribution parameters may be very different in the case of EET in photosynthetic complexes.

Thus, the old model [35] was modified by including the lifetime (energy transfer time, τ_{EET}) distributions. The lifetime affects both the homogeneous single-site spectrum (via the ZPL width) $L(\omega_B - \omega)$, and the spectral hole burning yield $\phi(\lambda)$ that now is given by [38]:

$$\phi(\lambda, \tau_{EET}) = \frac{\Omega_0 \exp(-2\lambda)}{\Omega_0 \exp(-2\lambda) + \tau_{fl}^{-1} + \tau_{EET}^{-1}} \tag{4:4}$$

The new master equation that calculates the absorption spectra is given by [38]:

$$\begin{aligned} D(\Omega,t) = 1.5 \int d\omega L(\Omega - \omega, \tau_{EET}) G(\omega) \int d\lambda f(\lambda) \int d\tau_{EET} T(\tau_{EET}) \times \\ \times \int d\alpha \sin\alpha \cos^2\alpha \, e^{-P\sigma\phi(\lambda,\tau_{EET}) L(\omega_B - \omega, \tau_{EET}) t \cos^2\alpha} \end{aligned} \tag{4:5}$$

where $T(\tau_{EET})$ is the distribution of excited state lifetimes and all other quantities are the same as in Equation 4.1 above.

The new model includes some assumptions as follows, [38]:

- There is no correlation between the SHB rate $\Omega_0 \exp(-2\lambda)$ (governed by the TLS dynamics) and energy transfer time (governed by inter-pigment interactions and spectral overlaps).

- For the sake of simplicity, the distributions of the homogeneous line widths $\Gamma=(2\pi\tau_{EET})^{-1}$+constant pure dephasing-limited width, rather than the distributions of the lifetimes;

The effects of the homogeneous line width distributions are not the main focus of this work. Other effects resulting from the multichromophoric nature of the photosynthetic complexes, for example the oscillator strength distributions (for delocalized excitonic states) have proven to have negligible effect on spectral hole evolution. More importantly, protein dynamics is expected to be somewhat different in the case of protein as compared to the case of glass. These differences will be described in the next subsection.

4.6. Protein dynamics, energy landscape further development of hole burning model

Proteins are supra-molecular machines that perform a large variety of tasks in living organisms and that in their native state have a well-defined highly ordered tertiary structure [11, 39-42]. However, to perform a biological function proteins don't have to be rigid structures. As proved by X-ray crystallography, proteins do not possess a unique state of minimum free energy but assume a large number of slightly different structures (states), called conformational substates. These conformational substates can be represented by nearly isoenergetic local minima in a complex free energy landscape, separated by energy barriers that have to be surmounted during a conformational change, that can be crossed either by tunneling or thermal activation [11, 39-42]. The term "energy landscape" refers to the potential energy hypersurface and it features a large number of minima, maxima, and saddle points]. Each minimum in this landscape represents a different conformational substate that corresponds to a different arrangement of the atoms [39]. In the energy landscape, the conformational substates are grouped into hierarchical tiers that can be characterized by the average energy barriers between the states belonging to each tier. The distribution of energy barriers is broad. A consequence of this broad distribution is that the dynamics of proteins cover a wide range of time scales. Chromophores embedded in the proteins feel the conformational fluctuations of proteins because there are fluctuations in the local distance-dependent interactions. Thus, the electronic transition frequencies of these chromophores change and conformation fluctuations of proteins can be monitored by optical spectroscopy [11, 39, 40].

Energy landscape in proteins can be considered the further development of the two-level system (TLS) model in glasses. The main difference between these models is that proteins have structures in which the conformational substates are hierarchically organized, while glasses are randomly disordered [11, 39, 40]. The observations on evolution of hole spectra in proteins as a function of time leads to conclusion that proteins show spectral diffusion phenomena somewhat different from those in glasses. Spectral diffusion observed in temperature cycling experiments may be used to measure barriers or even distribution of barriers in the energy landscape of a protein [11, 41] in the electronic ground state. SMS experiments [45-50, 59-63] allow one to observe the protein-induced spectral fluctuations on a single molecule level.

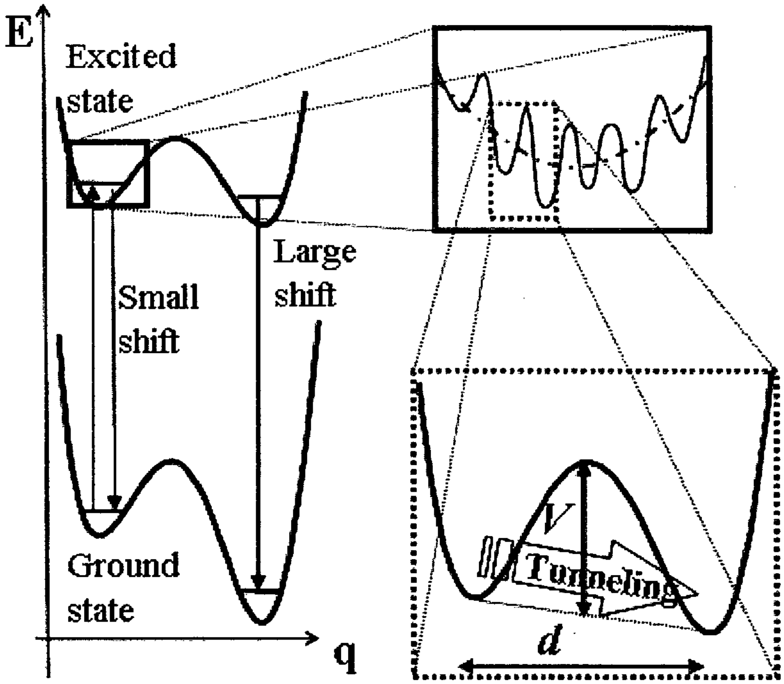

Fig. 4.4 NPHB mechanisms accounting the different hierarchical tiers on the energy landscape (from ref. 38)

As may be deduced from the discussion in the previous subsections, in addition to SMS and long-term spectral diffusion in the dark [68] experiments, other experiments are possible, for instance the hole growth kinetics measurements, including the influence of NPHB anti-hole on that kinetics, with which one can, in principle, determine the magnitudes and probabilities of various spectral fluctuations and respective barriers.

The number of the similar but non-identical substates of the protein is significantly larger than two (as in TLS). To reflect this fact, one needs to depart from the perfect spectral memory model developed in [35] for glasses and to allow for spectral shifts between multiple spectral positions. Namely, it was assumed that molecules starting at ω_{init} before burning are redistributed around ω_{init} according to a certain distribution, called anti-hole function, as a result of burning. Technically, the following sequence has been repeated in a loop: The SDF of the burnt molecules, $G(\omega)\cdot(1-\exp(-Pt\sigma\phi L(\omega-\omega_B)\cos^2\alpha))$ was convoluted with the properly normalized anti-hole function, and added to the burnt SDF $G(\omega)\cdot\exp(-Pt\sigma\phi L(\omega-\omega_B)\cos^2\alpha)$. This results in a modified shape of the SDF $G(\omega)$, without change in its normalization. (One starts with $G(\omega)$ being Gaussian). Unlike in [43-44], there was no spectral memory (i.e. it was assumed, based on SPCS results for LH2 [45-50] and LHCII [52, 53] that the single molecule line can be found at significantly more than two frequencies) and no correlation was implied between the shifts of the absorption of a molecule in the consecutive steps. The probability of burning at each step of the sequence was still determined by the standard SHB yield formula (Eq. 4.2).

CHAPTER 5 RESULTS AND DISCUSSION

5.1. LH2 complex of purple bacteria

Our studies started from LH2 complex due to the availability, in the literature, of large amount of single complex spectroscopy data for comparison. Originally, our intent was to verify that the phenomena observed in SMS experiments [45-50, 59-63] are manifesting also via SHB. Eventually, we extended our studies to other photosynthetic complexes (see following sections).

5.1.1. Sample preparation – LH2 from *Rsp. Acidophila*

LH2 samples were isolated and purified by the group of Dr. R. Cogdell at the University of Glasgow as described in [54, 55]. Briefly, chromatophores were incubated for 2 h in a 2% LDAO solution and subsequently ultracentrifuged overnight on a discontinuous sucrose gradient. The samples were diluted in a buffer (30 mM Tris/EDTA, pH = 8.0) containing 0.3% LDAO [55]. Immediately before the experiment the samples were mixed with glycerol at a ratio of 1:2 buffer/glycerol (99.9%) in order to form the high-quality transparent glass formation upon cooling.

The low temperature (T=5K) absorption spectra of LH2 shows the two characteristic bands centered at λ = 800 nm (12,500 cm^{-1}; B800) and λ = 850 nm (11,765 cm^{-1}, B850), (Fig. 5.1).

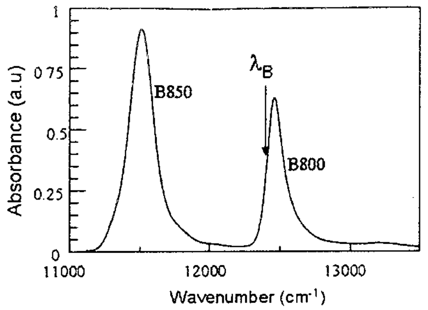

Fig. 5.1 Low temperature (T=5K) absorption spectra of LH2 from *Rsp. Acidophila*

5.1.2 The study of anti-hole absorption of LH2 from *Rsp. Acidophila*

5.1.2.1 The hole growth kinetics of LH2 from *Rsp. Acidophila*

The hole growth kinetics (HGK) curves at λ_B = 807.5 nm for different burning intensities have been recorded and two of these, for I = 0.23 W/cm^2 and I~ 1.37 W/cm^2 are shown in Fig. 5.2. The choice of the wavelength on the lower-energy side of the B800 band has been determined by the observation that at this wavelength the lifetime of the B800 molecule excitations is determined by B800 to B850 energy transfer only, and is not affected by energy transfer between nine pigments responsible for the B800 band.

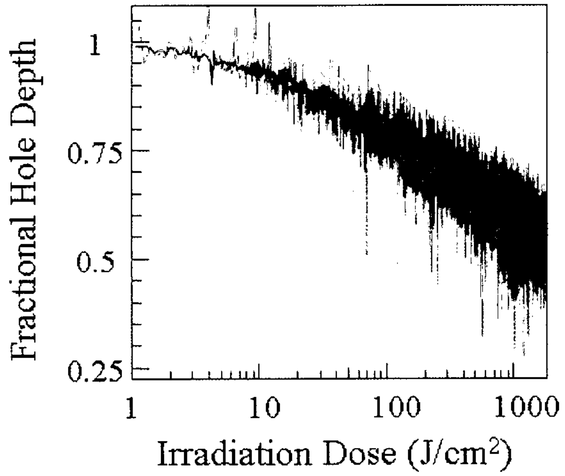

Fig. 5.2 HGK curves obtained at 0.23 W/cm^2 (0.5 s/point; dark gray curve) and 1.37 W/cm^2 (0.1 s/point; light gray curve) at 807.5 nm, as well as hole depths extracted from the spectral holes (red circles for data as measured, blue circles - for data corrected for white-light-induced hole filling, see ref 38 for details on LIHF)

One can notice that the HGK curves expressed as Fractional Hole Depth versus Irradiation Dose do not depend on the burn intensity, both curves (as well as not depicted curves obtained at lower intensities) exhibit similar behavior within this irradiation dose range. The absence of additional fast components of SHB kinetics (for example very fast burning in the beginning on a time scale faster than 0.5 seconds channel length; transient holes) has been assured in another independent way. It has been confirmed that the change of absorbance which can be calculated based on the HGK curves is within experimental uncertainty equal to that obtained from the hole spectra measured after the measurements of the HGK have been finished (i.e several minutes later). Using Beer's law (Chapter 1) one can obtain the following ratio

$$I_{beg} / I_{end} = I_{preburn} / I_{postburn} = 10^{OD_{end} - OD_{beg}},$$

where I_{beg} and I_{end} are transmission signals in the beginning and the end of HGK measurement; $I_{preburn}$ and $I_{postburn}$ are transmission signals at burn wavelength in the unprocessed hole spectra, and OD_{beg} and OD_{end} are respective optical densities. Thus, we conclude that there is no fast burning. Data obtained from the holes reported in the next sections is superimposed onto the HGK curves (each hole is represented by a pair of circles in the Figure 5.2). The upper circles (in red) correspond to the hole depths as measured (next section), while the lower circles (in blue) correspond to hole depth expected in the absence of white light-induced filling.

5.1.2.2 The hole spectra for LH2 of *Rsp. Acidophila*

To study the anti-hole structure (absorption) a set of holes has been burnt into both lower and higher energy sides of the B800 band of the LH2 complex. At 807.5 nm holes have been burnt with various irradiation doses (9.5, 32, 79, 123, 443 and 808 J/cm^2). Figure 5.3 shows these holes.

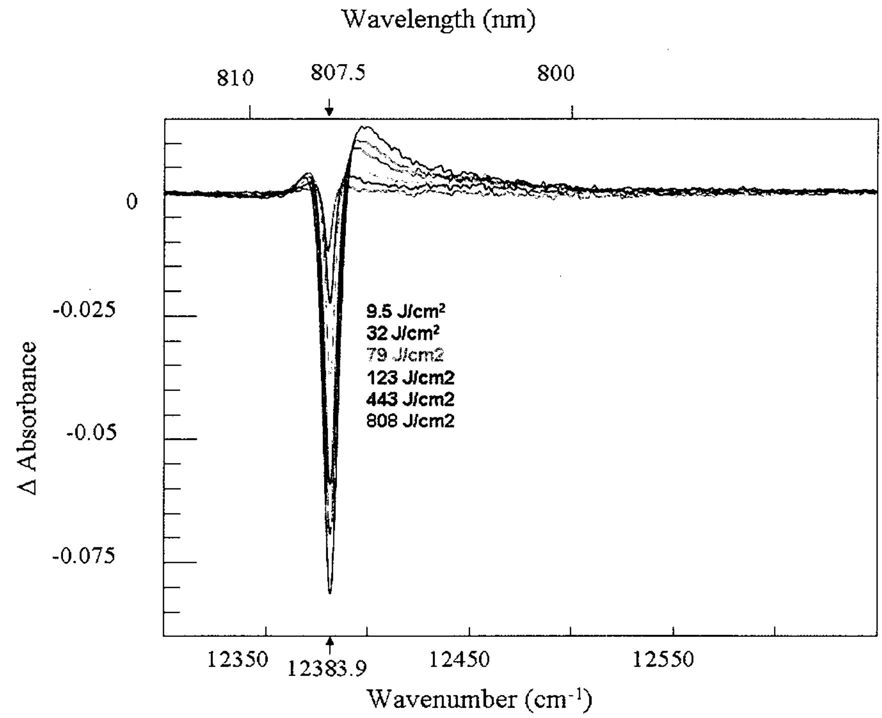

Fig. 5.3 NPHB of LH2 complex of *Rsp. Acidophila* (λ_B = 807.5 nm) for various irradiation doses. T=5K.

Analyzing the holes spectra from Fig. 4.3 one can notice that for shallow hole (I = 80 mW/cm^2 for 120 sec, i.e. irradiation dose of 10 J/cm^2, fractional depth ~5.6%) the width of the zero phonon hole (ZPH) is 4.2 cm^{-1}, which corresponds to the B800→B850 energy transfer time of 2.5 ps, while for the largest burn dose (810 J/cm^2) the width of the ZPH reaches ~8.0 cm^{-1}, and the fractional hole depth reaches ~ 40%.

The observation of just 40% being burnt for such a large irradiation dose is somewhat surprising, as the Huang-Rhys factor S is small for the B800 band (i.e. $S = 0.5$, [57, 59]), and the maximal fractional hole depth is expected to be approximately $exp(-S) = 0.6$ when the hole is burnt into the low-energy side of the absorption band. The reasons of such slow burning include light- and temperature-induced hole filling [56], the geometry of the experiment, and the influence of the SHB anti-hole or just exceptionally low hole burning yield (for some of the molecules).

Due to the non-photochemical nature of the hole burning both real and pseudo phonon sidebands (PSB) are masked by the anti-hole, except for the pseudo sideband for larger irradiation doses. However, the anti-hole absorption is not uniformly distributed over the whole original B800 absorption band, but over much narrower range both to the blue and to the red of the ZPH. It appears that for all irradiation doses the red fraction of the anti-hole approximately compensates the pseudo-PSB. The integral of the hole spectrum over the broad enough spectral range is close to zero, in agreement with the non-photochemical nature of the hole burning process.

To characterize the holes spectra in the above figure the gap between the center of mass of the positive and the negative features of the spectra is considered. The lowest-dose spectrum is almost perfectly symmetrical with respect to the burn wavelength due to the weak electron-phonon coupling and the photoproduct shape centered on the burn wavelength. The anti-hole absorption is peaked at 10 cm^{-1} to the blue and to the red of the burn wavelength. Unfortunately, the signal to noise ratio of this shallowest hole spectrum does not allow for reliable determination of the integral intensities of the positive and negative features. For higher-dose spectra the gap between the centers of mass of positive and negative features gradually increases to ~ 60 cm^{-1}, with anti-hole at higher energy with respect to the resonant hole.

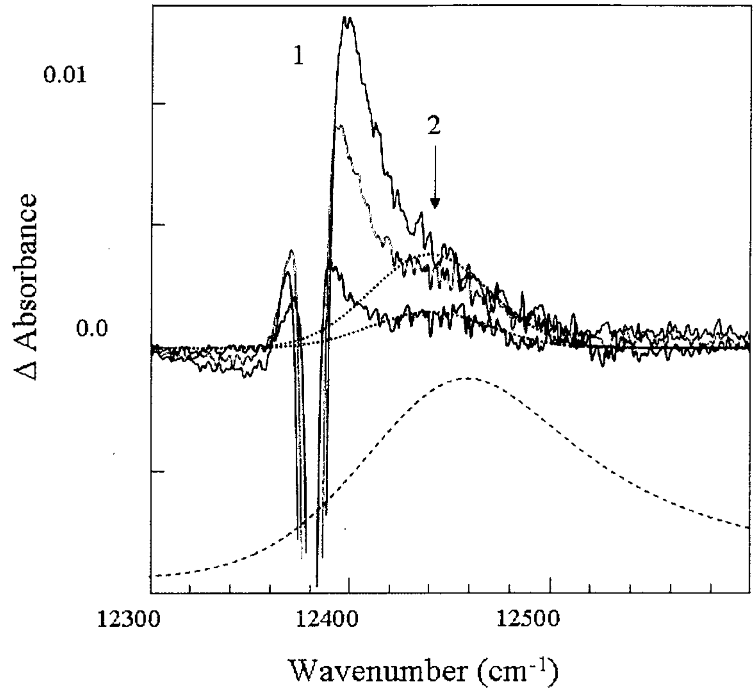

Fig. 5.4 NPHB anti-hole structure for Lh2 complex of *Rsp. Acidophila,* where the numerals 1 and 2 refer to different contributions to the NPHB antihole; dotted curves are the fit to the second, strongly shifted component of the antihole (labeled with the downward arrow); the dashed curve is the B800 absorption

From Fig. 5.4 it is obvious that the anti-hole exhibits quite complicated behavior even for relatively small irradiation doses and that the experimentally observed anti-hole should be described with at least a two-peak distribution (labeled as 1 and 2 in Fig. 5.4). While the first peak is located in the vicinity of the original hole, the second one is shifted much further to the blue (the solid arrow in Fig. 5.4). For realistic shape of the PSB and value of the Huang-Rhys factor S of the order of 0.5, the latter peak cannot be attributed solely to the real phonon sideband of the first one. One could also note that for medium and large irradiation doses the second peak (at ~12460 cm^{-1}) of the anti-hole does not develop as fast as the first one (labeled as 1), i.e. it most likely saturates for relatively low irradiation doses, with the further slow increase of absorption around 12460 cm^{-1} most likely being due to the phonon sideband of the peak 1. This means that large spectral shifts resulting in the formation of the anti-hole peak 2 are experienced only by a small fraction of molecules but the SHB yield for this small fraction is, on average, larger than for the molecules forming anti-hole peak 1. Finally, it is worth to mention that the parameters of the anti-hole illustrated by peak 2 (dotted Gaussian curves) are still significantly different from those of the whole B800 band (see the dashed curve). This indicates that the largest spectral shifts still do not result in redistribution of the molecules' absorption over the whole B800 band.

Figure 5.5 shows the second set of holes that have been burnt at the higher-energy side of the B800 band at 790.5 nm and also a set of calculated spectra (the fit to the SHB action spectrum and the hole due to EET and its anti-hole). Burning at this wavelength enables the B800→B850 and B800→B800 energy transfer. The B800→B800 energy transfer leads to both hole burning yield and induced absorption rate at resonance with the laser are significantly reduced, but the broad hole is formed at lower energies within the B800 band. The complicated hole-burned spectrum structure displays its resonantly burnt ZPH at 790.5 nm, its real and pseudo-PSB, the anti-hole absorption distributed in the vicinity of the resonant hole (similar to the case in Figure 5.3), as well as non-resonantly-burnt broad low-energy hole and its anti-hole.

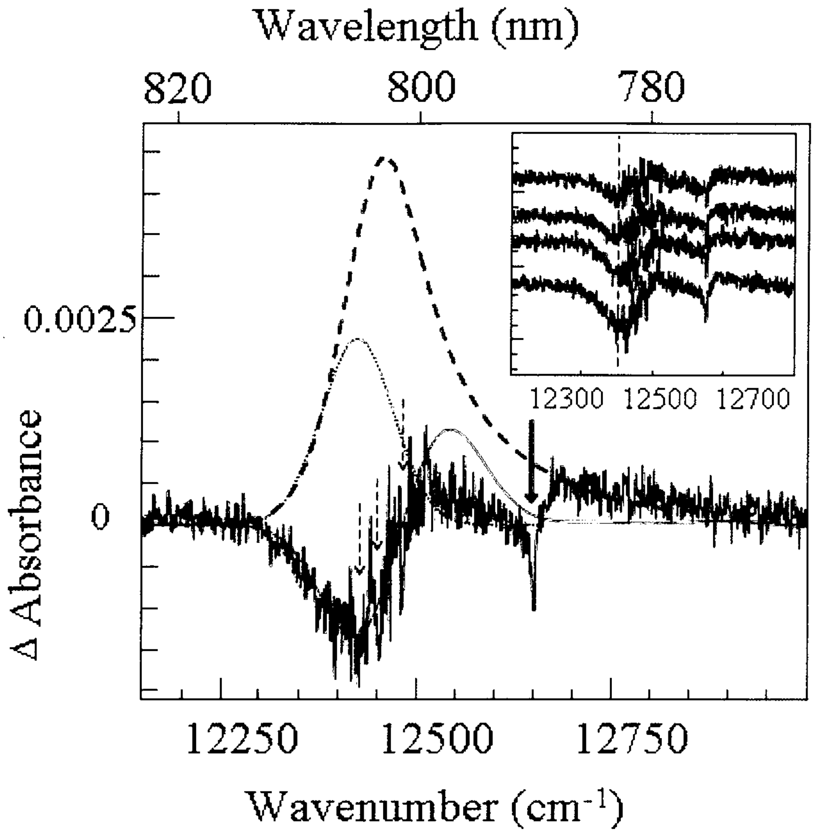

Fig. 5.5 Non-resonantly burned hole spectrum of LH2 complex of *Rsp. Acidophila* (λ_B = 790 nm and 150 J/cm^2), where the dotted line is the fit to the SHB action spectrum, and the dashed line is the B800 absorption band (multiplied by a factor of 0.003); the thin red solid curve represents the hole due to EET and its antihole; dashed arrows show vibronic replicas of the resonant hole; the inset contains nonresonantly SHB for different irradiation doses (50, 85, 100, and 150 J/cm^2, from top to bottom)

The non-resonantly burned hole spectrum shown in Fig. 5.5 displays a set of sharp satellite holes (indicated by the dashed arrows) at 168, 197, 224 cm^{-1} (with respect to the resonant ZPH) that are its vibronic replicas (i.e., ZPLs burnt via vibronic bands due to intra-molecular vibrations) [57], and not a part of the broad feature due to B800→B800 energy transfer. These vibronic holes are accompanied by narrow anti-hole features (the positive spikes between the vibronic holes). The main feature of this non-resonant burned spectrum is that the anti-hole of the broad hole due to the B800→B800 energy transfer is strongly blue-shifted with respect to the broad hole itself.

The average shift of transition energies of pigments burned within the B800 band has been roughly estimate at about 60-70 cm^{-1}. In this respect two assumptions have been made. First, it was assumed that the SDF of the burned fraction of the B800 band can be described with the same curve as the SHB action spectrum that has been taken from [58] and that the anti-hole SDF of that broad hole is also Gaussian in the first approximation. The red derivative-like curve in Figure 5.5 is the sum of these two Gaussians, lower-energy one (broad hole centered near 12430 cm^{-1}) for the initial absorption which has been burnt, and the higher-energy one – for the anti-hole absorption. Interestingly, the area of the former Gaussian is just 0.17% of the area under the B800 band, or 0.5 % of the integral intensity of the absorption of B800 molecules incapable of the B800→B800 energy transfer, and therefore more prone to spectral hole burning. Increasing the irradiation dose from ~150 J/cm^2 to ~300 J/cm^2 (at 791.8 nm, where OD is slightly higher, and therefore the fraction of absorbed photon flux also higher) resulted in just 20% increase in the integral intensity of the burnt band (other parameters of the band could stay the same and still result in a good fit. This indicates that the position of the broad feature near 12430 cm^{-1} is not correlated with the burn wavelength, in agreement with this broad hole being due to energy transfer). Such behavior also indicates that the fraction of B800 molecules experiencing large spectral shifts in this experiment is quite small. It needs to be stressed that the shape of the broad non-resonant hole and its anti-hole in Figure 5.5 is only weakly dependent on the irradiation dose (see insert of the Figure 5.5), which in turn suggests that the feature is formed as a result of one large spectral shift per each individual B800 molecule line rather than as a result of many small shifts. Otherwise one would expect gradual migration of the derivative-like hole-antihole feature to higher energies.

5.1.3 Discussion on LH2

The goal of this study was to determine if the hole burning results would be compatible with the available SMS data, i.e. if the protein dynamics parameters obtainable from the latter would yield agreement between theory and experiment in terms of SHB. Both the widths of the spectral lines / holes and the shape of the anti-hole are expected to be affected by protein dynamics. The widths of the spectral holes or SMS lines in LH2 are determined by excitation energy transfer times and by the spectral diffusion occurring in steps smaller than the hole width and at the timescale faster than the time scale of the experiment.

SMS data is available in Refs [59-63, 45-50] in the forms of a) distributions of line shifts between consecutive laser scans (SMS experiments on LH2 were performed in fluorescence excitation mode), b) the distributions of the line widths, which (widths) change from scan to scan for the same line and c) first moment or first cumulant distributions. In the latter case the information on the exact sequence of shifts is lost, but one can see at which wavelengths the line is more likely to be found as it jumps between multiple positions. The shift distributions are dominated by very small, 1-2 cm^{-1} shift. This allows one to estimate the likely shape of the anti-hole function (see Chapter 4) as a Gaussian with the width of a few cm^{-1}. Note that in this case one has somewhat unusual situation as anti-hole function width is comparable to the width of the ZPH. Moreover, analyzing the photon budgets of the SPCS experiments one can arrive to the probabilities of molecules to experience light-induced spectral shifts, which in our SHB model are nothing else but the HB yield ϕ. From the latter the average value of the tunneling parameter λ can be estimated as 7.8. (see Ref [38] for details) Taking into account that the line widths changed from scan to scan, one could also conclude that lines in SPCS experiments experienced not one, but several jumps per scan, and, therefore, that this value of lambda is just the upper limit (lambda values corresponding to the larger shifts can be estimated using the similar logic, and they appear to be much higher). Thus, HB process is supposed to be dominated by smaller shifts.

To fit the HGK curves from Fig. 5.2 and the holes in Fig. 5.3 the modified SHB model including anti-hole absorption has been used. The goal of the fit was to determine a set of parameters (the peak and mean of the tunneling parameter distribution, the shapes of the phonon side band and of the anti-hole distribution) which allows for satisfactory fitting of all the holes in the series, taking into account the burn times and intensities used in the experiment. The key assumption is that the burnable fraction of the B800 molecules is represented by the HB action spectrum, which is peaked at 12425 cm^{-1} (804.8 nm) (to the red of the B800 band maximum), and has the width of 108 cm^{-1}, (the dotted line in Fig. 5.4). Therefore, the hole at 12381 cm^{-1} was burnt 44 cm^{-1} to the red with respect to this sub-band maximum. The PSB parameters have been chosen such way to obtain single-site absorption (SSA) spectrum similar those in Refs. 48 and 64. In the process of fitting it was determined that the distribution of PSB parameters and of the oscillator strengths (the latter resulting from excitonic interactions between the pigments of the B800 ring) provide negligible contribution to the dispersion of SHB kinetics and they have been neglected. For an appropriate calculation of both HGK curves and SHB spectra a large variety of the anti-hole functions has been tested. These functions have been Gaussian and Lorentzian functions centered at burn frequency, slightly blue-shifted Gaussian and Lorentzian functions, and two-component anti-hole functions corresponding to situation when molecules can experience also large spectral shifts but with smaller probability. The results of these calculations are presented in the following figures.

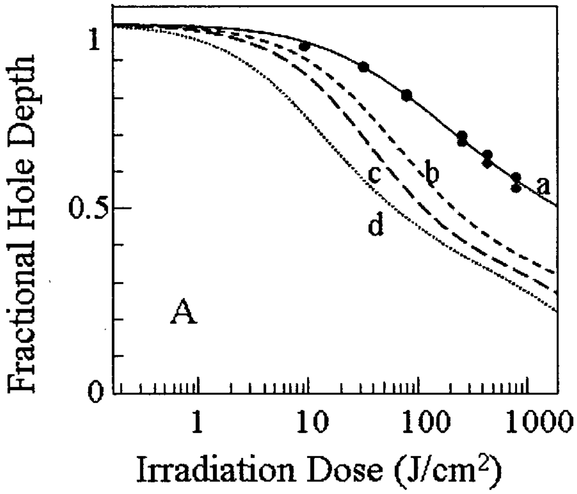

Fig. 5.6 The HGK calculated curves for $\lambda_0 = 7.8$, $\sigma_\lambda = 0$ and various shapes of the anti-hole function

The calculated HGK for the upper limit ($\lambda_0 = 7.8$) for small shift tier of the protein energy landscape according to SHB yield (i.e. 1/450 000), $\sigma_\lambda = 0$ and various shapes of the anti-hole function are presented in Fig. 5.6. In this figure one can notice the first curve (a) that represents a good fit to the experimental data. It was obtained with the non-shifted Gaussian anti-hole function with the width of 1.1 cm^{-1}. The next two HGK curves (b and c) were obtained assuming the presence of larger (~10 cm^{-1}) shifts in addition to small (i.e. ~1 cm^{-1}) ones. In the case of curve (b) the relative probability of the large shifts was assumed to be 0.025, which corresponds to $\lambda_0 = 9.6$ for the next tier of the energy landscape, and for the case (c) that probability was assumed to be 0.05 (next tier $\lambda_0 = 9.2$). The last curve was obtained for non-shifted Lorentzian anti-hole function having the width of 1.1 cm^{-1}. It should be mentioned here that increasing σ_λ results in more dispersive HGK curves but not slower on average. A significant increase of σ_λ would make the calculations inconsistent with experiments.

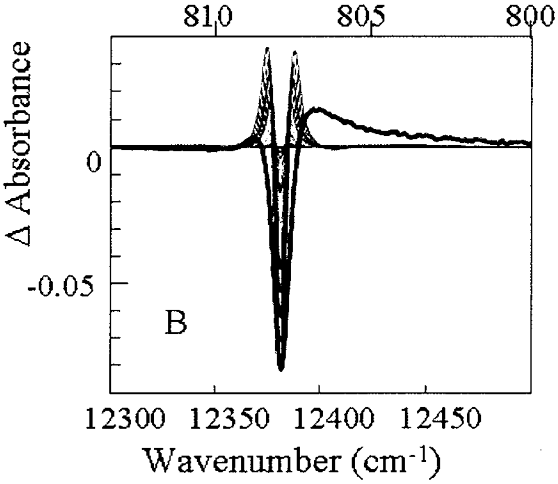

Fig. 5.7 The spectral hole burnt at λ_B = 807.5 nm and the spectral hole calculated for λ_0 = 7.8, σ_λ = 0, non-shifted Gaussian anti-hole function with the width of 1.1 cm^{-1} and several irradiation doses.

We conclude that for this range of λ values one can successfully fit the experimental HGK only if one assumes that anti-hole function is a single non-shifted Gaussian with very narrow, ~1.1 cm^{-1} FWHM, in some disagreement with the reported SPCS data in ref. 51. Reduction of tunneling parameter ($\lambda_0 < 7.8$) results in further decrease of the anti-hole distribution width required to fit the SHB kinetics. Any anti-hole models allowing even a small fraction of the molecules to escape further from the excitation energy than a fraction of a cm^{-1} resulted in calculated HGK becoming too fast. Figure 5.7 presents the fitted holes for the set of parameters used to obtain the curve (a) in the Figure 5.6. The figure proves that the parameters used for the best fit of hole growth kinetics (curve a) do not result in an appropriate fit of overall hole shapes. One also has to note that the line width (EET rate) distribution has been turned off to limit the dispersion of the kinetics curves.

Thus, we allowed the parameters of the anti-hole function and of tunneling distribution parameters to vary freely until we were able to achieve the satisfactory fit to the experimental data. In this new case the simultaneous gradual adjustment of the parameters of the tunneling distribution and of the anti-hole function has been performed in order to determine the optimal set of parameters which would actually results in a satisfactory match between experimental SHB data and simulations. These new theoretical curves that best match the experimental curves are presented in Figure 5.8.

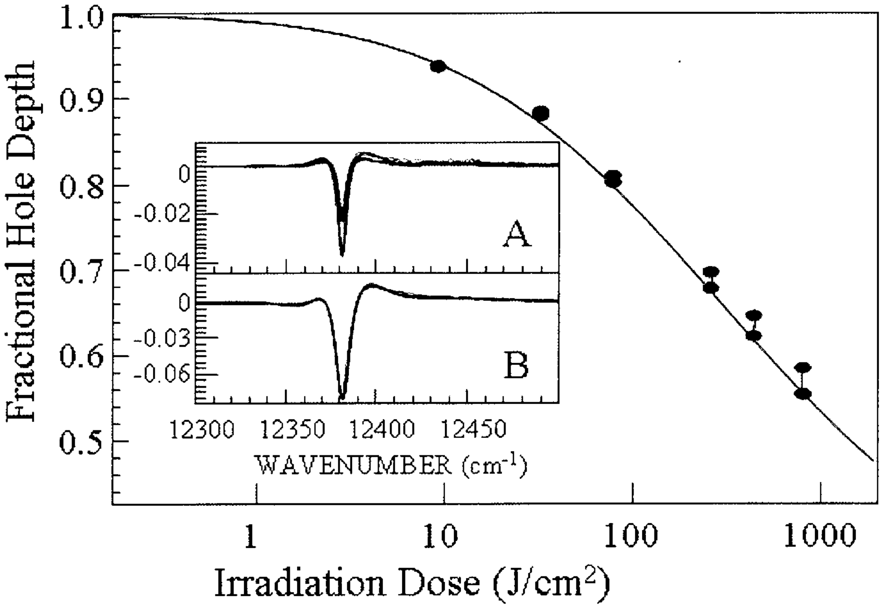

Fig. 5.8 The best fit to HGK and the overall shape fit of the shallowest and deepest holes in the series burned at 807.5 nm (inset A and inset B respectively). The blue and red noisy curves are the experimental holes.

The figure above shows the best fit to HGK curves and the best fits to the holes obtained with low (inset A) and high (inset B) irradiation doses (see Chapter 3 and Chapter 4) . For these fittings the electron-phonon coupling parameters and the line width distribution have been chosen from ref. 57 and 60, respectively, and they were fixed throughout the fitting procedure. However, it was noticed that varying the Huang-Rhys factor S within reasonable limits does not affect the fits significantly because a slight increase of S may be compensated by slight decrease of the λ_0 (or vice versa) while the quality of the fit is preserved.

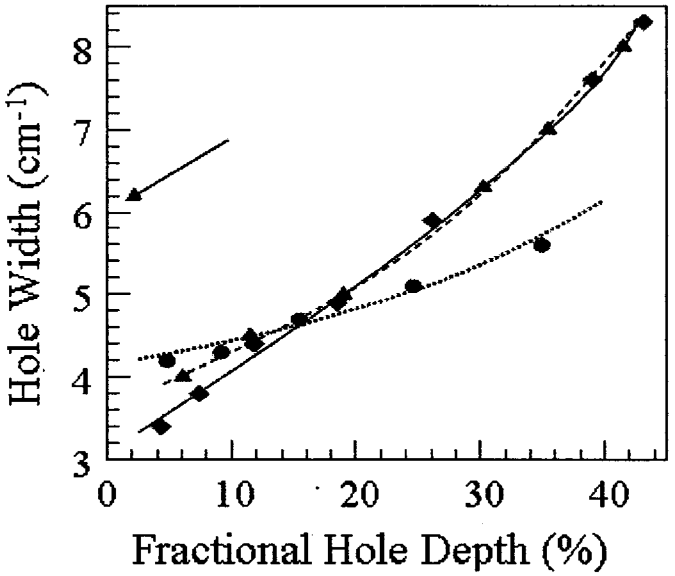

Fig. 5.9 Experimental dependence of the hole width on the fractional hole depth (triangles, dashed line), predicted dependence (based on eq. 4.5) in the absence of a homogeneous line width distribution (circles, dotted line), and predicted dependence assuming the distribution of line widths from ref 63 (diamonds, solid line). The value of the (shallow) hole width expected based on the time-domain data (i.e., about 6 cm^{-1}) is indicated by an arrow.

The hole width dependence on fractional hole depth (diamonds) obtained with the same parameters as data in figure above, along with the experimental data (triangles) and data simulated in the absence of the line width distribution but all other parameters being same (circles) are presented in Fig. 5.9. As mentioned, the line width distribution from reference 60 was employed and it is obvious that the match is quite satisfactory

The parameters employed for these fittings are summarized in the Table 5.1.

Table 5.1 Parameters to the best fit to the hole shape and HGK curves

Fitting parameter	**Parameter values**
phonon sideband	$S = 0.45 \pm 0.05$, $\omega_{\mathrm{peak}} = 25$ cm^{-1}, Gaussian/Lorentzian fwhm of 22/40 cm^{-1}
homogeneous line width	distribution from ref. 65 based on the whole B850 DOS, peaked at 3.3 cm^{-1} (1.6 ps)
Antihole, tier 1, shifts ~ 1 cm^{-1}	$\phi > 10^{-6}$, $\lambda_0 \leq 7.8$, $\sigma_\lambda \leq 0.1$; not observed in SHB experiments
Antihole, tier 2, shifts ~ 7-10 cm^{-1}	fwhm = 35 ± 5 cm^{-1}, shift = 3 ± 1 cm^{-1}, $\lambda_0 = 10.3 \pm 0.2$, $\sigma_\lambda = 0.7 \pm 0.2$ ($\phi \approx 10^{-8}$)
Antihole, tier 3, shifts ~ 60 cm^{-1}	fwhm = 70 ± 10 cm^{-1}, shift = 60 ± 10 cm^{-1}, $\phi \approx 10^{-7}$; note that only several percent of molecules are capable of such large shifts

The absence of fast small-step spectral diffusion is confirmed by following, for ~2 hours after the end of burning, the holes burned at similar wavelengths. Within the experimental uncertainties, the holes did not exhibit broadening. If spectral diffusion was indeed described by shift distributions from SMS data [59-63], the holes would broaden to approximately the width of the first cumulant distribution from [45], i.e. to 8-10 cm^{-1}. Several additional remarks can be made with respect to the Table 5.1. First, the reported SHB yields for the medium (i.e. ~10 cm^{-1}) and large (i.e. ~60 cm^{-1}) shifts are in agreement with the photon budgets of the SMS experiments. In this work *all* B800 molecules were assumed to be in principle capable of ~10 cm^{-1} spectral shifts, contrary to what was suggested based on the results of the SMS experiments [45]. However, if one takes into account the parameters of distribution of HB yields resulting from our analysis, there is no contradiction: some molecules followed in SMS experiments just did not experience the Tier-2 shifts within the timeframe of the SMS experiment. Note that 35 cm^{-1} FWHM of the anti-hole distribution on this tier of the energy landscape corresponds to the ~9 cm^{-1} average shift regardless of direction, i.e. it is in agreement with SCPS results. It is unclear if the requirement for a "little nudge to the blue" (3 cm^{-1} blue shift of the anti-hole function) is an artifact resulting from the calculation algorithm used (e.g., insufficient number if iterations) or is the reflection of real physics, or both. One could argue that the spectral shifts towards global minimum on the protein energy landscape (corresponding to the maximum of the B800 band) could be slightly more probable than in the opposite direction. The largest (~60 cm^{-1}) spectral shifts seem to be observed for only 5% of the B800 molecules (as assumed in calculating the spectra shown in frame B of the insert of Figure 5.8, and the HGK curve in the main frame of that figure). Closer look at the low-dose hole spectra suggests that about 10% of molecules capable of larger shifts would be required to produce better fits to the lower-dose holes (see frame A of the insert in Figure 5.8, as well as Figure 5.2). Thus, it appears that if a given molecule is capable of the Tier-3 (60 cm^{-1} on average) shift at all, the average SHB yield of that process must be higher than for Tier-2. Small fraction of molecules capable of large shifts (tens of cm^{-1}) suggests that the structural rearrangements responsible for Tier-3 dynamics are atypical, and probably a consequence of some distortions of the normal structure of the LH2 complex. This suggestion, if confirmed, could also explain dependence of the frequency of incidence of the large shifts on species [66] and sample preparation.

Finally, in the light of the absence of noticeable hole broadening which indicates significant degree of spectral memory for Tiers 2 and 3 of the energy landscape, we also attempted to fit the HGK data utilizing perfect memory model from [35], i.e. the model where each pigment molecule is interacting with one and only one TLS. Satisfactory fits to HGK data (not shown for brevity) can be obtained for $\lambda_0 = 9.3$ with other fit parameters being same as above. The latter simulation provides the *lower limit* of λ_0 for B800 band of LH2 since, according to the SPCS data [45], more than two distinct states on the Tier 2 of protein energy landscape were frequently observed. Interestingly, this lower limit for λ_0 is still significantly larger than typical $\lambda_0 \sim 8$ obtained for various glasses [35, 56, 61, 62].

Summarizing, in our SHB experiments on LH2 we do not observe any evidence of spectral diffusion with parameters corresponding to the lowest-barrier tier of the protein energy landscape suggested by SMS. There are several possible reasons for this discrepancy. One, most probable of these reason could be related to the fact that the small spectral shifts originate from the interaction of the chromophore with the tunneling entities at the distance of approximately 1 nm away, which places these entities at the protein / amorphous host interface and beyond. The difference in the sample preparation procedures in SHB and SMS experiments could explain the difference in outside amorphous host or protein interface dynamics. Another reason that is not very plausible, but it cannot be completely excluded, could be related to the higher excitation intensity in SMS experiments driving the molecules into conformational states less accessible or unavailable in the dark / lower light conditions.

5.2. Low-temperature Protein Dynamics of Several Small Light-harvesting Complexes Probed via Spectral Hole Growth Kinetics Measurements

In the previous section we presented an analysis of the spectral hole shape evolution for B800 band of the LH2 antenna complex of *Rps. Acidophila.* This analysis has been based on the theoretical models (Chapter 4) originally developed for glasses, which share many important properties with the proteins. A SHB model has been introduced allowing chromophore / environment system to assume multiple conformations [38 and Chapter 4]. Surprisingly, our SHB data proved incompatible with the lowest-barrier tier SMS dynamics reported in [45, 46, 70, 64], while agreeing both qualitatively and quantitatively with the higher tiers dynamics [38]. The number of possible conformations on the higher tier(s) of the protein energy landscape, however, appears to be limited. The same conclusion has been reported in room-temperature SMS experiments [52, 71, 72]. All these arguments suggest that original SHB models, extended to include Multi-Level Systems (MLS) still may be satisfactory for these tiers.

In this chapter the detailed hole burning models described in section 4.6 and Ref 38 will be applied to determine the protein dynamics parameters affecting the evolution of the spectral holes during burning for several protein antenna complexes [19–27]. This approach allows for determination of the impact of the protein dynamics on non-photochemical hole burning, and for subsequent disentangling of these effects from the effects related to the distributions of the energy transfer (EET) rates. The distributions of the EET rates measurable in the SHB experiments on higher-energy states of the complexes can then be compared to those theoretically predicted from the structure data, and additional constraints for transition energies of the chlorophylls in the absence of inter-pigment interactions can be obtained. The latter energies are still not precisely determined for most of the chlorophylls in most of the photosynthetic complexes.

Non-photochemical spectral hole burning (SHB) has been used to probe the low-temperature protein dynamics of CP43 core antenna complex and CP29 peripheral antenna complex of spinach Photosystem II, as well as of trimeric and monomeric LHCII complexes associated with pea Photosystem I.

For all complexes being studied, the same sequence of measurements has been performed. First, the hole burning action spectrum was measured at high resolution and low irradiation dose. HB action spectrum is the dependence of the hole depth on wavelength for fixed irradiation dose. It represents a weighted sum of the (parts of the) SDF of the two (or more) lowest-energy pigments as has been considered in ref. 73. Only the lowest-energy pigments of the complexes have been probed in hole growth kinetics measurements to guarantee that there is no contribution of the dispersion of the excited state lifetimes (dispersion of the line widths) to the dispersion of the hole growth kinetics. In this case all HGK dispersion can be ascribed to the distribution of the barriers between different conformational states of the protein alone. The value of the integrated absorption cross-section of isolated Chl *a* molecule has been calculated based on ref. 74 (σ=4.5$\cdot$10^{-13} cm^{2} cm^{-1} for molecules oriented with transition dipole moment parallel to the electric field of the burning light).

As the model used requires many adjustable parameters one should make certain general remarks about the effects of changing these parameters on the hole spectra. The parameters most strongly influencing the shape of the HGK curve are the mean and the width of the tunneling parameter distribution, and the Huang-Rhys factor *S*, describing the strength of the electron-phonon coupling. It is well-known that S can be estimated based on the maximal achievable depth of the resonant ZPH. Thus, a rough estimate of S can be obtained from the HGK curve itself even without any fitting. Other parameters affecting the maximal hole depth are the shapes of the phonon sideband and of the anti-hole function. The mean of the tunneling parameter distribution affects overall burning speed (i.e. how much the HGK curve is shifted towards higher irradiation doses), while the width of that distribution determines the qualitative behavior of the HGK curve. Larger σ_λ results in HGK curve (depicted on a logarithmic scale) more resembling the straight line, smaller σ_λ results in HGK curve being more sigmoidal. Thus, in our fitting procedure, we initially fixed all parameters except S, λ_0 and σ_λ, achieved the best possible fit to the experimental data, and then attempted to fine-tune the shape of the phonon sideband and of anti-hole function to improve the fit further.

5.2.1 CP43

5.2.1.1 CP43-Sample preparation

To isolate and purify the antenna complex CP43 the same procedure as reported in ref [75] has been used. The isolation has been performed at NREL at Golden CO by Drs. Seibert and Picorel. Summarizing, the pigmented product eluted from DEAEFractogel TSK 650s anion-exchange column was then passed through an S-Sepharose cation-exchange column and finally it was loaded onto a Q-Sepharose anion-exchange column at 4 °C equilibrated with the same buffer (20 mM Bis-Tris, pH 6.0, 20 mM NaCl, 10 mM $MgCl_2$, 0.03% (w/v) *n*-dodecyl β-D-maltoside (DM), and 1.5% (w/v) taurine at 22 °C), [75]. The final resulted product was dialyzed twice for 2 h against 1 L of 20 mM Bis-Tris, pH 6.0, plus 0.03% DM and concentrated with 30-kDa cutoff [75]. Dilution with glycerol was performed in order to ensure good glass formation upon cooling.

5.2.1.2 The absorption and SHB action spectra of CP43

The low temperature absorption spectrum of CP43 core antenna complex of Photosystem II is presented in Fig. 5.10.

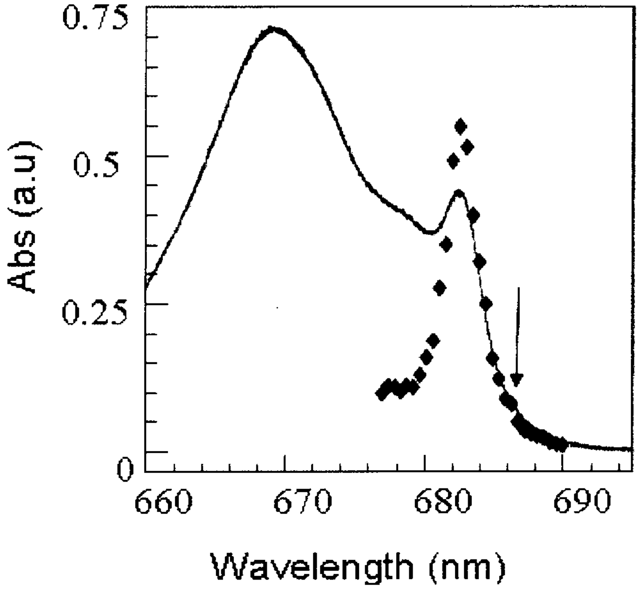

Fig. 5.10 Low temperature absorption spectrum of CP43 (red curve) and the SHB action spectrum of CP43 (black diamonds); the black pointed arrow indicates the burning wavelength (λ_B = 686.8 nm)

This spectrum shows that the chlorophyll *a* molecules display two main absorption peaks. A broad peak is placed at 669.1 nm (OD = 0.75) while a narrow and distinct peak is placed more to the red at 682.7. Similar spectral features e.g. a broad maximum at 669 nm and a very distinct and narrow peak at 682 nm have been reported in ref [19, 75].

It has been mentioned in ref. 73 and 76 that the CP43 protein–chlorophyll *a* core antenna complexes of Photosystem II possesses two quasi-degenerate lowest-energy Q_y-states (labeled as A and B) characterized with different inhomogeneous bandwidths. Thus, the hole-burning action spectrum of CP43 has contributions from both A- and B-state chlorophylls (while A-state is believed to be localized on a single chlorophyll molecule, B state may be somewhat delocalized over several chlorophylls). Due to the static site energy disorder either one or another pigment could be the lowest-energy pigment of the complex [73, 76]. The A-state is considered the major contributor to absorption at 686.8 nm where the HGK measurement presented in the next section was performed (arrow). One can note that the action spectrum normalized to the absorption spectrum in the region dominated by the A state overshoots the absorption in the region of the narrow B state. This indicates that the hole burning effectiveness is larger for the B state than for the A state (λ_0 is smaller).

5.2.1.3 The hole growth kinetics of CP43 of spinach

In Fig. 5.11 the hole growth kinetics curve for CP43 at 686.8 nm and its best fit are displayed. The insert of this figure shows the spectral hole burnt at 686.8nm and recorded immediately after HGK measurement. This spectral hole is characterized by a FWHM of 6.87 GHz and a fractional hole depth of 65%. To obtain the best fit to HGK a set of parameters characterizing the lowest energy states of protein-complex has been chosen from published works [52, 64, 70, 72, 75, 76]. The shape of the SDF of the A-state of CP43 is according to Ref. 76. The homogeneous line width at low temperature (5 K) has also been taken from Ref. 76. Its value of 0.03 cm^{-1} is determined mainly by pure dephasing, since radiative lifetime is as long as 3.5 ns [77, 78]. The electron-phonon coupling parameters for the CP43 A state [77] is weak, S~0.25...0.3, and the phonon sideband [78] is peaked at 17 cm^{-1} (these values are in agreement with extremely small Stokes shift observed for CP43 [76, 79]).

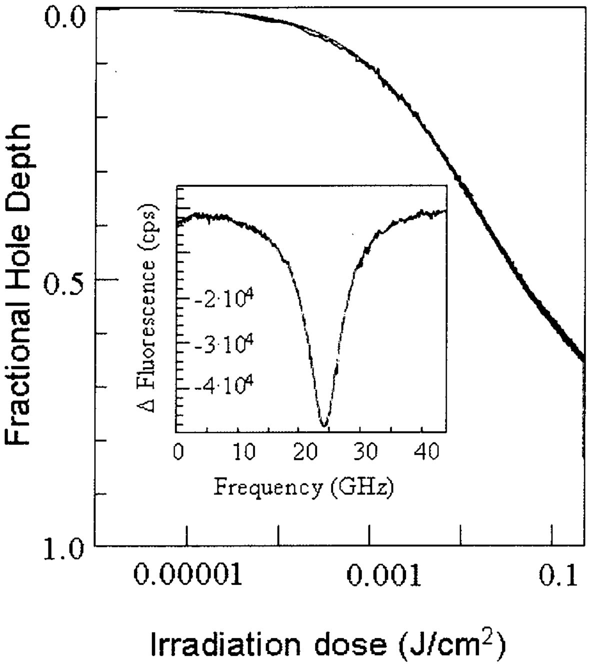

Fig. 5.11 The experimental (black noisier curve) and the best fit (based on eq. 4.5; red curve) to the hole growth kinetics curve of CP43; the insert shows the spectral hole burnt at 686.8 nm

Note that within the framework of the model for EET between two quasi-degenerate states described in [73], the small contribution to the B state which might still be present at 686.8 nm belongs to the B-type pigments being the lowest-energy pigments in the complex, and therefore, further downhill EET from these pigments is impossible. Consequently, contrary to what [78] suggests, non-resonantly excited hole burning **does not** contribute to the low-energy sideband in the respective hole spectrum, and the whole that sideband must in fact be pseudo-PSB. The latter assignment is supported by the observation that the gap between the burn wavelength and the wavelength where this pseudo-PSB feature tapers off stays constant for burn wavelengths longer than 684 nm [78]. It appears that the shape of the pseudo-PSB in case of $684<\lambda_B<686$ nm is determined by the actual shape of the phonon sideband, not by the shape of the SDF, and therefore, we used the phonon sideband shape following from SHB data (See Table 5.3). It is well established that that the A-state of CP43 is localized on a single Chl *a* molecule, therefore the integrated absorption cross-section of one Chl *a* molecule has been used in these simulations. The shape of the anti-hole function was estimated based on unpublished old results by V. Zazubovich and from ref. 78. It is obvious that the anti-hole is distributed both to the blue and to the red of the zero-phonon hole but it is unclear if the anti-hole is on average blue-shifted with respect to the ZPH or not (because of the interference between the red fraction of the anti-hole and pseudo-PSB). We used the Gaussian anti-hole function with the width of 40 cm^{-1} which is centered on ω_{init}. From the Fig. 5.11 the fractional depth is about 65%, which is somewhat less than 78% corresponding to S=0.25 (the maximal fractional depth is given by exp(−S)). The parameters that lead to the best fit to the experimental HGK, Fig. 5.1,) are the following: S=0.3, λ_0=11.0 and σ_λ=1.0. The hole spectrum displayed in the insert of Fig. 5.11 shows a width oh 6.9 GHz only for a depth of 65% indicating that it is not yet saturated. The fact there is no significant anti-hole contributions to this hole spectrum within the scan range of 45 GHz is consistent with the much broader anti-hole function that has been chosen for this simulation.

5.2.2 CP29

5.2.2.1. Sample preparation - CP29

CP29 samples were isolated and purified according to the procedure described in [80] by the group of Klaus-Dieter Irrgang from Berlin. In brief CP29 has been obtained from spinach PSII membrane fragments in the presence of 2 mM benzamidine (Sigma) and 1 mM Pefabloc as protease inhibitors. A two step chromatography was performed to obtain purified CP29. The first chromatography step was running using a CM-sepharose Fast Flow column under dim green light at 4°C and a second chromatography step was applied to obtain sufficiently purified CP29 [80]. To obtain the required concentration of the product the purified CP29 has been centrifuged in Centriprep 10 tubes. The samples were diluted with glycerol as mentioned above.

5.2.2.2. The absorption and SHB action spectra of CP29

At low temperature (T=5 K) the Q_y absorption band of CP29 displays the main peak at 674.7 nm (Fig. 5.12) and a faint shoulder at 664 nm. These two peak positions were assigned to Chlorophyll a molecules of CP29. This absorption spectrum shows also two broad bands located at 638.5 nm and 650.2 nm that are due to the two chlorophylls b molecules of CP29. The final optical density has been about 1.2 at 674.5 nm. Similar spectral features were reported in [21, 22, 80]. This proves that ~10-year storage at about –80C° did not affect the properties of the sample significantly.

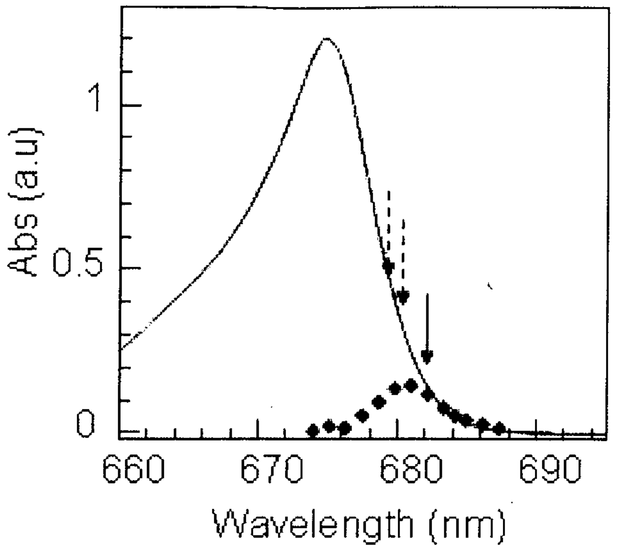

Fig. 5.12 Low temperature (T=5K) absorption spectrum of CP29 (red curve) and the SHB action spectrum of CP29 (black diamonds); the arrows indicate the burning wavelengths

The HB action spectrum has been measured using the dye laser in high resolution mode and the hole growth kinetics for the initial stage of burning at various wavelengths. The maximal irradiation dose (I = 0.005 J/cm^2) used in this work is ten times smaller than in ref. 80. This irradiation dose still leads to fractional hole depths of 25% for the lower-energy edge of the absorption band. The final HB action spectrum reported in Fig. 5.12 has been obtained for irradiation dose of 0.0014 J/cm^2 (from the beginning of the HGK curves that guarantees the holes were far from the onset of saturation) and it displays a maximum at 680.4 nm. The spectrum is somewhat asymmetric. One can remark here that hole burning is effective for the red-most tail of the spectrum. Analyzing both spectra from the Fig. 5.12 a key observation could be done that the absorption of CP29 is dominated by easily burnable lowest state at wavelengths longer than about 682 nm.

The next discussion has two main goals. First goal is to analyze (Fig. 5.13) the asymmetric features of the CP29 HB action spectra and to arrive to the parameters of the

SDF of the lowest state(s). The asymmetry of HB action spectrum of CP29 will be explained by analogy with CP43 [73]. Thus, this is because of the truncation from the high-energy side due to EET between the higher-energy and the lowest energy pigments of each complex [73]. It is important to recall that the exact values of peak and width of the lowest-state SDF do not significantly affect the HGK as long as the SDF provides the good fit to the absorption and action spectra at burn wavelength and at longer wavelengths. The second goal is to determine the realistic range of the oscillator strengths of the lowest state. This is important because HGK parameters resulting from the fit, namely those of the λ distribution, are sensitive to the value of the oscillator strength of the state being burned.

The Fig. 5.13 shows the SDF of lowest-energy pigment 1 (dashed blue curve) with maximum at 680.0 nm and the width of 165 cm^{-1}. Assuming that Q_x bands contribute about 10% of the total absorption [81], and that oscillator strength for the Chl *b* is 0.7 of that for Chl *a*, the oscillator strength of the lowest-energy state corresponds to 0.7 Chl *a* molecules. The SDF of the second-lowest energy state (pigment 2, black solid curve) shows its maximum at 678.25 nm and it is assumed to have oscillator strength of 1 Chl *a* molecule. The third-lowest energy SDF (green curve) is peaked at 675.4 nm.

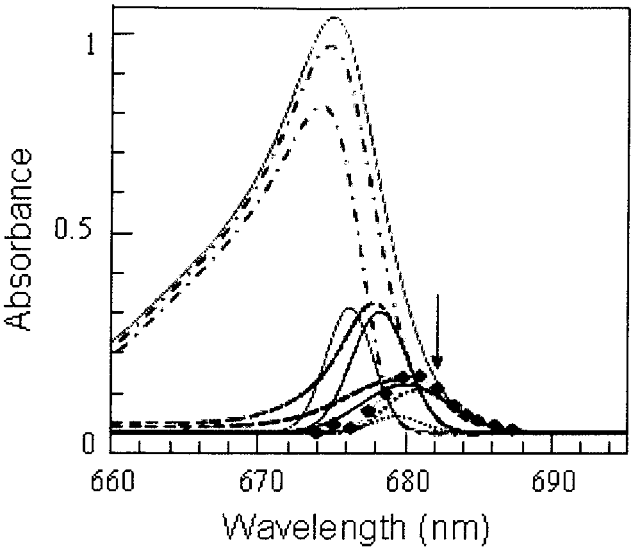

Fig. 5.13 The SDF and the absorption spectrum of the lowest – energy state of CP29; where the dashed blue curve is the pigment 1 SDF corrected with phonons and localized vibrations contribution [82]; dash-dotted red curve is the difference between the whole absorption spectrum (solid red curve) and the lowest-state absorption (dashed blue curve); black and green solid curves are the second and third-lowest energy SDFs; dashed black curve is the absorption spectrum of pigment 2 dressed with phonon and vibration contributions; black dotted curve is SDF of pigment 2 molecules incapable of downhill EET (divided by 3 for clarity, to avoid overlapping with other curves).

In order to achieve satisfactory fit to the action spectrum, one has to assume that the hole burning yield for pigment 2 is approximately 3 times lower than for pigment 1 (the dotted black curve in Figure 5.13 is already corrected by this factor of 3). Shifting the lowest-energy SDF further to the red allows fitting the action spectrum without assuming lower HB yields for other states. However, for lowest-state SDF peaked at 681.0 nm its integral intensity must be equal to that of 0.42 chl *a* equivalents only. As we will see below, HB effectiveness being equal for different states contradicts the HGK data while low integral intensity contradicts the results of excitonic calculations. Shifting the lowest state to the blue results in a situation where, by the time the lowest-state oscillator strength reaches one Chl *a* equivalent, the HB yield for the second-lowest state has to be reduced by at least an order of magnitude. Thus, one Chl *a* equivalent is the **upper limit** for the lowest state oscillator strength in CP29. The suggested lowest-state SDF parameters are reported in Table 5.3. Note that they differ significantly from those reported earlier [84]. Within the framework outlined in [73], not only the action spectra, but also the non-resonantly burned spectral holes (here and in [52]) and the fluorescence spectra actually contain two (or more) contributions: one from the pigments which are, on average, the lowest-energy pigments in the complex (pigment 1) and other from the pigment(s) which is (are) on average, second-lowest, third-lowest, etc in energy (pigment 2, 3, etc) but happen to be lowest-energy due to disorder. The differences in the shape of high-dose and low-dose action spectra, and of non-resonantly burned holes can then be attributed to the differences in SHB efficiencies $\sigma\phi L(\omega_B)$ between different chlorophyll molecules in the complex. Allowing for two (or more) different contributions to the fluorescence origin easily explains the wavelength dependence of the electron-phonon coupling reported in FLN experiments [84]. With that in mind, we utilize the longer-wavelength S value of 0.6 [85] as initial guess in subsequent HGK simulations for the longest burn wavelength where pigment 1 dominates. Comparing our results with those by [86] et al we suggest that fluorescence lifetimes for pigment 1 and pigment 2 in CP29 are 4.8 and 2.6 ns, respectively, and use these numbers as τ_1 (Section 2.5) in subsequent simulations.

5.2.2.3 The hole growth kinetics of CP29 of spinach

To fit the HGK of CP29 a set of parameters has been selected from published works [80, 85, 83]. Thus, the homogeneous width at low temperature (5K) for CP29 is

0.04 cm^{-1} [80], the electron-phonon coupling parameter is S= 0.6 [85] and lifetime of the lowest state was assumed to be 4.8 ns [83]. One should note, however, that changes in the parameters of the lowest-state SDF proposed in the previous subsection must result in some changes of the parameters of the electron-phonon coupling in order to produce the same delta-FLN spectra [85].

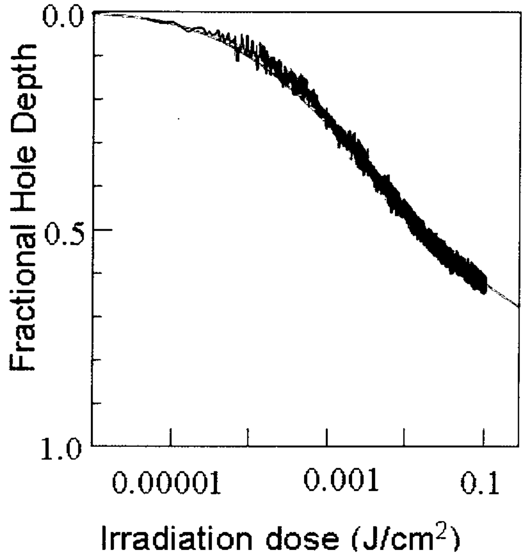

Fig. 5.14 The experimental HGK curves and the best fit to HGK of CP29 for burn wavelength of 681.7 nm

The figure above shows the experimental HGK curves and the best fit to HGK for burn wavelength of 681.7 nm. Some remarks about the parameters of fitting should be made. The theoretical HGK is faster than observed at shorter wavelength for the same tunneling distribution parameters. The electron-phonon coupling in CP29 is wavelength dependent with *S* decreasing towards the shorter wavelengths [85]. Thus, one would expect experimental HGK becoming somewhat faster, not somewhat slower (as observed) towards shorter wavelengths, if the only state being burned at shorter wavelengths was the same as was burned at 681.7 nm. The opposite tendency means that burning at 680.5 and especially 679.0 nm simultaneously probes two different states /

pigments, with the shorter-energy one exhibiting lower SHB yield than the state dominating absorption at 681.7 nm. Fitting the HGK curves at shorter wavelengths requires using two bands for simulations rather than one. The electron-phonon coupling strength of S=0.4 [85] has been used for the second-lowest energy band. In this case reasonable (but not perfect) fit to the higher-energy HGK curves was achieved for $\lambda_{0,2} \sim 10.5$. This corresponds to HB rate for the second state being approximately 1/6 of that for the first state, in reasonable agreement with estimates made above based on action spectrum shape alone (1/3 to 1/10).

5.2.3. LHCII

5.2.3.1 Sample preparation – LHCII of *Pisum Sativum*

LHCII isolation and purification has been performed by the group of Nathan Nelson at Tel-Aviv University, Israel. Isolation of thylakoid membranes from 12-day-old pea (*Pisum Sativum*) was performed based on the previously described method in ref. [83]. The material resulted from the first centrifuge procedure was suspended using a glass-Teflon homogenizer in a buffer (0.3 M sucrose, 20 mM Tricine (pH 8) and 1 mM phenylmethyl-sulphonyl fluoride (PMSF) at a chlorophyll concentration of 3.0 mg chl/ml) and then solubilized by 6.0 mg DM per mg chl. A second centrifugation was applied to remove the unsolubilized material. The resulted material was washed with 25 ml of the same buffer. The eluded LCHII was further centrifuged to separate it into trimeric and monomeric complexes. The last centrifuge procedure provided highly purified trimer and monomer complexes. All procedures were performed in dim light at 4-6 C°. Concentrated samples were diluted with buffer prior to experiment.

5.2.3.2 The absorption and SHB action spectra of LHCII of *Pisum Sativum*

The absorption spectra of LHCII monomer and trimer are presented in Fig. 5.15. The absorption spectrum of LHCII-monomer displays the Q_y peak characteristic to chlorophyll a at 675.86 nm. The Q_y absorption band of LHCII trimer displays characteristic peak for chlorophyll a at 675.46 nm and one can note two weak shoulders at 671.08 nm and 661.54 nm. Similar absorption peaks have been reported in published papers [87-90] despite LHCII complexes explored here belonging to different plants, pea and spinach, respectively, and despite the fact that our LHCII is associated with Photosystem I rather than Photosystem II. Still, some differences do exist i.e. the shoulder at ~671 nm is not as well-resolved in case of the pea.

A comparison between the absorption features of LHCII spectrum reported in this work and in earlier reported [87-90] is presented in Table 5.2.

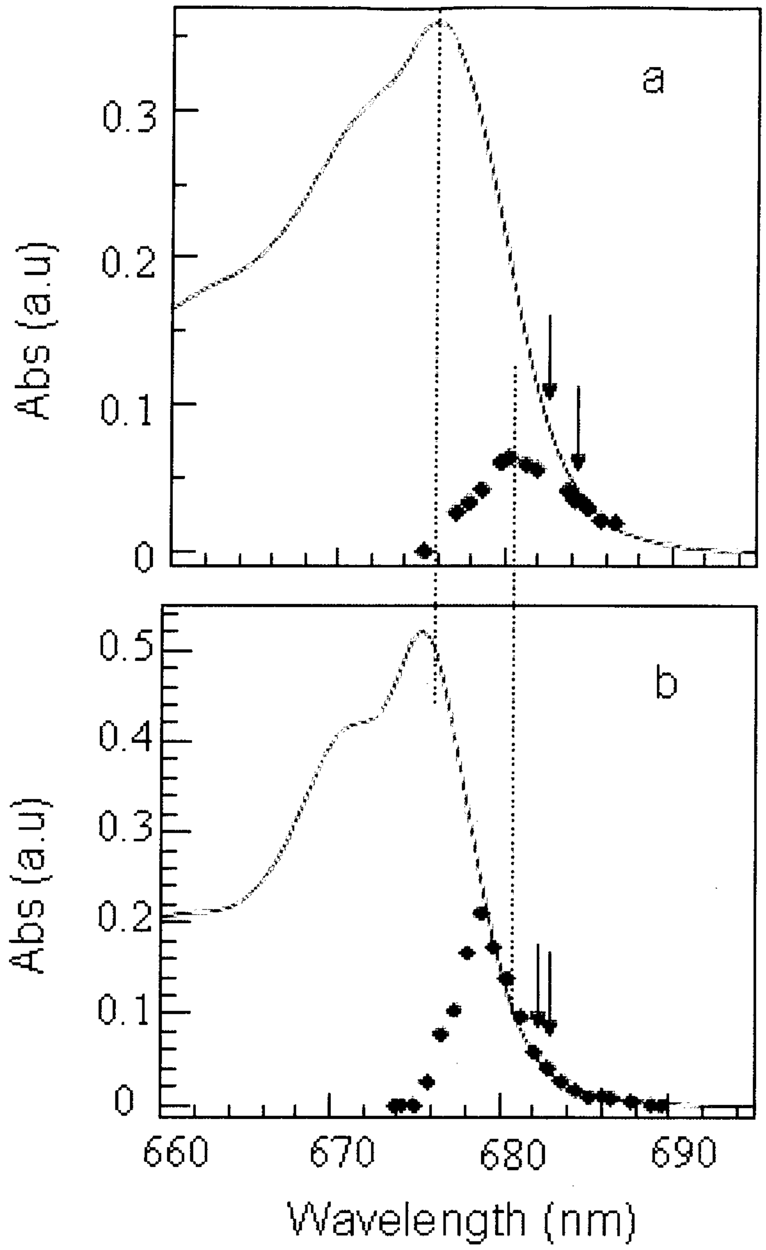

Fig. 5.15. Absorption (red curves) and HB action spectra (diamond curves) of LHCII-monomer (a) and LHCII-trimer (b)

Table 5.2 Absorption features of LHCII

	Experimental results		Literature results				
Pigment	**LHCII-monomer**	**LHCII-trimer**	**LHCII-monomer**		**LHCII-trimer**		**Aggregated LHCII-trimer 4.2K**
			77K	**4.5K**	**77K**	**4.5K**	
Chl a	675.86 nm	675.46 nm 671.08 nm 661.54 nm	662 nm; [34, 87] 670 nm; [34, 87] 678 nm; [34, 87]	676 nm [88] 671 nm [88] 661.5 nm [88]	670 nm; [34, 87] 676 nm; [34, 87]	676 nm [88] 671 nm [88] 661.5 nm[88]	676.3 nm[89] 671.9 nm [89] 662.0 nm[89]

One should note that, as mentioned above, an important difference between LHCII employed in this work and earlier ones is that LHCII associated with Photosystem I rather than Photosystem II is explored in this work. Thus, the sample used in these experiments is supposed to have a relative enrichment in Lhcb2 protein and contain a negligible amount of Lhcb3 protein [91-94]. The Lhcb2 protein is exhibiting the most blue-shifted lowest-energy state among the Lhcb1-3 proteins while the Lhcb3 protein normally comprising about 10% of LHCII samples (6:2:1 Lhcb1:Lhcb2:Lhcb3; [92]) is known to exhibit the most red-shifted lowest state at room temperature. Despite these differences, qualitatively, all the tendencies observed earlier for LHCII from spinach are present in the case of pea: the spectrum of the monomer is somewhat less structured, slightly red-shifted and with stronger lowest-energy region absorption.

The monomer's SHB action spectrum Fig.5.15 (a) – diamonds), obtained with irradiation dose of 0.0018 J/cm^2 (low-dose) is somewhat asymmetrical and is peaked at 680.2 nm, slightly to the red compared to 679.6 nm recently reported in ref. 88 for spinach monomer at slightly higher dose of 0.003 J/cm^2. The FWHM of this action spectrum reported in this research is ~120 cm^{-1}. Note that since action spectrum is asymmetrical, we report the true FWHM value, not the result of a Gaussian fit. Comparing the absorption and action spectra displayed in Fig 5.15 (a) one can notice that burning at wavelengths longer than 684 nm would guarantee that only the lowest-energy state is probed.

To determine the parameters of the SDF of the lowest-energy (on average) pigment (oscillator strength) an approach similar to that presented in previous sections (for CP29 and CP43) in used in the case of LHCII. In Fig. 5.16 all three lowest states of LHCII monomer have oscillator strength equal to 1.2 Chl *a* molecules. In order to achieve a good fit, one has to assume that the hole burning efficiency of the pigment 2 is several times lower than for pigment 1, while that of pigment 3 is only slightly lower. Obviously, reasonable fits to action spectrum can be obtained for certain range of SDF parameters. Again, like in the case of CP29, the purpose of the fitting of action spectrum is not only the determination of the SDF parameters, but also of the range of reasonable oscillator strengths of the lowest-energy state(s). All employed parameters are summarized in Table 5.3. The 4.4 ns lifetime of the lowest state [95] is used for both monomeric and trimeric LHCII.

It is obvious that the SHB action spectrum for LHCII trimer shown in Fig.5.15 (b) is narrower than for monomer. It maximum is located at 678.9 nm and it has the FWHM of 90 cm^{-1}. This could be compared to the data for spinach LHCII trimer from ref. 89. The Gaussian fit to the high-dose HB action spectrum has its maximum located at 678.2 nm and it has a width of 85 cm^{-1}. In the ref. [95] has been reported the HB action spectrum peaked at 679.3 nm and with the width of 110 cm^{-1}. Interestingly, much larger fraction of the absorption spectrum can be fitted to the low-dose action spectrum in the case of the LHCII trimer than in the case of the monomer. It is also much more obvious than in the case of the monomer that the action spectrum of the trimeric LHCII contains two different components, much like that of CP43.

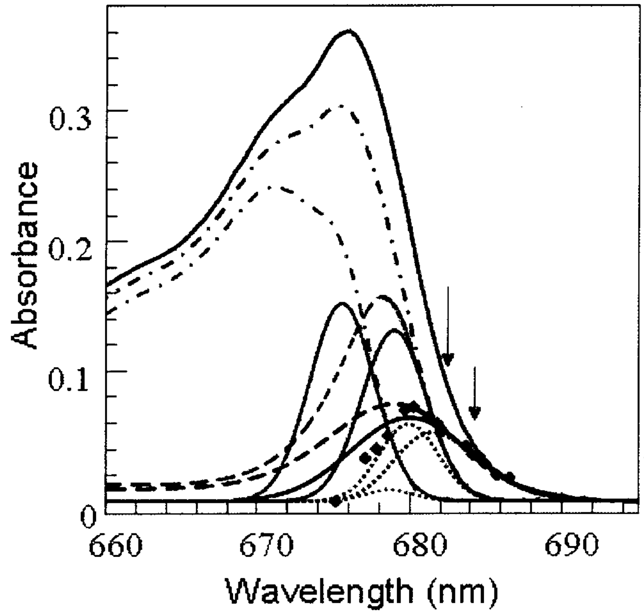

Fig. 5.16 The SDF and the absorption spectrum of the lowest – energy state of LHCII monomer; where the dashed blue curve is the pigment 1 SDF corrected with phonons and localized vibrations contribution; dash-dotted red curve is the difference between the whole absorption spectrum (solid red curve) and the lowest-state absorption (dashed blue curve); black and green solid curves are the second and third-lowest energy SDFs; dashed black curve is the absorption spectrum of pigment 2 dressed with phonon and vibration contributions; black dotted curve is SDF of pigment 2 molecules incapable of downhill EET

In case of the **trimeric LHCII** different approaches are possible within the framework of [73], depending on the rate of energy transfer between the lowest-energy pigments of adjacent monomers. The SDF of these three lowest-energy states are peaked at 679.8, 678.4 and 677.1 nm and have the widths of 70 cm^{-1} according to [96]. The rate of respective energy transfer was not determined. In ref. 96 it has been assumed that the high-dose HB action spectrum is the sum of these SDF but not only the lowest-energy band alone. This implies that energy transfer between adjacent monomers is relatively slow. The irradiation dose dependence of the position of the broad non-resonantly burned hole indicates that SHB yield is varying between the lowest-energy states of the three monomers, suggesting some inter-monomer energy transfer is lowering the SHB yield for two of the pigments. Although in the light of this analysis such effect can be assigned to the onset of burning of the second-lowest pigments of the monomers, the dose dependence of the non-resonant hole is much weaker, if present at all, for LHCII monomers [89]. It has also been argued that only the lowest one of the three low-energy sub-bands of the trimer is the origin of fluorescence. On the other hand, three narrow lines per single LHCII trimer, with approximately equal intensities, have been reported in single complex emission spectra [83, 97], indicating the absence of inter-monomer EET. One should note that effective inter-monomer EET should suppress the action spectrum, ultimately bringing its integral intensity down to a value corresponding to one Chl *a* per LHCII trimer, i.e. per 42 chlorophylls (or slightly more for a delocalized excitonic state). A quick look at Fig. 5.15 (b) and Fig. 5.17 allows noticing that this is not the case. Thus, the effects of inter-monomer EET will be ignored in subsequent discussion. It is assumed that errors resulting from the possibility of such EET are smaller than those resulting, for example, from the differences in the lowest-state parameters of Lhcb1 and Lhcb2 proteins comprising the sample. In other words this assumption means that the differences in the spectral properties of monomeric and trimeric LHCII complexes are ascribed to the small changes in the overall protein structure of the LHCII monomers upon monomerization, not to the changes in interactions between Chlorophylls *a* belonging to the adjacent monomers.

An example of deconvolution of the low-energy region of the spectrum using three states is presented in Figure 5.17. All states have oscillator strengths of 1.2 Chl *a* equivalents, and the lowest state SDF has been made broad enough to fit the low-energy tail of the absorption spectrum. Again, the HB action spectrum has to be fitted with a weighted sum of the dotted curves. Clearly, a satisfactory fit to the action spectrum can be obtained with HB yields for either second or third states being larger than for the lowest-energy one. This result is different from that obtained for CP29 and LHCII monomer. Lowest-state parameters can be found in Table 5.3.

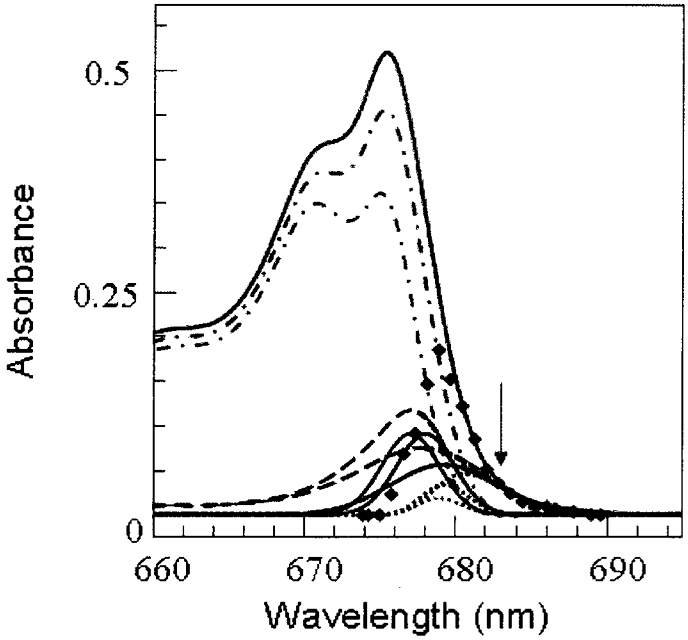

Fig. 5.17 The SDF and the absorption spectrum of the lowest – energy state of LHCII trimer; where the dashed blue curve is the pigment 1 SDF corrected with phonons and localized vibrations contribution; dash-dotted red curve is the difference between the whole absorption spectrum (solid red curve) and the lowest-state absorption (dashed blue curve); black and green solid curves are the second and third-lowest energy SDFs; dashed black curve is the absorption spectrum of pigment 2 dressed with phonon and vibration contributions; black dotted curve is SDF of pigment 2 molecules incapable of downhill EET

4.2.3.3. The hole growth kinetics of LHCII of *Pisum Sativum*

The experimental HGK curve, the best fit to HGK and the spectral hole burned at 684.2 nm are presented in Figure 5.18a for monomeric LHCII. The hole has the width of about 0.1 cm^{-1} and the fractional hole depth of about 15% for an irradiation dose of ~$2 \cdot 10^{-3}$ J/ cm^2 at λ_B = 682.6 nm. Figure 5.18b contains experimental HGK curve and its fit for trimeric LHCII (λ_B =683.1 nm) As it has been reported in Ref. 83, the 10 K fluorescence decay kinetics of LHCII has two components, 1.8 and 4.4 ns. In this work the latter value has been used to simulate the lowest-energy HGK curves for both monomer and trimer. The parameters that have been used to fit monomer's HGK include homogeneous line width of 0.04 cm^{-1} [80] and electron – phonon coupling parameters of 0.9 [88] for initial guess. However, due to the changes in the SDF parameters proposed above, the actual phonon sideband shape may differ somewhat from that proposed in [88].

Moreover, as can bee seen from HGK curves for both monomeric and trimeric LHCII, the maximal fractional hole depth (~45% for monomer and ~35% for trimer) is significantly smaller than expected for S=0.6 (monomer) and S=0.8–0.9 (trimer) reported in [88, 86, 95-98]. The fits to HGK obtained with the initial guess values of S were relatively poor, and resulted in λ_0>12 for lowest-energy bands of both trimeric and monomeric LHCII. It was also clear that in order to simulate the early leveling off of the kinetics at high irradiation doses one had to introduce high values of $\sigma_\lambda > 2$, which, in turn resulted in poorer fits to the beginning of the spectra. Therefore, we allowed S to increase significantly for both monomeric and trimeric LHCII. Simultaneously, we decreased the width of the Lorentzian part of the PSB somewhat to arrive to approximately the same simulated overall shape of the Δ-FLN spectra as reported in [88].

One should also note that producing acceptable fits also for shorter burn wavelength holes (not depicted) required that the second-lowest state (with parameter different from those for the first state) contributes significantly to absorption already at 682 nm (monomer) and 681 nm (trimer), respectively. This in turn places limitations on the oscillator strength of the lowest-energy state.

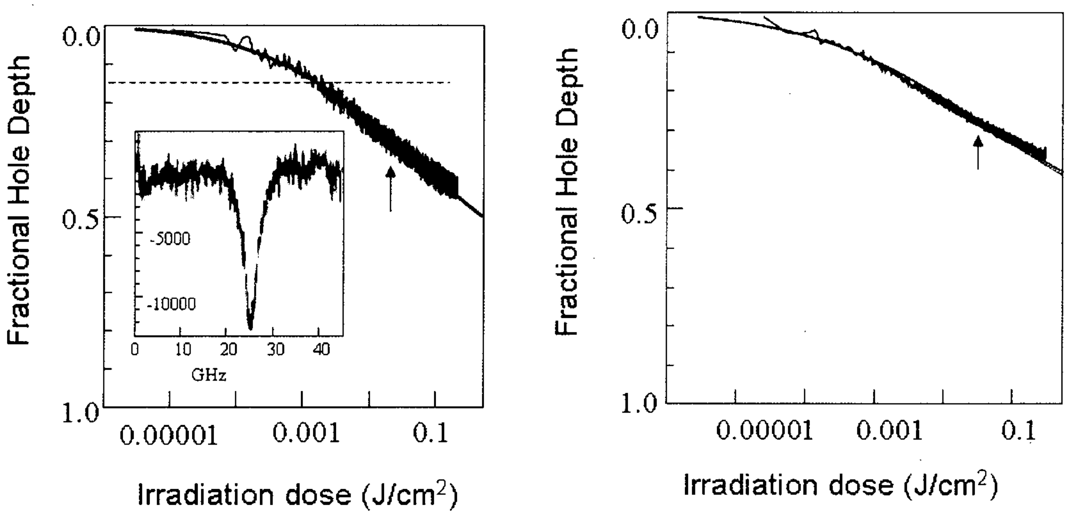

(a) (b)

Fig. 5.18 The experimental HGK curves for LHCII – monomer (a) and trimer (b) and the best fit to HGK for burn wavelength of 684.2 nm and 683.1 nm respectively; the insert shows the spectral hole burned at 684.2 nm

The Fig. 5.18 (a) and (b) have been obtained assuming that the oscillator strength of the two lower-energy states of both the monomeric and trimeric LHCII does not exceed 1.2 Chl *a* equivalents, in agreement with super-radiance data [100]. Again, fit parameters are summarized in Table 5.3.

Table 5.3 The summary of the HGK curves simulation parameters Fit parameters correspond to the lowest burn frequency, highlighted in bold

Complex	**CP43, A-state**	**CP29**	**LHCII monomer**	**LHCII trimer**
SDF peak and width (cm^{-1})	14641; 180	14717, 165 [1]	14705; 198 [2]	14717, 180 [3]
Oscillator strength (Chl *a* equivalents)	1	1.0-0.7	1.2	1.2
Lifetime τ_1 (ns)	3.5	4.8	4.4	4.4
Γ_{homog} (cm^{-1})	0.03	0.04	0.04	0.04
Burn frequency ω_B (cm^{-1})	**14560**	**14670** 14694 14720	**14616,** 14628, 14653	**14640** 14652 14656
S_{PSB}	0.30±0.05	0.60±0.05	0.80±0.05[4]	1.3±0.1
ω_m; Γ_{Gauss}; $\Gamma_{Lorentz}$ (cm^{-1})	17; 15; 70	22; 20; 110	22; 20; 110[4]	22,20,110
λ_0	11.0±0.2	9.6±0.2	11.3±0.2[4]	11.2±0.2
σ_λ	1.0±0.05	1.4±0.2	2.0±0.2	2.3±0.2

[1] SDF parameters from [79]: peak 14745 cm^{-1}, FWHM=120 cm^{-1}, S=0.4…0.6.

[2] SDF parameters from [88]: peak 14715 cm^{-1}, FWHM=110 cm^{-1}, S=0.6

[3] SDF parameters from [88]: peak 14705 cm^{-1}, FWHM=80 cm^{-1}; S=0.8…0.9

[4] The best fit with electron-phonon coupling parameters exactly as in [88] yields λ_0=12.0

5.3. Discussion

Concerning the HGK curves simulation parameters (table 5.3) the key observation is that the parameters of the tunneling distribution observed for photosynthetic protein complexes are significantly different from those reported for hyperquenched glassy water and simple organic glasses [35, 56, 97]. The LH2 antenna complex, which was explored in detail earlier [previous section and Ref. 38] and which contains bacteriochlorophyll *a*, not chlorophyll a, exhibited parameters in the same range (λ_0=10.3±0.2, σ_λ=0.7±0.1). Generally it can be noticed that the hole burning yield is 30–100 times lower in protein complexes than in water and organic glasses. This is reasonable and it is due to tunneling entities in proteins being larger and heavier than in the amorphous host. In all cases (LH2 and Chl *a* antenna complexes) we did not observe any evidence for fast spectral diffusion. The latter is associated with TLS of the amorphous host surrounding the pigment-protein complexes or with surface TLS. There was no accumulation of anti-hole absorption in the immediate vicinity of the resonant hole , which could be expected if majority of molecules were capable of experiencing small, <1 cm^{-1} shifts upon burning [45, 70, 64]. Summarizing, our data reflects the true dynamics of the intact protein and not the interface or surrounding amorphous host dynamics.

It is obvious that the differences in protein dynamics parameters reflect the differences in the protein environment of the respective chlorophyll molecules. In this respect it is instructive to note that these parameters are the same, within experimental errors, for the lowest-energy state of monomeric and trimeric LHCII. This indicates that the lowest-energy state of this complex most likely is not significantly affected by monomerization of LHCII. A very interesting observation is that the protein dynamics of the lowest-energy state of CP29 is significantly different from that of the LHCII. This suggests that either the lowest state is localized on completely different chlorophylls in CP29 and LHCII, or that the excitonic lowest state of LHCII is significantly contributed to by a chlorophyll molecule either absent in CP29, or present but in significantly different environment. In this respect it is worthwhile to recall the results of the recent excitonic calculations performed based on the high-resolution structure of LHCII (the structure for CP29 is not available, but similarities are expected based on genetics).

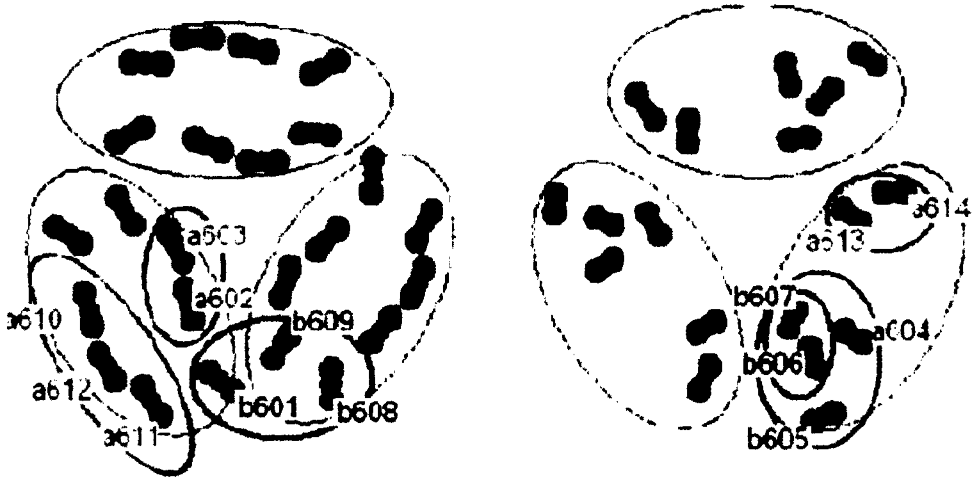

Fig. 5.19 The structural arrangement of chlorophylls in LHCII (after ref. 27)

In the Fig. 5.19 the structural arrangement of chlorophylls in LHCII is shown. Several groups [101-103] reported the results of modeling, including that of not only absorption, LD and fluorescence spectra, but also of various 1D and 2D time-domain data. It has been concluded that Chl 604, proposed by Pieper et al. [88] to be the lowest-energy pigment in the complex, is required to absorb at much higher energy. Lowest-energy state was placed on Chls 610, 611 and 612. Thus, it seems reasonable that the lowest-energy state probed by SHB is localized predominantly on Chls 610, 611 and 612, with subsequent states on 602-603 and 613-614 dimers. Assignment of the lowest state to the 610-611-612 trimer is also in agreement with the assumption of negligible EET between the lowest-energy states of the adjacent monomers which we made above, as these pigments are situated far from the similar chlorophylls in the adjacent monomers. Note that Chl 611 is absent in CP29 [27, 104, 105]. As the dynamics of the second-lowest state of LHCII is significantly affected by monomerization, one could speculate that this state is localized on Chls 613 and 614 which are the closest to the interface between the monomers in the trimer. It cannot be completely excluded that this state is localized on Chls 602 and 603 but it is less probable. The Chls 602 and 603 of adjacent monomers are close to each other according to the trimer structure (Fig. 5.19), and energy transfer between chlorophylls 602 and 603 belonging to adjacent monomers would suppress burning into the second lowest state of the trimer with respect to the monomer. In reality, however, the second-lowest state contributes more to the action spectrum of the trimer than to the action spectrum of the monomer.

Finally, we address the electron-phonon coupling parameters following from this work and their disagreement with Δ-FLN data from [88]. Use of the parameters derived from Δ-FLN data [84, 88] results in poor fits to the hole growth kinetics curves. This discrepancy can be attributed either to our assumption about the absence of weak aggregation-related bands in the low-energy edge of the spectra being invalid (i.e. to our lowest-state SDF parameters being incorrect), or to our SHB model applied being inapplicable to proteins in general, or just to the differences between the species. However, an interesting alternative explanation also exists, namely, that the Δ-FLN data fittings in Refs 21, 22 are subject to a systematic error. One could notice, for example, that the equation used to simulate the Δ-FLN spectra in [84, 88] is valid only in the shallow hole limit, while the data which was fitted with that equation corresponds to ~30%-deep holes. The latter estimate can be obtained after throwing just a brief look at the Figure 2C of [85] and 7A and 8A of [88]. Also, the irradiation doses reported in ref. 85 and ref. 88 (32 mJ/cm^2) must result in ~30%-deep holes according to the data presented in this work (upward arrows in Fig. 5.18 (a) and 5.18 (b)). The anti-hole absorption, which is distributed both to the red and to the blue with respect to the excitation wavelength, also was not taken into account in [85, 88]. In order to explore how using more accurate treatment would affect the Δ-FLN spectra, we modified the existing software based on Equation 1 to allow for calculation of Δ-FLN spectra for a broad range of irradiation doses, as well as in the presence of NPHB anti-hole. The modification was very straightforward: SDF modified by burn (see Chapter 4)

$$(G(\omega)\cdot \exp(-Pt\sigma\phi L(\omega-\omega_B)\cos^2\alpha) + \text{normalized anti-hole})$$

was convoluted with the single-site emission spectrum. The latter is just the single site absorption spectrum flipped with respect to the ZPL. Strictly speaking, such a procedure results in Δ-FLN spectra being conservative, which is obviously in contradiction with all published results. Thus, before convoluting SDF modified by burn as in equation above with the single-site emission spectrum one has to remove from that modified SDF the part of the anti-hole which is blue-shifted with respect to the excitation energy. Such a removal is physically justified, as molecules to the blue of the ZPH are not excited and do not contribute to the Δ-FLN spectra. Within the frame of this model, the electron-phonon coupling parameters presented in Table 5.3 result in even better agreement with Δ-FLN spectra from ref. 88 than the theoretical data from work [29] itself. For example, the broad bump several nm to the red of the burn wavelength is reproduced by our fits and missed by the fits from [88]. One should note, however, that the fits to hole growth kinetics data, especially for LHCII trimer, can be further improved if one allows for even narrower phonon sidebands. In Fig. 5.18 (b), blue curve, obtained for the 90 cm^{-1} FWHM of the Lorentzian contribution to phonon sideband, offers somewhat better fit to the experimental data than the red curve (Lorentzian FWHM of 110 cm^{-1}). Detailed theoretical study of Δ-FLN spectra, for all irradiation doses and including NPHB anti-hole contributions, is the subject of future papers.

6. CONCLUSIONS

Low-temperature protein dynamics has been explored for the lowest-energy pigments of several photosynthetic protein complexes (CP43, CP29 and LHCII) as well as for the B800 band of LH2 by means of high resolution hole burning spectroscopy. In particular, spectral hole growth kinetics has been measured and analyzed. It has been demonstrated that hole-burning yields are significantly lower in photosynthetic proteins than those in simple molecular glasses. This is consistent with the idea that the tunneling entities are much larger and heavier in protein.

We found no evidence for fast small spectral shifts routinely observed in SMS experiments. The agreement between SHB and SMS data for other tiers of LH2 dynamics is good though. Support has been provided for the theories of B800-B850 energy transfer involving the whole B850 density of states.

The parameters of tunneling distribution obtained in this work for a number of complexes can be employed for disentangling the effects of this distribution and of the distribution of energy transfer rates in the hole burning data obtained from higher-energy states.

We also assigned the lowest-energy states of LHCII complex to particular chlorophylls known from structure data. The lowest-energy state of LHCII, in both trimeric and monomeric form, was assigned to excitonically coupled Chls 610, 611 and 612. It is unclear however, if Chls 610 and 612 are responsible for the lowest state of CP29, as protein dynamics of the lowest state of CP29 differs significantly from that of

LHCII. The second and third lowest states were assigned to Chls 613-614 and/or 602/603, respectively.

Finally, the importance of developing more detailed procedures for modeling Δ-FLN data has been demonstrated as this will allow for obtaining more precise values of electron-phonon coupling parameters.

Appendix 1. Preliminary results on Photosystem I from *Synechocystis PCC6803* and *Thermosynechococcus elongatus.*

The research on protein energy landscapes can be extended also to other systems, for example cyanobacterial Photosystem I. PS I is one of the two major photosystems involved in oxygenic photosynthesis and the largest and most complex membrane protein for which detailed structural and functional information is now available [106, 107]. The main function of PS I is to capture and convert light energy into chemical energy by transferring electrons through the photosynthetic (thylakoid) membrane from plastocyanine or cytochrome c6 to NADP+ [106, 107]. A pair of closely-spaced Chl *a* molecules called P700 (and allegedly absorbing at 700 nm) serves as a primary electron donor in the light-induced charge separation process. There is significant degree of similarity between the structures of PS I and PS II, but most of the antenna of PS I is connected to just two proteins, PsaA and PsaB proteins, and therefore PS I cannot be taken apart into various relatively small antenna complexes as PS II.

Cyanobacterial Photosystem I can exist in the photosynthetic membrane in both trimeric and monomeric forms and it captures the sunlight by the large antenna system that consists of >90 antenna chlorophylls and 22 carotenoids [106].

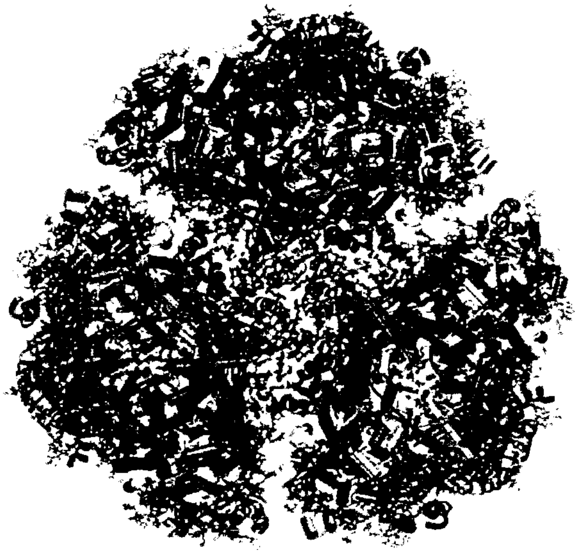

(a)

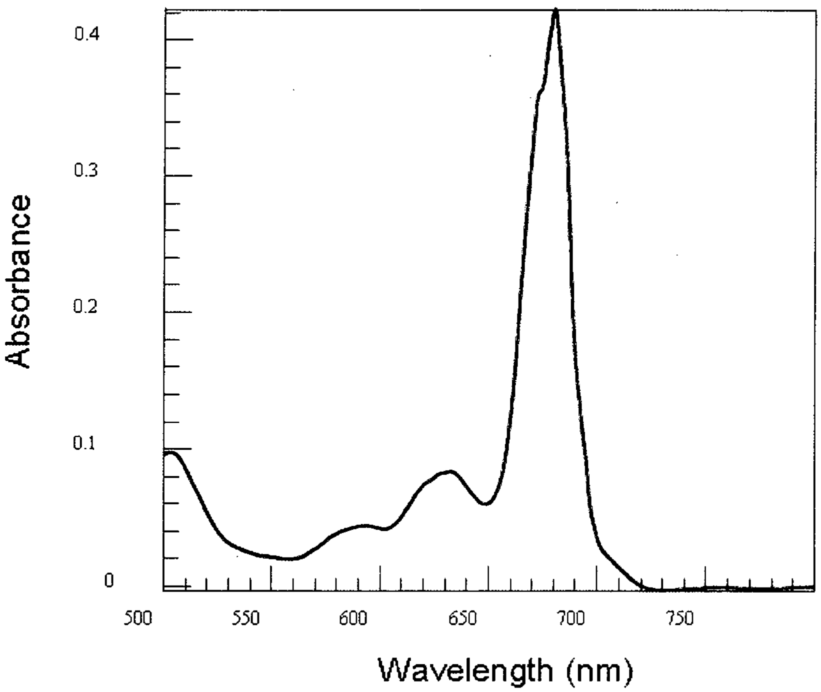

(b)

Fig. A1.1 The structural model of Photosystem I and the absorption spectrum of PS-I wild type (a -from ref. 106, b - from our group data). Green – chlorophyll molecules, blue, pink, purple, orange, etc – protein alpha-helixes.

In case of this complicated system containing ~100 chlorophylls per monomer, connected by energy transfer, one can utilize another method of exploring the barrier parameters distributions – the recovery of the satellite hole structure resulting from HB following energy transfer (Figures A.1.1 and A.1.2.). As can be seen, different satellite holes recover at different temperatures. Analysis of this data is in progress.

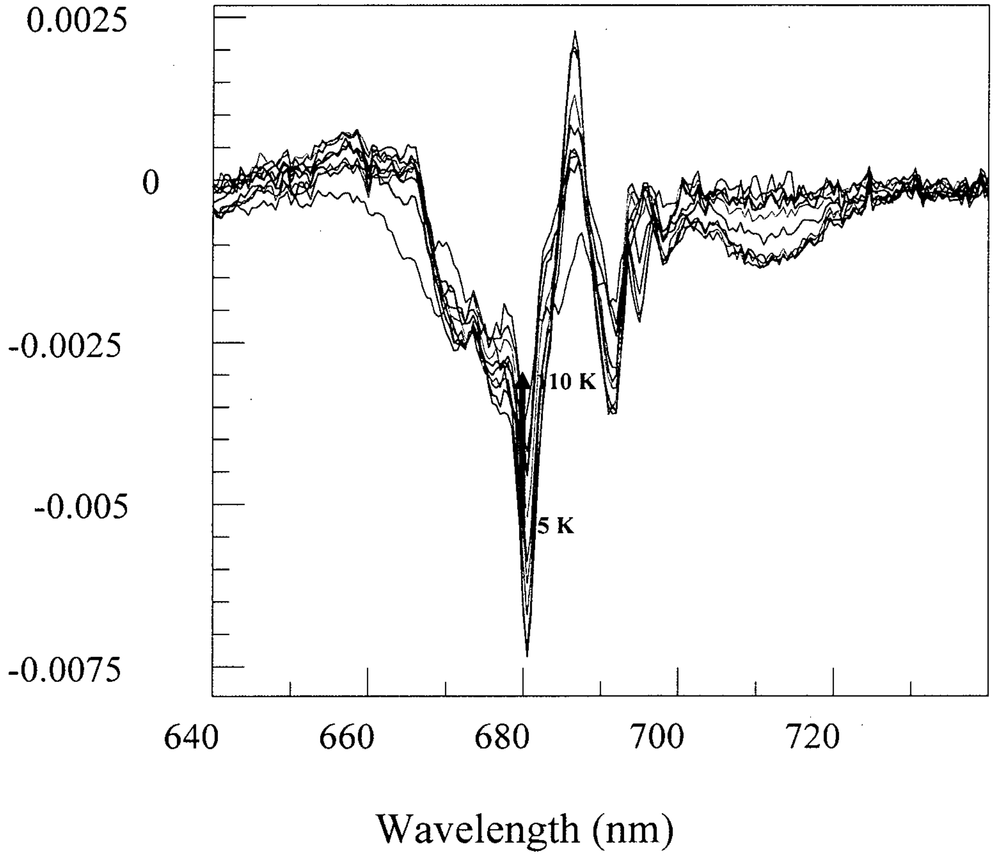

Fig. A1.2 Thermocycled spectral holes burned in to the absorption spectrum of Synechocystis PCC6803 at 660 nm (T=5K, 20K, 31K, 40K, 52K, 61K, 73K, 86K, 99K, 110K). The lowest-temperature spectrum is the deepest hole spectrum. The vertical line indicates the burn wavelength.

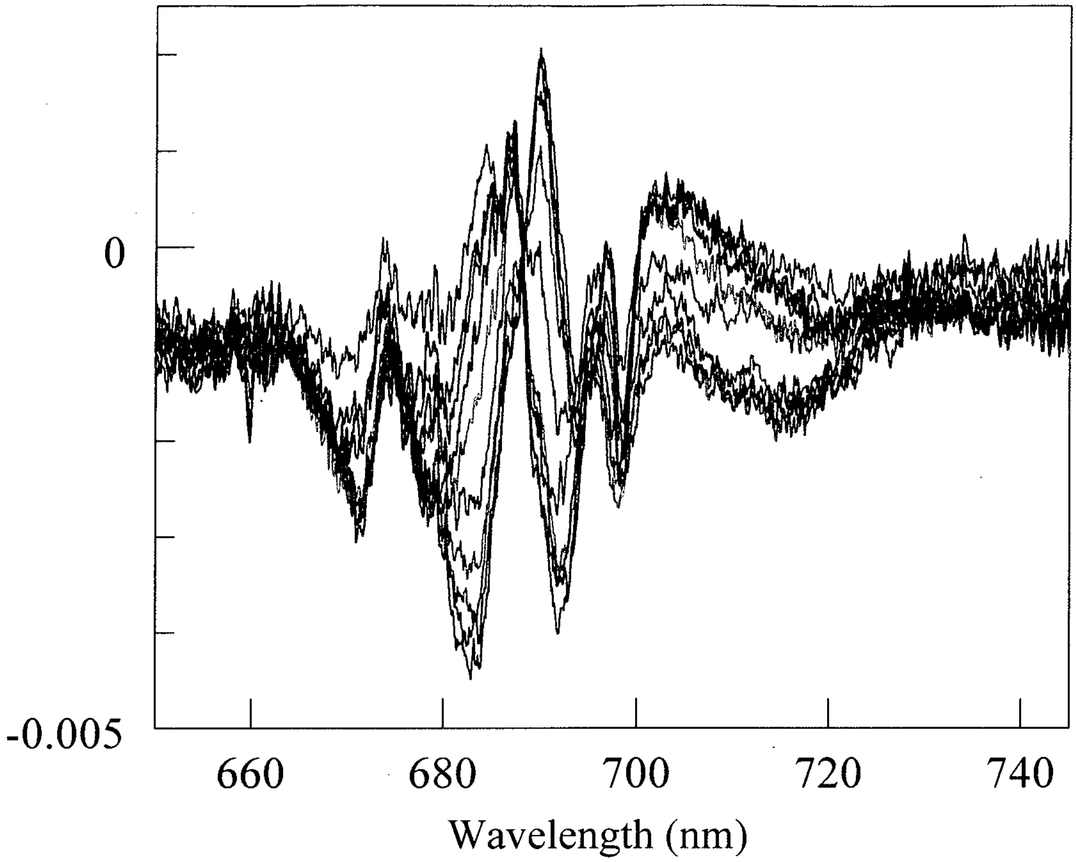

Fig. A1.3 Thermocycled spectral holes burned in the absorption spectrum of *Thermosynechococcus Elongatus* at 659.94 nm (T=5K, 19.5K, 30K, 40K, 50K, 69.4K, 85.1K, 100K, 119K, 146K). The lowest-temperature spectrum is the deepest hole spectrum

Appendix II.

Table A2: Summary of the experiments performed

Species	*Rps. Acidophila*
Complex studied	**LH2**
Provider/collaborator	Cogdell, U. Glasgow
Experiment type	HB Spectra, hole broadening on a time scale of hours and HGK
Species	*Spinach*
Complex studied	**CP43**
Provider/collaborator	Seibert and Picorel, NREL, Colorado
Experiment type	HB Spectra and HGK
Species	*Spinach*
Complex studied	**CP29**
Provider/collaborator	Pieper and Irrgang, Berlin
Experiment type	HB Spectra and HGK
Species	*Pea*
Complex studied	**LHC-II**
Provider/collaborator	Nethan Nelson, U. Tel Aviv, Israel
Experiment type	HB Spectra and HGK
Species	*Synechocystis PCC6803* and *Synechococcus elongatus*
Complex studied	**PS I**
Provider/collaborator	T.W. Johnson / Petra Fromme ASU
Experiment type	Thermocycling of the whole satellite hole structure.

REFERENCES

1. R. E. Blankenship, Molecular Mechanisms of Photosynthesis, Blackwell Science Oxford, UK, 2002

2. Advances in Photosynthesis and Respiration, vol. 20, Discoveries in Photosynthesis, Ed. By Govindjee, J. T. Beatty, H. Best, J. F. Allen, Springer 2005

3. Advances in Photosynthesis and Respiration, vol. 4, Photosynthesis: The Light Reactions, Ed. By D. R. Ort, C. F. Yocum, I. F. Heichel, Kluwer Academic Publishers, 1996

4. R. J. Cogdell, J. Gordon Lindsay, The structure of photosynthetic complexes in bacteria and plants: an illustration of the importance of protein structure to the future development of plant science, TANSLEY, New Phytol, 145, 167-196, 2000

5. K. J. Riley, Probing the energy-transfer dynamics of photosynthetic reaction center complexes through hole-burning and single-complex spectroscopy, PhD Thesis, Iowa State University, 2007

6. R. Purchase, S. Volker, Spectral hole burning: examples from photosynthesis, Photosynth Res 101:245–266, 2009

7. H. van Amerongen, L. Valkunas, R.van Grondelle, Photosynthetic Excitons, World Scientific, ISBN 981-02-3280-2, 2000

8. J. Friedrich, D. Haarer Photochemical Hole Burning: A Spectroscopic Study of Relaxation Processes in Polymers and Glasses, Angew. Chem. Int. Ed. Engl. 23, 113-140, 1984

9. J. Friedrich, Hole Burning Spectroscopy and Physics of Proteins, Methods in Enzimology, 246, 226 – 259, 1995

10. S. Volker, Hole-Burning Spectroscopy, Annu. Rev. Phys. Chern. 40, 499-530, 1989

11. B. H. McMahon J. D. Muller, C. A. Wraight, G.U. Nienhaus, Electron Transfer and Protein Dynamics in the Photosynthetic Reaction Center, Biophysical Journal, Vol. 74, 2567–2587, 1998

12. T. Reinot, V. Zazubovich, J. M. Hayes, G. J. Small, New Insights on Persistent Nonphotochemical Hole Burning and Its Application to Photosynthetic Complexes, J. Phys. Chem. B, 105, 5083-5098, 2001

13. D. L. Andrews, A. A. Demidov, An introduction to Laser Spectroscopy, Kluwer Academic/Plenum Publishers, 2002;

14. J. M. Hollas, Modern Spectroscopy, 4th Edition, 2009;

15. W. W. Parson, Modern Optical Spectroscopy, Springer ISBN 978-3-540-95895-6, Second Edition, 2009

16. Valter Zazubovich, Course Notes, Optical Spectroscopy, PHYS679B, 2009

17. J. Kohler, A.M. van Oijen, M. Ketelaars, C. Hofmann, M. Matsushita, T.J. Aartsma, J. Schmidt, Optical Spectroscopy of Individual Photosynthetic Pigment Protein Complexes, Intl.J.Modern Phys.B, vol.15, Nos. 28-30, 3633-3636, 2001

18. A. M. van Oijen, M. Ketelaars, J. Ko1hler, T. J. Aartsma, J. Schmidt, Spectroscopy of Single Light-Harvesting Complexes from Purple Photosynthetic Bacteria at 1.2 K, J. Phys. Chem. B, Vol. 102, No. 47, 1998

19. M-L Groot, R. N. Frese, F. L. de Weerd, K. Bromek, Å. Pettersson, E. J. G. Peterman, Ivo H. M. van Stokkum, R. van Grondelle, J. P. Dekker, Spectroscopic

Properties of the CP43 Core Antenna Protein of Photosystem II, Biophysical Journal Vol. 77, 3328–3340, 1999

20. J. W. Murray, J. Duncan, J. Barber, CP43-like chlorophyll binding proteins: structural and evolutionary implications, TRENDS in Plant Science Vol.11 No.3 March 2006

21. A. Pascal, C. Gradinaru, U. Wacker, E. Peterman, F. Calkoen, K-D Irrgang, P. Horton, G. Renger, R. van Grondelle, B. Robert, H. van Amerongen, Spectroscopic characterization of the spinach Lhcb4 protein (CP29), a minor light-harvesting complex of photosystem II, Eur. J. Biochem. 262, 817-823, FEBS, 1999

22. R. Croce, M. G. Muller, S. Caffarri, R. Bassi, A. R. Holzwarth, Energy Transfer Pathways in the Minor Antenna Complex CP29 of Photosystem II: A Femtosecond Study of Carotenoid to Chlorophyll Transfer on Mutant and WT Complexes, Biophysical Journal, Vol. 84, 2517–2532, 2003

23. F. J. Kleima, C. C. Gradinaru, F. Calkoen, I. H. M. van Stokkum, R. van Grondelle, H. van Amerongen, Energy Transfer in LHCII Monomers at 77K Studied by Sub-Picosecond Transient Absorption Spectroscopy, Biochemistry, 36, 15262-15268, 1997

24. J. Pieper, R. Schodel, K-D Irrgang, J. Voigt, G. Renger, Electron-Phonon Coupling in Solubilized LHC II Complexes of Green Plants Investigated by Line-Narrowing and Temperature-Dependent Fluorescence Spectroscopy, J. Phys. Chem. *B, 105,* 7115-7124, 2001

25. T. Barros, A. Royant, J. Standfuss, A. Dreuw, W. Kuhlbrandt, Crystal structure of plant light-harvesting complex shows the active, energy-transmitting state, The EMBO Journal 28, 298–306, 2009

26. H. van Amerongen, R. van Grondelle, Understanding the Energy Transfer Function of LHCII, the Major Light-Harvesting Complex of Green Plants, J. Phys. Chem. B, 105, 604-617, 2001

27. Z. Liu, H. Yan, K. Wang, T. Kuang, J. Zhang, L. Gui, Xiaomin An, Wenrui Chang, Crystal structure of spinach major lightharvesting complex at 2.72Å resolution, Nature, Vol. 428, www.nature.com , 2004

28. H7421 Series Photon Counting Head, Instruction Manual, 2008

29. Research Cryostat A-240 B, Operation Manual, National Academy of Sciences of Ukraine, Kiev, 2006

30. Matisse User's Guide, Sirah Laser- und Plasmatechnik GmbH, Version 1.6

31. M. Vacha, F. Adamec, M. Ambroz, J. Dian, J. Hala, Spectral Hole Burning of Photosynthetic Antenna of Blue-Green Algae, Czechoslovak Journal of Physics, Vol. 41, No. 7, 606 – 613, 1991

32. R. I. Personov, B. M. Khalamov, Photochemical and Photophysical Hole Burning in Electronic Spectra of Complex Organic Molecules, Laser Chem. Vol. 6, 181-201, 1986

33. H.C. Meijers, D.A. Wiersma, Low temperature dynamics in amorphous solids: a phonon echo study, J. Chem. Phys. 101 (8), 6927 – 6943, 1994

34. M. Bauer, L. Kador, Single-molecule spectra split by the interaction with two-level systems (TLSs), Journal of Luminescence 107, 32-37, 2004

35.T. Reinot, N. C. Dang, G. J. Small, A model for persistent hole burned spectra and hole growth kinetics that includes photoproduct absorption: Application to free base phthalocyanine in hyperquenched glassy ortho-dichlorobenzene at 5 K, J. Chem. Phys. 119 (19), 10404-10414, 2003

36. N.C. Dang, J. M. Hayes, T. Reinot, G.J. Small, Dispersive hole burning kinetics and fluence broadening of the zero-phonon hole of impurities in amorphous hosts, Chem. Phys. 297, 187 – 194, 2004

37. R.J.Walsh, S.Matsuzaki, T.Reinot, J.M.Hayes, K.R.Kalli, L.C.Hartmann, G.J. Small, Single-cell nonphotochemical hole burning of ovarian surface epithelial carcinoma and normal cells, PNAS , vol. 100, no. 4, 1685–1689, 2003

38. D. Grozdanov, N. Herascu, T. Reinot, R. Jankowiak, V. Zazubovich, Low-Temperature Protein Dynamics of the B800 Molecules in the LH2 Light-Harvesting Complex: Spectral Hole Burning Study and Comparison with Single Photosynthetic Complex Spectroscopy, J. Phys. Chem. 114, 3426-3438, 2010

39. C. Hofmann, T. J. Aartsma, H. Michel, J. Köhler, Direct observation of tiers in the energy landscape of a chromoprotein: A single-molecule study, PNAS, vol. 100, no. 26, 15534–15538, 2003

40. F. T. H. den Hartog, C. van Papendrecht, U. Storkel, S. Volker, Protein Dynamics in Photosystem II Complexes of Green Plants Studied by Time-Resolved Hole-Burning, J. Phys. Chem. B, 103, 1375-1380, 1999

41. V. V. Ponkratov, J. Friedrich, J. M. Vanderkooi, A. L. Burin, Y. A. Berlin, Physics of Proteins at Low Temperature, arXiv.org: cond-mat:arXiv:cond-mat/0407378v1[cond-mat.dist-nn] 15 Jul 2004

42. K. Henzler-Wildman, D. Kern, Dynamic personality of proteins, Nature, Vol 450, 3 , 964 – 972, 2007

43. H. Frauenfelder, S. G. Sligar, P. G. Wolynes, The energy landscapes and motions of proteins, Science, *254*, 1598, 1991

44. P. W. Fenimore, H. Frauenfelder, B. H. McMahon, R. D.Young, Proteins are paradigms of stochastic complexity, Physica A, 351, 1, 2005

45. J. Baier, M. F Richter; R. J. Cogdell, S. Oellerich,; J. Kohler, Determination of the Spectral Diffusion Kernel of a Protein by Single-Molecule Spectroscopy, Phys. Rev. Lett. 100, 018108, 2008

46. C. Hofmann, T. J. Aartsma, H. Michel, J. Kohler, Spectral dynamics in the B800 band of LH2 from *Rhodospirillum molischianum*: a single-molecule study, New J. Phys. 6, 8, 2004

47. A. M. van Oijen, M. Ketelaars, J. Kohler, T. J. Aartsma, J. Schmidt, Spectroscopy of individual light-harvesting 2 complexes of *Rhodopseudomonas acidophila*: diagonal disorder, intercomplex heterogeneity, spectral diffusion, and energy transfer in the B800 band, Biophys. J. 78, 1570, 2000

48. M. Ketelaars, A. M. van Oijen, M. Matsushita, J. Kohler, J. Schmidt, T. J. Aartsma, Spectroscopy on the B850 Band of Individual Light-Harvesting 2 Complexes of *Rhodopseudomonas acidophila* I. Experiments and Monte Carlo Simulations, Biophys. J. 80, 1591, 2001

49. M. Matsushita, M. Ketelaars, A. M.van Oijen, J. Kohler, T. J. Aartsma, J. Schmidt, Spectroscopy on the B850 Band of Individual Light-Harvesting 2 Complexes of *Rhodopseudomonas acidophila* II. Exciton States of an Elliptically Deformed Ring Aggregate, Biophys. J. *80*, 1604, 2001

50. C.Hofmann,; H. Michel, M.van Heel, J.Kohler, Multivariate Analysis of Single-Molecule Spectra: Surpassing Spectral Diffusion Phys. Rev. Lett. 94, 195501, 2005

51. V. V. Ponkratov, J. Friedrich, J. M. Vandrekooi, Hole Burning experiments with proteins: Relaxations, fluctuations and glass-like features, J. Non-crystaline Solids 352, 4379-4386, 2006

52. D. Rutkauskas, V. I. Novoderezhkin, R. J. Cogdell, R. van Grondelle, Fluorescence spectroscopy of conformational changes of single LH2 complexes, Biophys. J, 88, 422, 2005

53. D. Rutkauskas, V. Novoderezkhin, R.J. Cogdell, R.van Grondelle, Fluorescence spectral fluctuations of single LH2 complexes from *Rhodopseudomonas acidophila* strain 10050, Biochemistry, Apr 20;43(15):4431-8, 2004

54. V. Zazubovich, R. Jankowiak, G. J. Small, On B800-B800 energy transfer in the LH2 complex of purple bacteria, Journal of Luminescence 98, 123–129, 2002

55. J. T. M. Kennis, A. M. Streltsov, H. Permentier, T. J. Aartsma, J. Amesz, Exciton Coherence and Energy Transfer in the LH2 Antenna Complex of *Rhodopseudomonas acidophila* at Low Temperature, J. Phys. Chem. B, 101, 8369-8374, 1997

56. N. C. Dang, T. Reinot, M. Reppert, R. Jankowiak, Temperature Dependence of Hole Growth Kinetics in Aluminum – Phthalocyanine –Tetrasulfonate in Hyperquenched Glassy Water, , J. Phys. Chem.B, 111, 1582, 2007

57. V. Zazubovich, I. Tibe, G. J Small, , Bacteriochlorophyll *a* Franck–Condon Factors for the $S_0 \rightarrow S_1(Q_y)$ Transition, J. Phys. Chem. B, 105, 12410, 2001

58. B. Loll, J. Kern, A. Zouni, W. Saenger, J. Biesiadka, K.-D. Irrgang, The antenna system of photosystem II from *Thermosynechococcus elongatus* at 3.2 A resolution, Photosynth. Res., 86, 175, 2005

59. J.M. Hayes, G.J. Small, Photochemical hole burning and strong electron-phonon coupling: primary donor states of reaction centers of photosynthetic bacteria, J. Phys. Chem., 90 (21), pp 4928–4931, 1986

60. K. J. Riley, R.Jankowiak, M. Ratsep, G. J. Small, V. Zazubovich, Evidence for Highly Dispersive Primary Charge Separation Kinetics and Gross Heterogeneity in the Isolated PS II Reaction Center of Green Plants, J. Phys. Chem. B, *108*, 10346, 2004

61. T. Reinot, G. J. Small, Non-Lorentzian zero-phonon holes and new insights on nonphotochemical hole burning: Al-phthalocyanine in hyperquenched glassy water, J. Chem. Phys., 114, 9105, 2001

62. Y. Berlin, A. Burin, J. Friedrich, J. Kohler, Low temperature spectroscopy of proteins. Part II: Experiments with single protein complexes, Phys. Life Rev. 4, 64, 2007

63. Y. Berlin, A. Burin, J. Friedrich, J. Kohler, Spectroscopy of proteins at low temperature. Part I: Experiments with molecular ensembles, Phys. Life Rev. 3, 262, 2006

64. J. Baier, M. Gabrielsen, S. Oellerich, H. Michel, M. van Heel, R. J. Cogdell, , J. Köhler, Spectral Diffusion and Electron-Phonon Coupling of the B800 BChl *a* Molecules in LH2 Complexes from Three Different Species of Purple Bacteria, Biophys. J, 97, 2604, 2009

65. S. Jang, M. D. Newton, R. J. Silbey, Multichromophoric Förster Resonance Energy Transfer, Phys. Rev. Lett. 92, 218301, 2004

66. J. Baier, M. Gabrielsen, S. Oellerich, H. Michel, M. van Heel, R.J. Cogdell, J.Köhler, Spectral diffusion and electron-phonon coupling of the B800 BChl a molecules in LH2 complexes from three different species of purple bacteria, Biophys J. Nov 4;97(9):2604-12, 2009

67. N. Herascu, A. Amunts, J. Pieper, K-D Irrgang, R. Picorel, M. Seibert, N. Nelson and V. Zazubovich, Low-temperature Protein Dynamics of Several Small Light-harvesting Complexes Probed via Spectral Hole Growth Kinetics Measurements, in preparation

68. A. Sigi, M. Orrit,T. Reinot, R. Jankowiak, J. Friedrich, Terrylene in hexadecane revisited: A hole burning study, J. Chem.Phys. 127, 084510, 2007

69. A. Freiberg, M. Ratsep, K. Timpmann, G. Trinkunas, N. W. Woodbury, Self-Trapped Excitons in LH2 Antenna Complexes between 5 K and Ambient Temperature, J. Phys. Chem. B 107, 11510, 2003

70. J. Baier, M. F, Richter, R. J. Cogdell, S. Oellerich, J. Köhler, Do proteins at low temperature behave as glasses? A single-molecule study, J. Phys. Chem. B, 111, 1135, 2007

71. J. Janusonis, L. Valkunas, D. Rutkauskas, R. van Grondelle, Spectral Dynamics of Individual Bacterial Light-Harvesting Complexes: Alternative Disorder Model, Biophys. J. 94, 1348, 2008

72. V. I. Novoderezhkin, D. Rutkauskas, R. van Grondelle, Energy transfer in photosynthesis: experimental insights and quantitative models, Biophys. J, 90, 2890, 2006

73. V. Zazubovich, R. Jankowiak, On the energy transfer between quasi-degenerate states with uncorrelated site distribution functions: An application to the CP43 complex of Photosystem II, J. of Luminescence 127, 245–250, 2007

74. H. Du, R. A. Fuh, J. Li, A. Corkan, J. S. Lindsey, PhotochemCAD: a computer-aided design and research tool in photochemistry, Photochem. Photobiol, 68, 141, 1998

75. R. Jankowiak, V. Zazubovich, M. Ratsep, S. Matsuzaki, M. Alfonso, R. Picorel, M. Seibert, G. J. Small, The CP43 Core Antenna Complex of Photosystem II Possesses Two Quasi-Degenerate and Weakly Coupled Q*y*-Trap States, J. Phys. Chem. B, 104, 11805-11815, 2000

76. R. Jankowiak, V. Zazubovich, M. Rätsep, S. Matsuzaki, M. Alfonso, R. Picorel, M. Seibert, G. J. M., Small, The CP43 Core Antenna Complex of Photosystem II Possesses Two Quasi-Degenerate and Weakly Coupled Q_y-Trap States, J. Phys. Chem. B, 104, 11805, 2000

77. M. Di Donato, R. van Grondelle, I. H. M van Stokkum, M. L Groot, Excitation energy transfer in the Photosystem II core antenna complex CP43 studied by femtosecond visible/visible and visible/mid-infrared pump probe spectroscopy, J. Phys. Chem. B, 111, 7345, 2007

78. J-F He, S-C Wang, S. Zhang, F-T He, J-X Shan, T-Y Kuang, Kinetic fluorescence spectral analysis od core antenna CP43 and CP47 of Photosystem II with ultrafast time-resolved technology, *Acta Botanica Sinica / Journal of Integrative Plant Biology*, 43, 704, 2001

79. M. Reppert, V. Zazubovich, N. C. Dang, M. Seibert, R. Jankowiak, The CP43 Proximal Antenna Complex of Higher Plant Photosystem II Revisited: Modeling and Hole Burning Study. II, *J. Phys. Chem.* B, 112, 9934, 2008

80. J. Pieper, K-D Irrgang, M. Rätsep, J. Voigt, G. Renger, G. J. Small, Assignment of the lowest Q_Y-state and spectral dynamics of the CP29 chlorophyll *a/b* antenna complex of green plants: a hole-burning study, Photochem. Photobiol. 71, 574, 2000

81. E.I.Iseri, D. Gulen, Chlorophyll transition dipole moment orientations and pathways for flow of excitation energy among the chlorophylls of the major plant antenna, LHCII, Eur. Biophys. J. 30: 344-353, 2001

82. Gillie, J. K., Small, G. J., Golbeck, J. H., Nonphotochemical hole burning of the native antenna complex of photosystem I (PSI-200), J. Phys. Chem. 93, 1620, 1989

83. J. L. Hughes, B. J. Prince, S. Peterson Ärsköld,.E. Krausz, R. J. Pace, R. Picorel, M. Seibert, Photo-conversion of chlorophylls in higher-plant CP43 characterized by persistent spectral hole burningat 1.7K, J. Lumin. 108, 131, 2004

84. Tietz, C., Jelezko, F., Gerken, U., Schuler, S., Schubert, A., Rogl, H., Wrachtrup, J., Single molecule spectroscopy on the light-harvesting complex II of higher plants, Biophys. J, 81, 556, 2001

85. M. Rätsep, J. Pieper, K.-D Irrgang, A. Freiberg, Excitation wavelength-dependent electron-phonon and electro-vibrational coupling in the CP29 antenna complex of green plants, *J. Phys. Chem.* B, 112, 110, 2008

86. J. Huyer, H-J Eckert, K-D Irrgang, J. Miao, H-J Eichler, G. Renger, Fluorescence Decay Kinetics of Solubilized Pigment Protein Complexes from the Distal, Proximal, and Core Antenna of Photosystem II in the Range of 10–277 K and Absence or Presence of Sucrose, J. Phys. Chem. B, 108, 3326, 2004

87. J. M. Salverda, M. Vengris, B. P. Krueger, G. D. Scholesz, A. R. Czarnoleski, Vladimir Novoderezhkin, Herbert van Amerongen, and Rienk van Grondelle Energy Transfer in Light-Harvesting Complexes LHCII and CP29 of Spinach Studied with Three Pulse Echo Peak Shift and Transient Grating, Biophysical Journal Vol. 84, 450–465, January 2003

88. J. Pieper, M. Ratsep, K-D Irrgang, A. Freiberg, Chromophore-Chromophore and Chromophore-Protein Interactions in Monomeric Light-Harvesting Complex II of Green

Plants Studied by Spectral Hole Burning and Fluorescence Line Narrowing, J. Phys. Chem. B, 113, 10870–10880, 2009

89. J. Pieper, K.-D. Irrgang, M. Ratsep, R. Jankowiak, Th. Schrotter, J. Voigt, G. J. Small, and G. Renger, Effects of Aggregation on Trimeric Light-Harvesting Complex II of Green Plants: A Hole-Burning Study, J. Phys. Chem. A, 103, 2422-2428, 1999

90. M. Wentworth, A. V. Ruban, P. Horton, The Functional Significance of the Monomeric and Trimeric States of the Photosystem II Light Harvesting Complexes, Biochemistry, 43, 501-509, 2004

91. J. Standfuss, W. Kuhlbrandt, The three isomers of the light-harvesting complex II, Spectroscopic features, trimer formation and functional roles, J. Biol. Chem, vol. 279, no. 35, 36884-36891, 2004

92. G. Jackowski, K. Kacprazak, S. Jansson, Biochem. Biophys. Acta, 1504, Identification of Lhcb1/Lhcb2/Lhcb3 heterotrimers of the main light-harvesting chlorophyll *a/b*–protein complex of Photosystem II (LHC II), 340-345 2001

93. U.K.Larsson, B. Andersson, Different degrees of phosphorylation and lateral mobility of two polypeptides belonging to the light-harvesting complex of photosystem II, Biochem. Biophys. Acta, 809, 396-402, 1985

94. U.K. Larsson, C. Sundby, B. Andersson, Variations in the relative content of the peripheral and tightly bound LHCII subpopulations during thylakoid light adaptation and development. Biochim Biophys Acta, Biochem. Biophys. Acta, 894, 59-68, 1987

95. N. R. S. Reddy, H. van Amerongen, S. L. S. Kwa, R. van Grondelle, G. J. Small, Low-energy exciton level structure and dynamics in light harvesting complex II trimers from the Chl a/b antenna complex of photosystem II, J. Phys. Chem, 98, 4729-4735, 1994

96. J. Pieper, J. Voigt, G. Renger, G. J. Small, Analysis of phonon structure in line-narrowed optical spectra, Chem. Phys. Lett. 310, 296, 1999

97. F. Jelezko, C. Tietz., E. Thews, S. Schuler, A. Wechsler, J. Wrachtrup, Single molecule spectroscopy on photosynthetic pigment-protein complexes, Optics and Spectroscopy, 91, 486, 2001

98. J. Pieper, R. Schödel, K-D Irrgang, J. Voigt, G. Renger, Electron-phonon coupling in solubilized LHCII complexes of green plants investigated by line – narrowing and temperature-dependent fluorescence spectroscopy, J. Phys. Chem. B, 105, 7115, 2001

99. T. Reinot, N. C. Dang, G. J. Small, Non-photochemical Versus Photochemical Hole Burning in Hyperquenched Glassy Water and Cubic Ice J. Lumin. 98, 183, 2002

100. M. A. Palacios, F. L. de Weerd, J. A. Ihalainen, R. Van Grondelle, H. Van Amerongen, Superradiance and exciton (De)localization in light harvesting complex II from green Plants?, J. Phys. Chem. B 106, 5782 – 5787, 2002

101. V. I.Novoderezhkin, M. A. Palacios, H. van Amerongen, R.van Grondelle, Excitation dynamics in the LHCII complex of higher plants: Modeling based on the 2.72 Å crystal structure, J. Phys. Chem. B, 109, 10493, 2005

102. J. Linnanto, J. Martiskainen, V. Lehtovuori, J. Ihalainen, R. Kananavicius, R. Barbato, J.Korppi-Tommola, Photosynth. Res. 2006, 87, 267

103. G. Shlau-Cohen, T. R. Calhoun, N. S. Ginsberg, E. L. Read, M. Ballottari, R. Bassi, R. van Grondelle, G. R. Fleming, Pathways of Energy Flow in LHCII from Two-Dimensional Electronic Spectroscopy, J. Phys. Chem B, 113, 15352, 2009

104. J. Standfuss, M. Lamborghini, W. Kühlbrandt, A. C. T. van Scheltinga, Mechanisms of photoprotection and nonphotochemical quenching in pea light-harvesting complex at 2.5 Å resolution, EMBO J., *24*, 919, 2005

105. W. Kühlbrandt, D. N. Wang, Y. Fujiyoshi, Atomic model of plant light-harvesting complex by electron crystallography, Nature, 367, 614, 1994

106. I. Grotjohann, P. Fromme, Structure of cyanobacterial Photosystem I, Photosynthesis Research, 85: 51–72, 2005

107. P. Fromme, P. Mathis, Unraveling the Photosystem I reaction center: a history, or the sum of many efforts, Photosynthesis Research 80: 109–124, 2004